J Mater Sci (2016) 51:513–553
DOI 10.1007/s10853-015-9324-2

50TH ANNIVERSARY

Magnetic nanoparticles: material engineering and emerging applications in lithography and biomedicine

Yuping Bao[1] · Tianlong Wen[2] · Anna Cristina S. Samia[3] · Amit Khandhar[4] · Kannan M. Krishnan[5]

Received: 9 June 2015 / Accepted: 31 July 2015 / Published online: 1 September 2015
© Springer Science+Business Media New York 2015

Abstract We present an interdisciplinary overview of material engineering and emerging applications of iron oxide nanoparticles. We discuss material engineering of nanoparticles in the broadest sense, emphasizing size and shape control, large-area self-assembly, composite/hybrid structures, and surface engineering. This is followed by a discussion of several nontraditional, emerging applications of iron oxide nanoparticles, including nanoparticle lithography, magnetic particle imaging, magnetic guided drug delivery, and positive contrast agents for magnetic resonance imaging. We conclude with a succinct discussion of the pharmacokinetics pathways of iron oxide nanoparticles in the human body—an important and required practical consideration for any in vivo biomedical application, followed by a brief outlook of the field.

✉ Kannan M. Krishnan
kannanmk@u.washington.edu

Yuping Bao
ybao@eng.ua.edu

Tianlong Wen
halong@uestc.edu.cn

Anna Cristina S. Samia
anna.samia@case.edu

Amit Khandhar
amit@lodespin.com

[1] Chemical and Biological Engineering, The University of Alabama, Tuscaloosa, AL 35487, USA

[2] State Key Laboratory of Electronic Thin Films and Integrated Devices, University of Electronic Science and Technology of China, Chengdu 610054, China

[3] Chemistry, Case Western Reserve University, Cleveland, OH 44106, USA

[4] Lodespin Labs, PO Box 95632, Seattle, WA 98145, USA

[5] Materials Science and Engineering, University of Washington, Seattle 98195, USA

Introduction

Magnetic nanoparticles have been explored for numerous applications, such as catalysts for water splitting [1–3], nanomedicine [4–9], and as matrices for matrix-assisted laser desorption/ionization (MALD) analysis [10]. Fundamental magnetic properties of nanoparticles critically define their potential applications, such as hard magnets for data storage and soft magnetic materials for magnetic switches. The properties of magnetic ferrite nanoparticles can be tuned by size [11], surface [12], shape [13–16], assembly [17, 18], coupling [19], and doping [20–22]. For instance, iron oxide nanoparticles over ~28 nm[1] are ferrimagnetic and widely used for magnetic separation and as ferrofluids for liquid seals around the spinning drive shafts in hard disks and in loudspeakers to remove heat from the voice coil [23]. Iron oxide nanoparticles below 28 nm are superparamagnetic at room temperature (measurement time ~100 s), and are heavily explored for biomedical applications, such as drug delivery [24, 25], cancer therapy via magnetic hyperthermia [26], as contrast agents for magnetic resonance imaging (MRI) [27], and the emerging technique of magnetic particle imaging (MPI) [5]. Iron oxide nanoparticles smaller than 4 nm become primarily paramagnetic and can be used as positive (T_1) MRI contrast agents [28]. Recently, it has been shown that nonspherical iron oxide nanoparticles could improve their usefulness for biomedical applications. For examples, ultrathin iron oxide

[1] Unless specified, nanoparticle size in this review always refers to diameter

nanowires can serve as effective T_1 MRI contrast agents [29]. Iron oxide nanoworm-like particles formed by aggregation of spherical nanoparticles showed increased blood circulation time and more effective targeting [30]. Iron oxide nanocubes demonstrate extremely high r_2 relaxivity as negative MRI contrast agents [31], and a high value of the specific absorption rate necessary for hyperthermia cancer treatment [32]. Iron oxide nanoparticle tracers are central to realizing the true potential of MPI in translational clinical applications [33]. Furthermore, the magnetic properties and performance of nanoparticles can be enhanced through interactions with their environments (e.g., self-assembly) and integration with other types of materials (composites or hybrid structures).

In practice, the behavior of nanoparticles is not only affected by their intrinsic properties but also by the surrounding environments [34, 35]. Besides that, nanoparticles can serve as fundamental building blocks, often through the process of self-assembly, to build artificial materials, which could be potentially used in a variety of applications [36–40]. As a result, it is possible to manipulate the spatial arrangement of nanoparticles so that their response to external stimuli can be tuned for different applications. Self-assembly is a technique that is both economical and powerful, and can be used to control the spatial arrangement of nanoparticles [41–46]. Nanoparticle self-assembly can be affected by factors such as interparticle interactions, pre-patterned features, evaporation rate and directions of carrier fluids, and surfactants [47–51]. By controlling these factors, magnetic nanoparticles can be self-assembled into different patterns and morphologies [42, 52–54]. Instead of discussing the broad topic of self-assembly, we mainly concentrate on magnetic nanoparticle monolayers [55] and hierarchical nanoparticle assembly arrays [56]. To obtain long-range order in nanoparticle assembly, the nanoparticles should be made monodisperse, which can be realized by controlling the nucleation and growth of nanoparticles [57–59]. Recent interest in nanomaterial fabrication has gone beyond the production of a single material. Integration of multiple nanocomponents provides the capability of performing multiple tasks on a single platform [60–62]. For example, the integration of magnetic nanoparticles with fluorescent probes offer dual imaging probes [63] [64], and magnetic nanoparticle-quantum dot hybrid systems allow simultaneous multimodal imaging (microscopy, fluorescence, MRI) [65, 66] and therapy (hyperthermia) [67, 68].

Among various possibilities, iron oxide nanoparticles offer significant promise due to their chemical stability, easy preparation, and low cost. In particular, their intrinsic biocompatibility makes iron oxide nanoparticles the primarily candidate for nanomedicine. For any biomedical and biological applications, water solubility and surface functionality of nanoparticles are key parameters to their interactions with biological systems. Surface coatings, in particular, directly affect nanoparticle cellular uptake [69], biodistribution [70], blood circulation [71], and metabolism [72]. Therefore, surface engineering is essential to achieve various functionalities (e.g., biocompatibility and targeting). The enhanced physical and chemical properties of magnetic nanoparticles have enabled them to be used a wide range of new applications.

In this revimutipleew article, we will discuss material engineering aspects of iron oxide nanoparticles (e.g., size, shape, self-assembly, and hybrids) for improved chemical and physical properties, and surface engineering strategies for effective conjugation of functional molecules onto iron oxide nanoparticle surfaces. Furthermore, emerging applications of magnetic nanoparticles will be discussed, including magnet-guided drug delivery, positive MRI contrast agents, tracers for MPI, and nanoparticle lithography. Finally, the pharmacokinetic pathways of iron oxide nanoparticles, critical for in vivo applications, are also presented.

Material engineering

Fundamentals of magnetic nanoparticles

Magnetic materials show a wide range of behaviors; at one end are the noninteracting spins in paramagnets and characterized by a temperature-dependent susceptibility ($\chi = M/H \propto 1/T$) given by Curie's law. At the other end are the ferromagnets, with exchange interactions between spins, exhibiting hysteretic, $M(H)$, behavior, and a finite coercivity, H_C ($M = 0$), that is strongly dependent on the microstructure. Further, to minimize the overall magnetic energy, the material often forms domains, separated by domain walls with widths determined by the ratio of the exchange to anisotropy energies. However, if we reduce the size of any ferromagnet, we will ultimately reach a size where thermal energy ($k_BT \sim 25$ meV, at 300 K) will compete with the prevailing anisotropy and randomize the magnetization direction such that for a typical measurement time ($\sim$100 s) the magnetization, $M = 0$, when no field is applied ($H = 0$). In other words, such materials show no coercivity ($H_C = 0$), behaves similar to paramagnets but with very large moments, and are called superparamagnets. In practice, the randomization of the magnetization direction takes place by excitations over an energy barrier, $\varepsilon_B = KV$, given by the product of the anisotropy constant, K, and the volume, V. As a first approximation, neglecting the applied field, the Arrhenius law can describe thermal excitations of the magnetic moment over an energy barrier, ε_B, with relaxation time,

$\tau = \tau_0 \exp(KV\, k_B^{-1} T^{-1})$. Thus, superparamagnetic particles are defined by a characteristic diameter, D_{sp}, or a characteristic temperature called the blocking temperature, T_B, such that, for a given measurement time, a sharp division from superparamagnetic to ferromagnetic behavior can be observed either as a function of size (Fig. 1a) or temperature. Similar to a paramagnet, the magnetization response, $M(H)$, of a superparamagnet is also given by the Langevin function. Note that because the relaxation time, τ, depends exponentially on the energy barrier, KV, to reproducibly control the magnetic behavior of superparamagnetic nanoparticles, especially under alternating fields, such as in MPI [73], tailored size and monodisperse size distributions in nanoparticle synthesis are required. Finally, for slightly larger particles, it is also important to consider the critical size that determines whether it is favorable to be uniformly magnetized (single domain), or to break into multiple domains to minimize their overall energy. Using simple models for domain stability in fine particles [74] and bulk properties available in the literature, one can determine the characteristic size, D_{sd}, up to which single domains are stable [75]. For particles with cubic anisotropy, the critical radius, $R_c = 9/\mu_0 M_s^2$, with $D_{sd} = 2\,R_c$, at which the nanoparticle breaks into multidomains is a balance between the additional energy cost of introducing the domain wall and the reduction/gain in magnetostatic energy. This series of magnetic "phases" as a function of size is shown (Fig. 1b) for different ferromagnets and includes a "single domain" size (D_{sd}) below which the material will not support a multidomain particle [76] and a size (D_{sp}) defined by the superparamagnetic effect. Note that the characteristic size, D_{sp}, is determined by the measurement time (typically, 100 s is assumed); however, if the nanoparticles are subject to AC measurements, where the sampling time is inverse of the frequency, the observed D_{sp} would be smaller than that shown in Fig. 1b and inversely related to the sampling frequency.

Material engineering

Numerous metallic [77–81] and alloy [82–85] magnetic nanoparticles have been synthesized, but here, we focus on the material engineering of iron oxide nanoparticles because of their ubiquity in nature, biocompatibility, and unique suitability for in vivo biomedical applications. Several synthetic methods are available for iron oxide nanoparticles, such as coprecipitation [86], and hot injection [87]; however, currently iron oxide nanoparticles of high-quality monodisperse type, controlled size, phase-purity, and high crystallinity without defects are normally produced in organic solvents at high temperatures [87–91]. In this section, the discussion of size and shape control will be primarily focused on the thermal decomposition of iron oleate in an organic solvent at high temperature: the so-called heat-up method [90, 92]. This method allows for the production of iron oxide nanoparticles with great reproducibility and control of physical parameters. The overall synthetic process includes two major steps: (1) preparation of the precursor, iron oleate ($Fe(oleate)_3$) complex, and (2) synthesis of nanoparticles at high temperatures. Originally, the synthesis of spherical iron oxide nanoparticles (5–25 nm) by the thermal decomposition of iron oleate in 1-octadecene at 300 °C was reported with oleic acid (OA) as the only ligand [90]. Several modifications have been made to this process to achieve easy surface functionalization of spherical nanoparticles [64, 92, 93], or

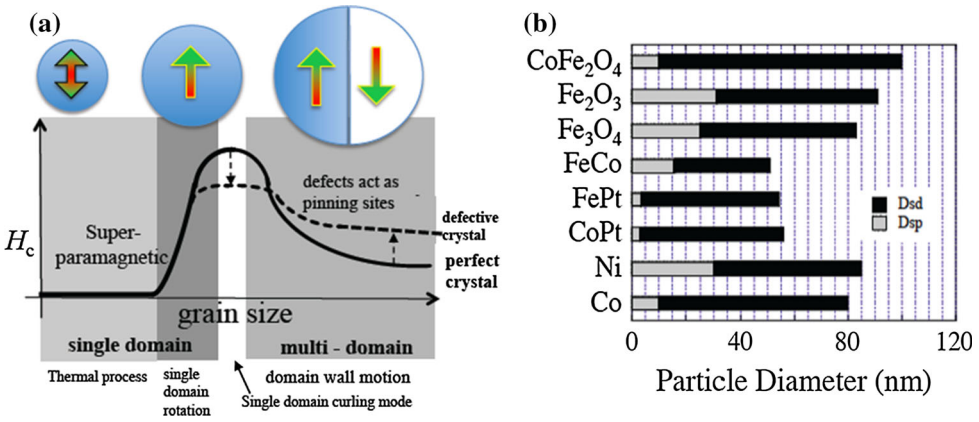

Fig. 1 **a** Magnetic behavior of nanoparticles as a function of diameter, D, defined as a function of their coercivity, H_c. For superparamagnetic particles, $D < D_{sp}$, $H_c = 0$ as they are thermally excited within the measurements time (typically 100 s). For $D > D_{sd}$, they split into multiple domains. For $D_{sp} < D < D_{sd}$, they are ferromagnetic and single domain. **b** These characteristic sizes depend on their intrinsic properties (saturation magnetization, M_s, anisotropy constant, K, and exchange stiffness, A) and can easily be calculated; critical sizes for the observation of superparamagnetism, D_{sp}, and single-domain, D_{sd}, and behaviors for a variety of common ferromagnetic nanoparticles are shown [75]. Copyright © 2006 Springer

preparation of iron oxide nanoparticles with other shapes, such as ultrathin nanowhiskers [16], nanoplates and nanoflowers [15], nanocubes [22], and single crystalline nanoworms [14]. The modified "heat-up" methods for the production of various iron oxide nanoparticles will be elaborated in the following sections. One specific set of modifications is centered on temperature control and addition of ligands to alter the nucleation and growth process (Fig. 2).

Size and shape control of iron oxide nanoparticles

The size of spherical nanoparticles has been an important parameter to tune their magnetic properties for various applications. The size control of iron oxide nanoparticles has been primarily focused on two regimes for biomedical applications: paramagnetic ultrasmall nanospheres (<4 nm), and superparamagnetic nanoparticles (5–27 nm). The ultrasmall spheres were primarily developed as positive contrast agents for MRI [94], while the superparamagnetic nanoparticles have been explored for various biomedical imaging, diagnostic, and therapy applications.

Because of the burst nucleation and rapid nanoparticle growth at high temperatures, the original "heat-up" process generally produces spherical iron oxide nanoparticles over 5 nm [90]. To produce ultrasmall (<4 nm) iron oxide nanoparticles, several modifications were made to the original process. First, the reaction was performed in diphenyl ether at lower reaction temperature (258 °C), which is more viscous than the original solvent, 1-octadecene. Second, oleyl alcohol, a strong nanoparticle growth inhibitor, was introduced into the reaction. Both the lower temperature and the growth inhibitor slowed down the nanoparticle growth. Most importantly, the reaction was rapidly quenched shortly after nucleation stage, and nanoparticles were precipitated out of solution with cold hexane and ethanol to stop the nanoparticle growth. Figure 3 shows the transmission electron microscopy (TEM) image from a typical reaction similar to the previously reported procedure [94]. The high-resolution TEM image

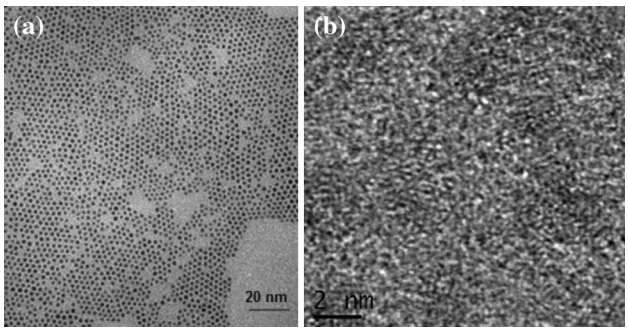

Fig. 3 TEM images of ultrasmall iron oxide nanospheres with an average diameter of 4 nm: **a** brightfield TEM image, and **b** high-resolution TEM image

indicates the crystalline structures of these small nanoparticles.

The original "heat-up" method can effectively produce superparamagnetic iron oxide nanoparticles over 5 nm. However, the use of only OA, a strong binding ligand, causes serious problems for subsequent surface modification. Water solubility is key to any biomedical application. To address this problem, an effective and facile method was developed by simply introducing a co-ligand, trioctylphosphine oxide—TOPO—during synthesis [92]. The use of TOPO is critically important for the subsequent ligand exchange and surface functionalization. TOPO has a weaker binding to iron oxide nanoparticle surfaces, compared to OA [95]. Besides the weaker binding, the bulky C_8 tails of the TOPO molecule prevent them from forming a dense packing layer on the nanoparticle surfaces [78]. These two properties, together, provide the preferred sites for hydrophilic ligands to attach or bind, initiating the ligand exchange process. Most importantly, the introduction of TOPO during synthesis does not affect the overall size of the iron oxide nanoparticles, and it also leads toward the production of less-faceted nanoparticles.

Figure 4 shows the TEM images of ~12-nm iron oxide nanoparticles with OA only (a) and OA/TOPO (b) capping ligands under similar reaction conditions. The

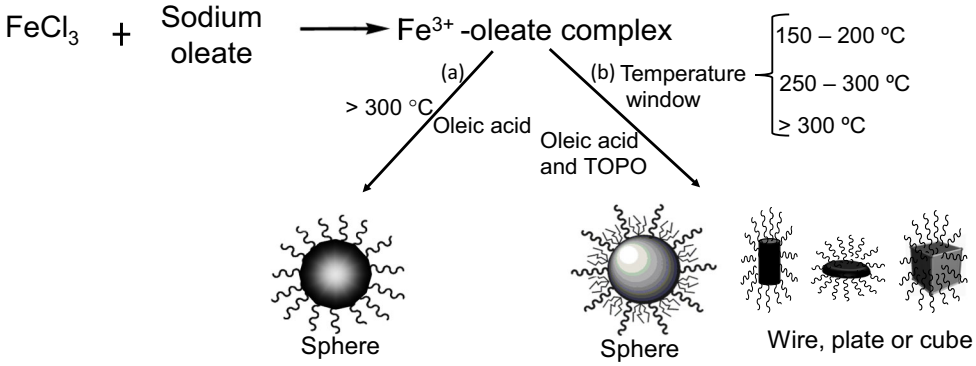

Fig. 2 Schematic drawing of the heat-up method: **a** original process, and **b** modified process

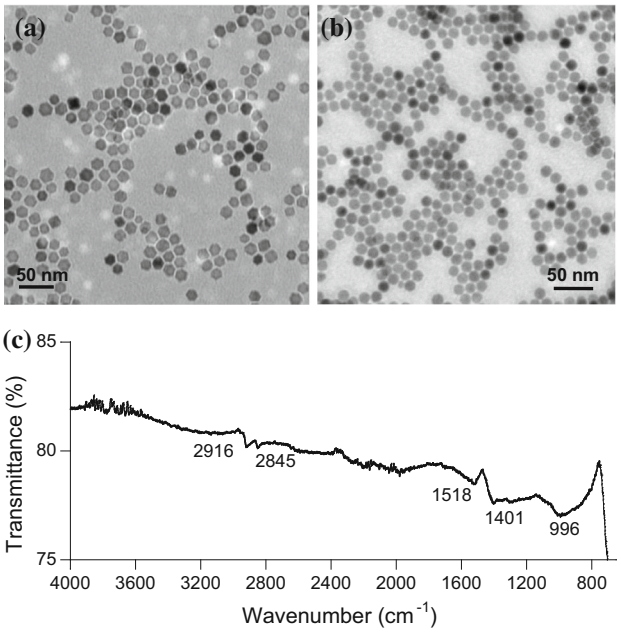

Fig. 4 TEM images of 12-nm monodispersed iron oxide nanoparticles synthesized using a modified heat-up method: **a** oleic acid only capping ligand, **b** oleic acid and TOPO ligands, and **c** FTIR spectra of iron oxide nanoparticles with oleic acid and TOPO capping ligands. Copyright © American Chemical Society 2011 [92]

nanoparticles from OA-only ligand were faceted, while the nanoparticles with TOPO addition are not faceted. The more spherical nanoparticles were likely because the weaker adsorption of TOPO on nanoparticle surfaces allowed for effective rearrangement of surface atoms. Fourier transform-infrared spectroscopy (FTIR) spectrum (Fig. 4c) of nanoparticles with TOPO/OA coatings exhibits the characteristic broad band of –P=O groups around 996 cm^{-1} [96], indicating the presence of TOPO capping molecules on the nanoparticle surfaces. The broad bands at 1518 and 1401 cm^{-1} were from the carboxylic groups of the OA molecules on the nanoparticle surfaces.

Larger magnetic nanoparticles were prepared by the thermal decomposition of iron (III) oleate with excess OA in 1-octadecene at 318 °C [96]. Such thermal decomposition approaches can produce monodispersed nanoparticles over a range of sizes, but the reactions are kinetically driven and sensitive to fluctuations that yield batch-to-batch variation in size and quality. In addition, if not carefully controlled, the reaction chemistry can produce variations in iron oxide phases and phase purities. Thus, nanoparticles were oxidized in situ with subsequent annealing at 318 °C for up to 30 h to ensure that phase-pure magnetite nanoparticles are synthesized. Furthermore, published protocols typically provide examples performed at small-scale and procedures that may not be scalable and frequently omit magnetic characterization that is critical for establishing suitability for applications such as MPI. With subsequent annealing, cores with median diameter in the range of 24–27 nm and geometric standard deviation of 1.06 were reproducibly synthesized in gram-scale quantities (Fig. 5a). Diffraction confirmed the particles were phase-pure magnetite (Fe_3O_4) with typical saturation magnetization of 350 kA/m measured by vibrating sample magnetometry (Fig. 5b). Note that there is significant effort involved in preparing anhydrous iron-oleate precursors suitable for reproducible particle synthesis. Alternatively, the use of iron oxy-hydroxide, also produces very high-quality nanoparticles, 25–30 nm in diameter, (Fig. 5c), with iron oleate being formed as an intermediate during the reaction [97]. Control of iron oxide phase and phase purity, by appropriate oxidation during synthesis, is critical to achieving phase purity and suitable magnetic properties.

Until recently, the synthesis of iron oxide nanoparticles with nonspherical shapes using the "heat-up" method has been limited to a few reports on nanocubes with addition of sodium oleate, or other chemicals [98–102]. The recent fundamental understanding of the chemical microenvironments of iron oleate precursor has opened the doors to the synthesis of other shaped iron oxide nanoparticles [16]. In brief, thermogravimetric analysis (TGA) and density functional theory (DFT) electronic structure calculations suggest that the three ligands of iron oleate complex have different binding affinities to the Fe(III) center with one oleate having much higher binding energy (39.2 eV) than the other two (7.0 and 10.5 eV), which yield several temperature-control windows for synthesis consideration (Fig. 6) [16]. Based on the optimized electronic structures of the iron oleate complex (Fig. 6a), two of the ligands are symmetric, and the third ligand is asymmetric. The TGA plot exhibited three distinct weight-loss windows: 150–250, 250–300, and 300–400 °C. The weight-loss

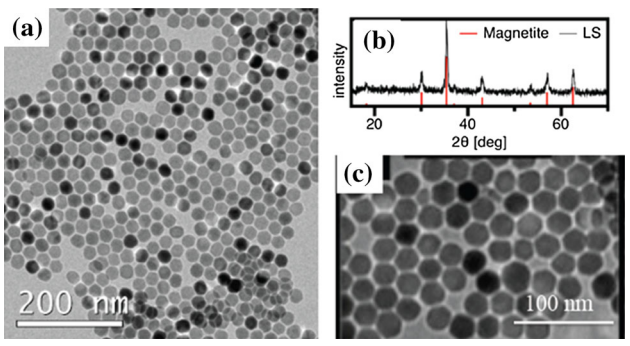

Fig. 5 **a** Transmission electron micrograph, and **b** X-ray θ–2θ scan of 25-nm diameter magnetite nanoparticles synthesized by the decomposition of iron-oleate precursor with excess surfactants. **c** 27-nm diameter magnetite nanoparticles made with iron oxy-hydroxide precursors. Both synthetic methods involved subsequent annealing to ensure magnetite phase purity

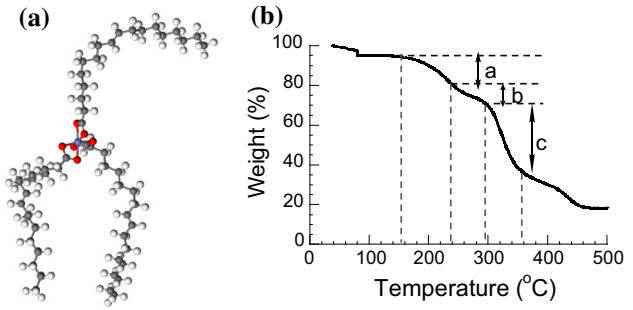

Fig. 6 Iron oleate: **a** optimized electronic structure from DFT calculation, and **b** TGA plot. Copyright © American Chemical Society 2011 [16]

window of 150–250 °C (Fig. 6b, region a) corresponds to the dissociation of the two symmetric ligands with lower binding energies. The weight losses are mainly due to the oleate ligand decomposition, releasing CO_2 gas. The weight loss ratio of about 2:1 agrees very well with two ligands of lower binding energies from the DFT calculations. The weight-loss window of 250–300 °C reflects the decomposition of the third ligand (Fig. 6b, region b), where the iron oxide nucleation initiates around 250 °C, which has also been suggested by Hyeon [103]. The continuous weight loss at above 300 °C was due to desorption of the decomposed ligands (Fig. 6b, region c). The TGA studies suggested that the original "heat-up" method (directly heating of the reaction mixture over 300 °C) overlooked the difference in the ligand microenvironments. Additional control within each temperature window offers great means for shape control, which serves as the foundation for the following experimental design to produce multiple-shaped iron oxide nanoparticles.

The different binding abilities of the three ligands within Fe(III) oleate allowed to selectively decompose the lower binding ligands at 150 °C. Interestingly, when a typical "heat-up" reaction was performed at 150 °C, iron oxide nanowhiskers with dimensions of approximately 2 × 20 nm were obtained (Fig. 7a). These nanostructures were single crystalline indicated by clear lattice fringes from the high-resolution TEM image of a single nanowhisker (Fig. 7a, inset). The calculated fringe spacing of 0.298 nm was close to the lattice spacing of the (220) plane of the cubic iron oxide spinel structure [104]. The selected area electron diffraction pattern suggested maghemite (γ-Fe_2O_3) crystal phase (Fig. 7b). The maghemite phase was further supported by Raman spectroscopy and X-ray photoelectron spectroscopy (XPS), as shown in Fig. 7c, d. The absence of the major feature peak of Fe_3O_4 at around 670 cm^{-1} suggests that these nanowhiskers are not magnetite phase; [105] in contrast, the main peaks of 725, 1295, and 1430 cm^{-1} can be readily assigned to the

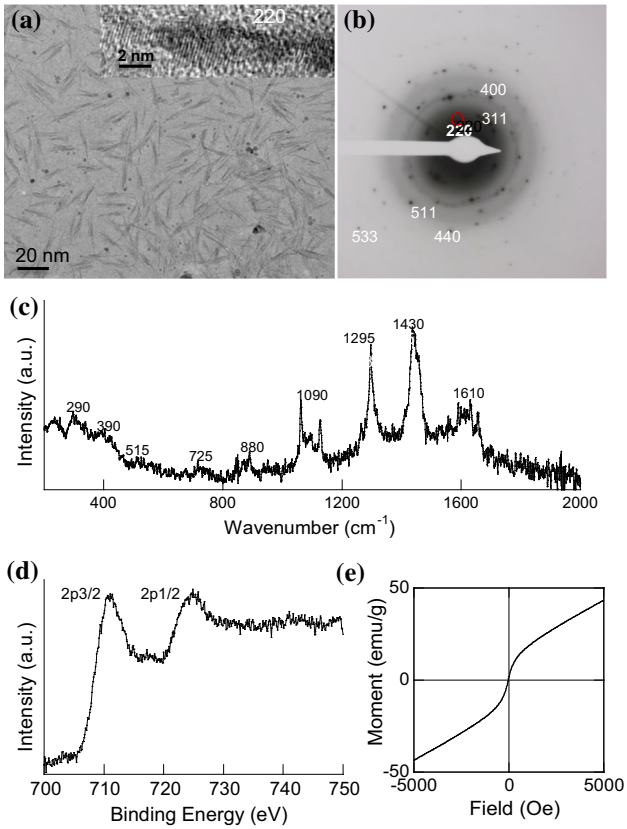

Fig. 7 Iron oxide nanowhiskers: **a** brightfield TEM image, and HRTEM-insert, **b** electron diffraction pattern, **c** a Raman spectrum, **d** Fe2p core-level spectrum, and **e** room temperature *M–H* curve. Copyright © American Chemical Society 2011 [16]

γ-Fe_2O_3 phase [106]. In addition, XPS offers an effective tool to differentiate magnetite (Fe_3O_4) from maghemite (γ-Fe_2O_3) [107]. The two major peaks at 710.7 and 725.0 eV of the XPS spectrum correspond to the $2p_{3/2}$ and $2p_{1/2}$ core levels of iron oxide (Fig. 7d). Small satellite signals around 718.0, 730.0, and 745.0 eV were an indicator of γ-Fe_2O_3 rather than Fe_3O_4, as suggested in [107].

The formation of γ–Fe_2O_3 can be readily understood because no Fe^{2+} ions were introduced during synthesis. The original "heat-up" method reported the formation of Fe_3O_4, mainly due to the Fe^{3+} reduction by H_2 or CO gases generated at high temperature from decomposing oleate ligands over 250 °C [103]. The low reaction temperature of the nanowhiskers minimized the generation of reducing gases, subsequently limiting the reduction of Fe^{3+} ions.

Because of the extremely high surface-to-volume ratio, the iron oxide nanowhiskers showed a strong paramagnetic signal from the magnetization versus applied field (*M–H*) curve (Fig. 7e). The observed magnetic property is a result of the high surface-to-volume ratio and surface iron–ligand complexation. The high percentage of surface atoms was linked to oleate ligands through coordination bonds,

behaving as iron complexes. The surface effects generate a magnetic "dead layer" on the nanoparticle surfaces, which is commonly observed in small magnetic nanoparticle systems [108–112]. Theoretical simulations also suggested that the dead layer is around 1 nm thick [113], and this effect could be significant in high surface-to-volume ratio nanostructures, as observed in our nanowhisker system. It was hypothesized that the nanowhisker formation was directed by the undecomposed third ligand, which self-assembled into a soft template and facilitated the nanowhisker formation.

The second weight-loss window (250–300 °C) is directly related to the nucleation and growth of iron oxide nanoparticles. A reaction temperature of 290 °C was chosen to study the ligand effects on the nucleation and nanoparticle growth process based on TGA plot of iron oleate [16, 103]. This temperature is high enough to decompose all three ligands of the precursor, but it is still below the burst nucleation temperature (>300 °C). At this temperature, different amounts of TOPO were used to alter the nucleation event. Interestingly, iron oxide nanoplates (~3 nm thick) were obtained with TOPO/OA ~1.65/1. Figure 8a shows the TEM image of iron oxide nanoplates with a side length of ~18 nm. This plate-like nanostructure was highly crystalline indicated by the lattice fringes of the HRTEM image (Fig. 8b), and the ordered dot pattern of the fast Fourier transformation (FFT) image (Fig. 8b, inset). The HRTEM image was obtained with a 30° α-tilt angle, which confirmed the thickness of the thin nanoplates was about 3 nm. However, under a similar reaction condition, nanoflowers (~20 nm) were produced by simply increasing the TOPO to OA ratio five times (Fig. 8c). The HRTEM image clearly indicated that the nanoflowers were composed of many small (~5 nm) iron oxide nanocrystals, which was also supported by the ring dot pattern of the FFT image (Fig. 8d).

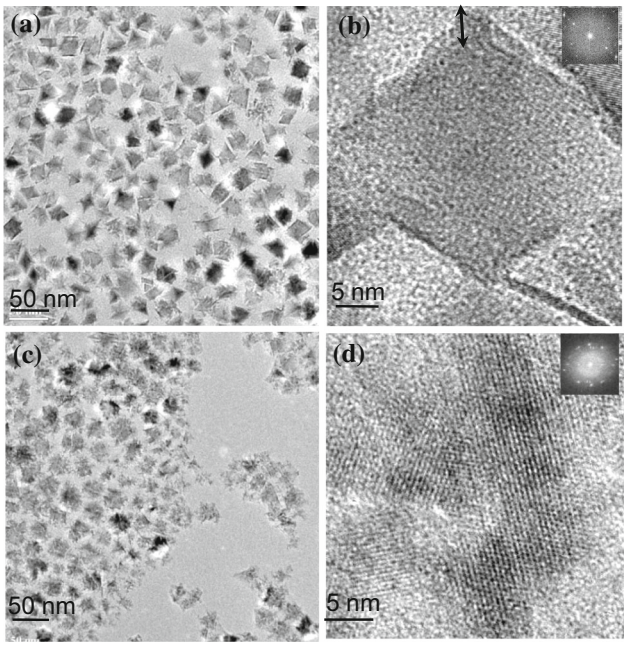

Fig. 8 TEM images of **a** nanoplates, **b** HRTEM of nanoplates (30° α-tilt), **c** nanoflowers, and **d** HRTEM of nanoflowers. Copyright © Royal Chemical Society 2012 [15]

The magnetization versus applied field (*M–H*) curves of both samples showed large saturation fields (>1.5 Tesla), similar to that of typical small (<5 nm) spherical nanoparticles (Fig. 9). The high-saturation magnetic fields indicated large surface areas of the nanostructures, leading to increased paramagnetic signal. Even though the nanoplates and nanoflowers have distinct morphologies, both samples have large surface areas. The high surface area was a result of the very thin morphology (~3 nm) of the nanoplates and the small crystalline grains (~5 nm) of the nanoflowers. The paramagnetic surface layer is from the surface capping molecules and the magnetically disordered spin of the surface atoms.

The formations of nanoplates and nanoflowers under similar reaction conditions suggested that capping ligands could be used to tailor the concentration of nuclei and subsequent nanoparticle growth. It was proposed that the nanoplates were formed following a diffusional-growth pathway, where $C_2H_5O^-$, an impurity from precursor preparation, served as the third ligand and facilitated the formation of nanoplates. In contrast, at high TOPO concentration, the high nucleus concentration induced the formation of the iron oxide nanoflowers through aggregation of very small iron oxide nanoparticles.

Studies of nanowhiskers and nanoplates/nanoflowers suggested the importance of reaction temperature as the nucleation process at 250 °C can be easily affected. Interestingly, by simply slowing down the nucleation

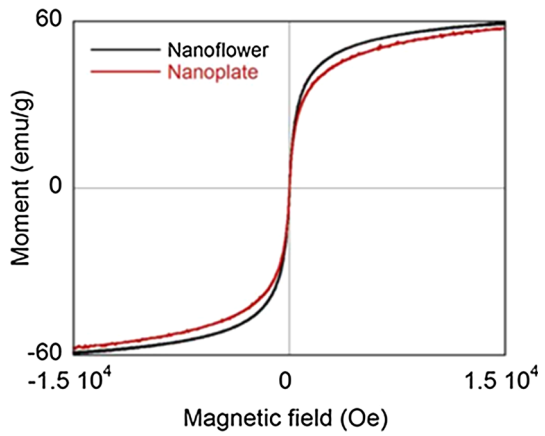

Fig. 9 The *M–H* curves of nanoplates and nanoflowers. Copyright © Royal Chemical Society 2012 [15]

process through step-heating processes (250 °C–20 min, 320 °C–30 min), well-defined iron oxide nanocubes can be obtained [22]. The design was to slow down the decomposition at 250 °C, allowing for the formation of cubic ferrite nuclei, and then the heating at 320 °C led to the nanocube growth on the preformed seeds. Figure 10 shows the TEM and high-resolution TEM images of the iron oxide nanocubes formed through the step-heating process. The Raman spectrum of iron oxide nanocubes in Fig. 10c shows the as-expected A_{1g} band at 671 cm^{-1}, corresponding to the vibrational stretching of the tetrahedral units, $T_{2g}(2)$ band around 490 cm^{-1} and $T_{2g}(3)$ band at 545 cm^{-1}, corresponding to the asymmetric stretching and bending of the Fe–O bonds. The shoulder peak near 715 cm^{-1} was assigned to the oxidation of Fe(II) irons at the octahedral sites. The core-level XPS spectra of M $2p_{3/2}$ and M $2p_{1/2}$ are shown in Fig. 10d. The Fe $2p_{3/2}$ and Fe $2p_{1/2}$ core-level peaks of Fe_3O_4 nanocubes were clearly observed at 711 and 724 eV, respectively. The absence of Fe $2p_{3/2}$ satellite peak at 718 eV was an indicator of magnetite (Fe_3O_4) formation, rather than maghemite (γ-Fe_2O_3). The shoulder peak at 709 eV also suggested the presence of Fe^{2+} ion.

The ligand not only plays an important role in nanoparticle nucleation around 250 °C, but it also affects the nanoparticle growth greatly over 300 °C. Introduction of a high concentration of TOPO around 300 °C induced the formation of iron oxide nanoworms via aggregation of nanospheres [14]. The rationale for the aggregation process is that TOPO-capping ligands on the nanoparticle surfaces

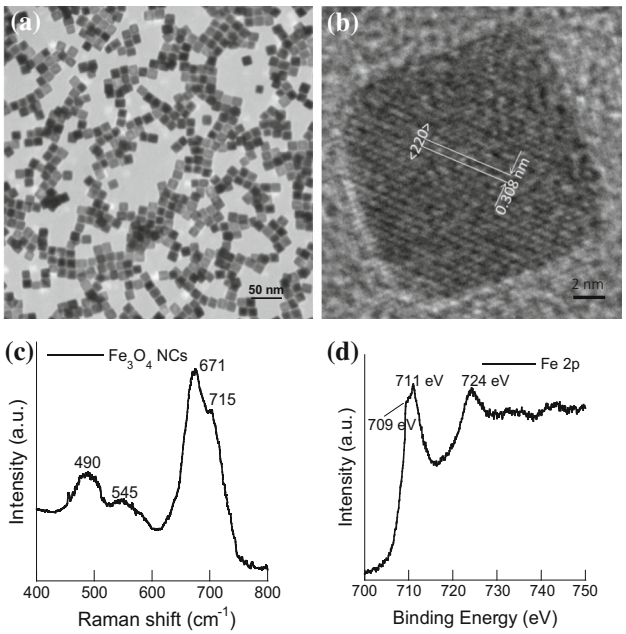

Fig. 10 Iron oxide nanocubes: **a** brightfield image, **b** high-resolution TEM image, **c** Raman spectrum, and **d** XPS spectrum

are dynamic (constantly attaching-detaching) at high temperatures because of their weaker binding to iron oxide surfaces [95] and the very bulky tails, which prevent them from forming a dense-packed layer on nanoparticle surfaces [78]. When the uncovered nanoparticle surfaces meet each other, the nanoparticles will start to interconnect, subsequently leading to the formation of nanoworms. In contrast to the 1:1 OA to TOPO ratio for nanosphere formation, over five times more TOPO molecules were needed to facilitate the aggregation process. In addition to the increased amount, TOPO was injected into the reaction around 300 °C for nanoworm formation, rather than being added before the heating process. This step was designed based on the TGA analysis to influence the nanoparticle growth, but not the nucleation process [16, 103].

Figure 11a shows the TEM images of iron oxide nanoworms produced from a typical reaction, where some spheres can still be seen. The high-resolution TEM (HRTEM) images (Fig. 11b) indicate the high crystallinity of the nanoworms, where the calculated lattice spacing of 0.209 nm corresponded to the (400) crystal plane of maghemite crystal structure. The X-ray diffraction pattern of the nanoworms exhibited typical peaks of maghemite (γ-Fe_2O_3) crystal structure, including the (220), (311), (400), (422), (511), (440), and (533) crystal planes. The open loop of the room-temperature magnetization versus applied magnetic field (*M–H*) curve suggests ferromagnetic properties of these nanoworms (Fig. 11d). In contrast, the nanospheres before aggregation are superrparamagnetic.

The aggregation process was confirmed by the time-dependent studies (Fig. 12) where samples were taken out of reaction at various reaction times (e.g., 1, 2.5, and 5 h). At 1 h, only a few of nanoworms were observed among mostly spherical nanoparticles (Fig. 12a). By 2.5 h, the typical reaction time, significant amount of nanoworms were formed with some spherical nanoparticles (Fig. 12b). After 5 h reactions, the nanoworms continuously grew in length to over 200 nm (Fig. 12c). With the increasing reaction time, only the lengths of the nanoworms were found to change, while the diameter remained the same as that of the starting nanospheres. These experimental observations supported the hypothesis that the nanoworms were formed from the aggregation of nanospheres.

In summary, the detailed analysis of the iron oleate thermal decomposition behavior, based on TGA measurements, allowed for the rational design of synthetic processes for the preparation of iron oxide nanoparticles with well-defined sizes, shapes, and surface properties.

Self-assembly of large-area nanoparticle arrays

Convective self-assembly is often performed to organize a large quantity of nanoparticles in 3D space [114–116].

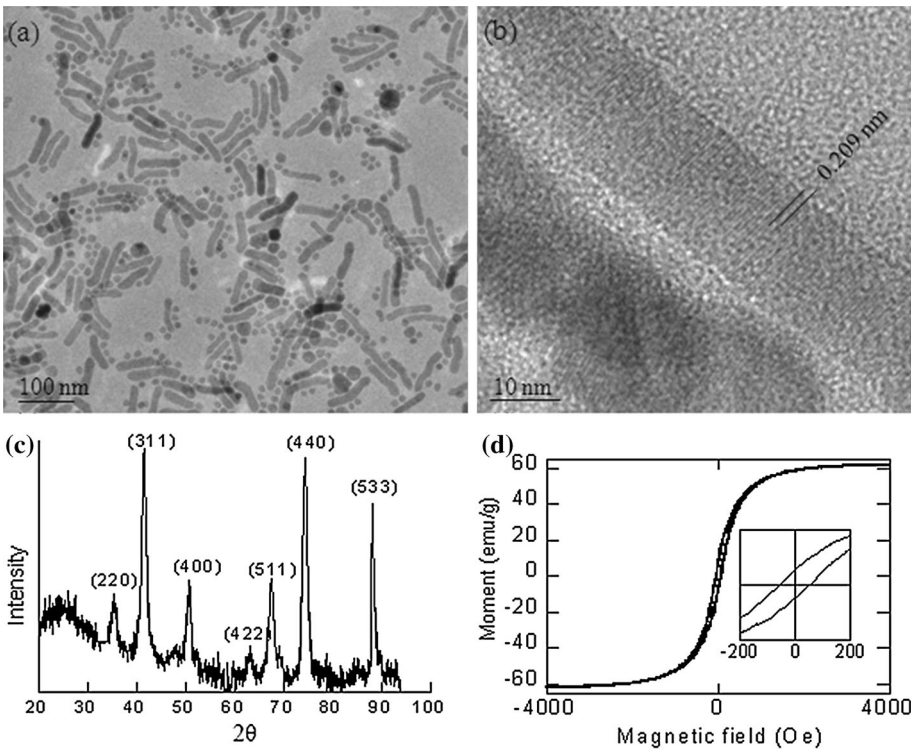

Fig. 11 The iron oxide nanoworms: **a** TEM image, **b** HRTEM, **c** XRD scan, and **d** *M–H* curve. Copyright © American Physical Society 2010 [14]

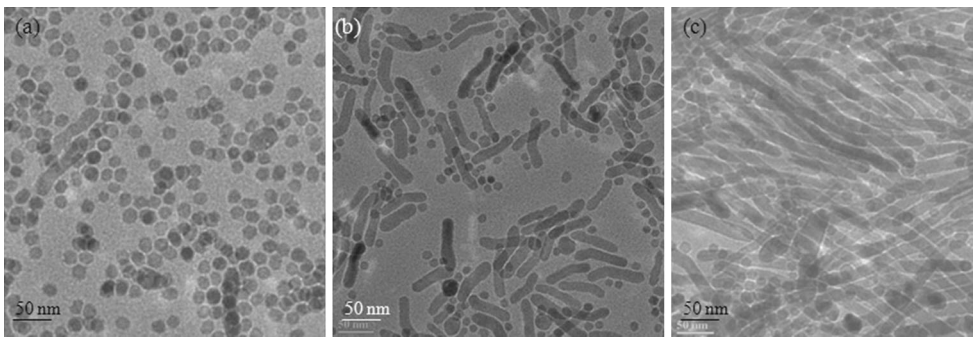

Fig. 12 TEM image of iron oxide NWs at different reaction times: **a** 1 h, **b** 2.5 h, and **c** 5 h. Copyright © American Physical Society 2010 [14]

First, nanoparticle cores are often stabilized by surfactants and dispersed in a carrier fluid [117]. Then, as the carrier solvent is evaporated, the convective flow will drive nanoparticles in solutions to move toward the drying front, where the capillary force in the meniscus squeezes nanoparticles together for nucleation and growth of nanoparticle assemblies [118]. Typically, the convective self-assembly of nanoparticles often occurs at the air/liquid or air/solid interfaces [49, 118]. The former gives nanoparticles more freedom to adjust their positions during self-assembly, and the latter allows us to control the movement of the contact line of the drying front by the pre-fabricated features on the surface [48, 50, 55, 119, 120]. Self-assembly of nanoparticles can be affected by a variety of factors, including drying front movement, nanoparticle movement in solution, evaporation rate, and directions of carrier fluids, etc. Here, we discuss controlling nanoparticle self-assembly by manipulating the evaporation of carrier solvent and the movement of drying front [41, 55, 56].

Interparticle interactions often play an important role in determining the spatial arrangements of nanoparticles [51]. After magnetic nanoparticles are brought closely together at the drying front by convective flow and capillary forces, magneto-static, van der Waals, steric, and depletion forces are the main forces that determine the final morphologies of the nanoparticle assemblies [42, 51, 52]. The dominant interaction between magnetic nanoparticles is determined by the sizes of nanoparticles [42]. Nanoparticles above a critical diameter, D_{sp}, are magnetically blocked at room temperature for typical measurement times of 100 s; then the magnetization of individual magnetic nanoparticles is frozen in direction (in the coordinate frame of the

nanoparticles) at room temperature [35, 75], and the north and south poles of nanoparticles are successively aligned during self-assembly to minimize magneto-static energy [42, 52]. In this case, nanoparticle chains are often obtained. Here, we focus on the self-assembly of superparamagnetic nanoparticles ($D < D_{sp}$), where van der Waals interactions dominate over magneto-static interactions [42, 51]. Strong van der Waals force is desired to assist nanoparticle assembly [121], which makes it easier for nanoparticle ensembles with larger sizes and higher densities of nanoparticle cores. The number of surrounding nanoparticles is often maximized to increase van de Waals interactions and reduce the free energy of the system. In addition, it has been demonstrated that the interactions are much stronger between faceted nanoparticles, which can be taken advantage for nanoparticle assemblies [122, 123]. For example, large-area nanoparticle monolayers were formed by using cubic cobalt ferrite nanoparticles and using the modified self-assembly method in Ref. [55], which is proposed for hard disk applications [124].

When a drop of nanoparticle solution is put on an open surface, carrier solvent evaporates along all possible directions. The concentration of nanoparticles at the drying front varies as the contact line retreats due to the variable evaporation rates and local concentrations at different positions and times. Due to this variation, nanoparticles are often clustered and distributed on the surface with gaps between them, such as the sample prepared by evaporating a nanoparticle solution on a TEM carbon film. Further, if the contact line of the evaporating solution is pinned, the evaporation will drive interior nanoparticles in solution to the drying front to deposit and form coffee stain rings [125, 126]. Monodisperse nanoparticles are often deposited layer-by-layer to build islands from a monolayer, to a bilayer, and then a multilayer. As the concentration of nanoparticles in solution increases, nanoparticle clusters will grow larger and thicker while the gaps between them gradually become smaller. By uncontrolled evaporation, no uniform and continuous nanoparticle assembly can be obtained over large areas, which is often necessary in many applications [38, 124]. To obtain high-quality nanoparticle assemblies, both evaporation direction and rate of carrier fluid should be carefully controlled [55]. Further, during growth, the nanoparticles should be driven steadily from interior solution to the drying front. By doing this, the nanoparticle concentration is approximately constant at the drying front when it moves so that the growth condition for nanoparticle assembly is almost the same at different times and locations to yield an uniform assembly [55]. Further, if the concentration of nanoparticles in solution is tuned properly to be below the critical value for formation of bilayers, monolayer of nanoparticles will form on the surface. However, the concentration should not be too low since the total number of nanoparticles determines the total area of the self-assembled monolayer(s) of nanoparticles [55].

In summary, the self-assembly of superparamagnetic nanoparticles can be 'intrinsically' affected by shape, size, and bulk density of the nanoparticle cores [122, 124, 127]. It is also 'extrinsically' affected by the evaporation rate and direction of carrier solvent, movement of contact line, and concentration of nanoparticle [55]. To make a high-quality nanoparticle assembly, these intrinsic and extrinsic factors should be carefully considered and designed for a convective self-assembly process. In addition, it is also found that extra surfactants in the solution can also significantly affect the self-assembly process [55]. Further, the extra surfactant could also improve the mechanical strength of the self-assembled monolayers [128–130]. Finally, the carrier solvent should be carefully chosen. The solvent should be a good dispersant with proper evaporation rate [55].

Figure 13a shows the schematic experimental settings used to control the evaporation of carrier solvent for fabricating continuous ultra-large-area self-assembled monolayer of nanoparticles [55]. Here, D.I. water is used as subphase to give nanoparticles freedom to relocate during self-assembly [55]. Iron oxide nanoparticles are coated with OA and dispersed in a mixture solvent of toluene and hexane with volume ratio of 1:2. Toluene and hexane are chosen because they can disperse surfactant-coated nanoparticles well, and they have appropriate evaporation rates [55]. The concentration of nanoparticles in the mixture solvent is tuned to be able to cover an area on the order of centimeters but low enough to prevent the formation of bilayers or multilayers. A drop of nanoparticle solution is spread on top of the liquid subphase in a trough, which is then partially covered by a glass slide, as shown in

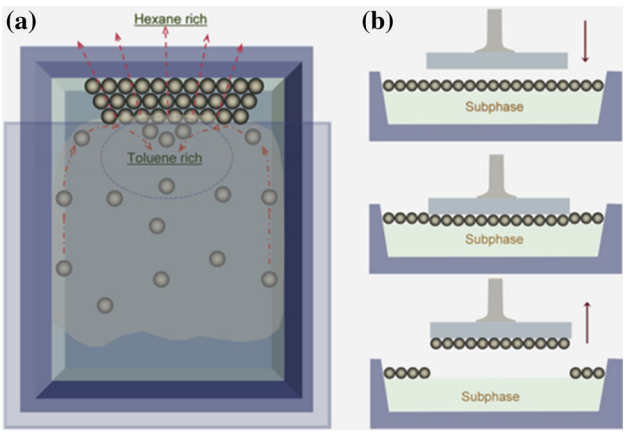

Fig. 13 **a** Top view of the apparatus for fabricating ultralarge-area self-assembled monolayers of nanoparticles on top of liquid subphase, and **b** collection of monolayer of nanoparticles floating on subphase. Copyright © American Chemical Society 2011 [55]

Fig. 13a. The partially covered trough can reduce the evaporation of the carrier solvent. It also only allows carrier solvent to evaporate along one direction to the opening. By doing this, the growth rate and the direction of nanoparticle monolayer are controlled [55]. Hexane evaporates quickly at the opening, while toluene flows back from the drying front to the interior solution. Droplets containing nanoparticles were thus circulated from the interior solution to the drying front along the sidewall of the trough. By doing this, the nanoparticles in the interior solution are continuously driven to the drying front, and the extra nanoparticles at the drying front were brought back by the circulating flow to the interior solutions [55]. As a result, the nanoparticle concentration at the drying front is approximately kept constant so that nanoparticle monolayer can be continuously extracted from the mixture solution.

Figure 14a shows the TEM image of large-area self-assembled monolayer of ~12 nm monodisperse Fe_3O_4 nanoparticles. After the carrier solvent has completely evaporated, a monolayer of iron oxide nanoparticles is floated on the surface of the subphase, which is then transferred to a substrate for further characterizations and applications, as shown in Fig. 14b. The area enclosed in (a) is magnified and shown in Fig. 14c, which shows a closely packed hexagonal monolayer of nanoparticles. Imperfections such as vacancies and edge dislocations are also observed in the nanoparticle monolayer, which minimize the free energy of the system [55]. The FFT of the monolayer in an area of ~7 μm × 7 μm in Fig. 14a is given in (d). The hexagonal pattern of the FFT indicates that all nanoparticles in this large area are aligned along a single crystal orientation. Lower magnification image of the monolayer is shown in the scanning electron micrograph (SEM) in Fig. 14b. The SEM overview shows that the monolayer is polycrystalline, but with long range order as shown in Fig. 14e. Figure 14b shows that the grains with different "crystallographic" orientations have different

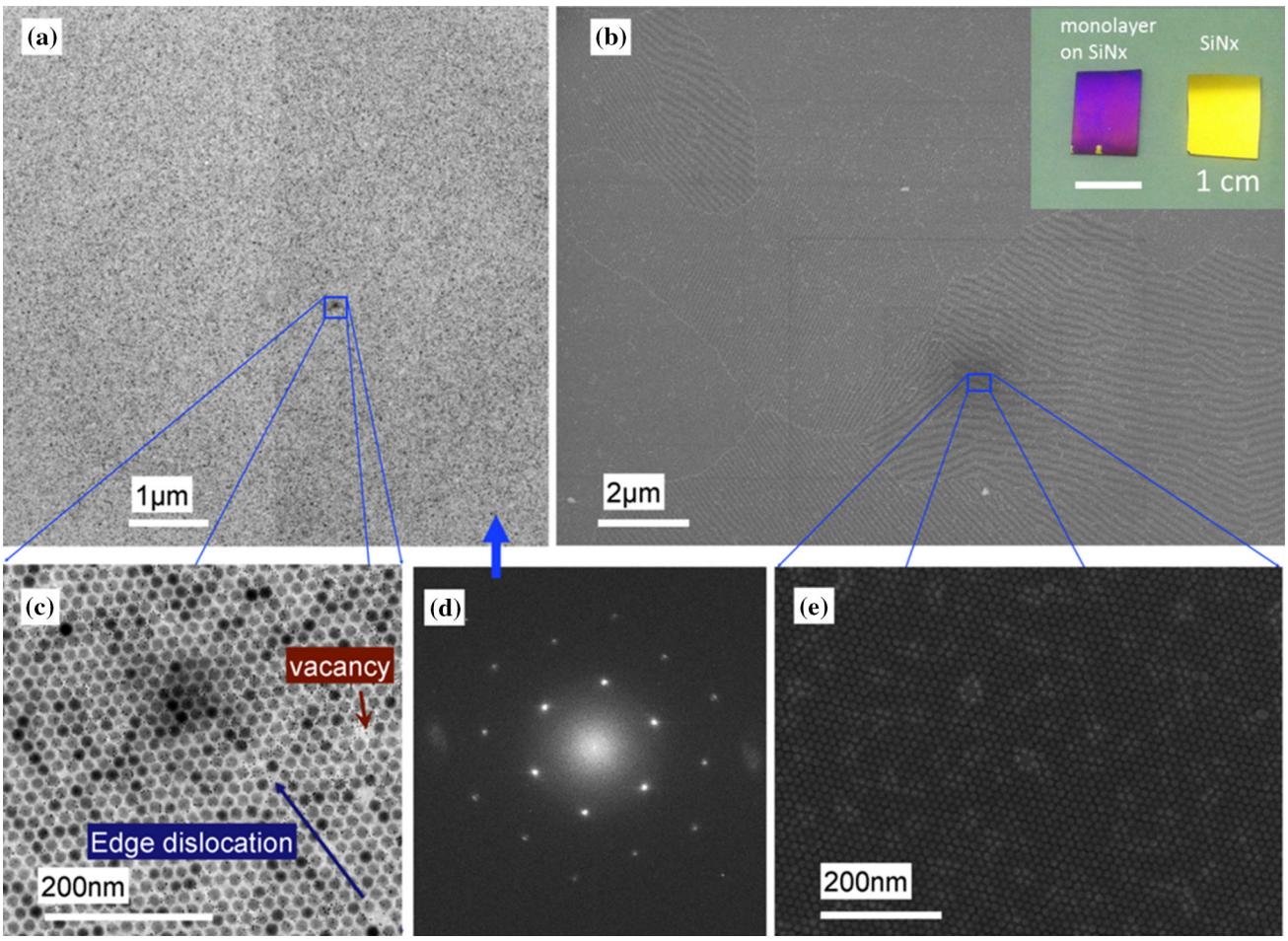

Fig. 14 **a** TEM and **b** SEM images of large-area self-assembled monolayer of ~12 nm Fe_3O_4 nanoparticles, which are magnified in (**c**) and (**e**), respectively. **d** the FFT of the TEM image in (**a**). The *inset* in (**b**) shows the picture of Fe_3O_4 nanoparticle monolayer-coated SiNx thin films. Copyright © American Chemical Society 2011 [55]

stripe patterns at lower magnifications, from which grain boundaries can be clearly identified [55]. The Fe_3O_4 magnetic nanoparticles, black in solution, appear purple when they are self-assembled into monolayers and coated on the yellowish SiN_x thin films on a silicon substrate, as shown in the inset of Fig. 14b. Further, the above self-assembly method can be used to fabricate monolayer of other surfactant-coated colloidal nanoparticles as well, such as gold nanoparticles [55]. It is worth pointing out that monodisperse nanoparticles ($<\sim 5$ %) are needed to make crystalline monolayers with longer range orders [55, 131].

When one monolayer of nanoparticles is superimposed on another, nanoparticle bilayer forms with a rotation angle between the close packed directions of the two set of monolayers [55]. Figure 15a-d shows the TEM image of nanoparticle bilayers with different rotation angles. The FFT of the TEM image in Fig. 15d can be divided into two subsets of hexagonal patterns, which are indicated by the red and blue circles, respectively, in Fig. 15e, g. The inverse transformation of the FFT (IFFT) in Fig. 15e, g gives the images of the two monolayers as shown in Fig. 15f, h, respectively. The rotation angle of the bilayer is calculated by measuring the angle between the close packed directions of the two monolayers as shown in Fig. 15h. The rotation angles of the bilayer in Fig. 15a–d are 0°, 8°, 17°, and 20°, respectively. Moiré fringes can be clearly observed, and the period of the Moiré pattern decreases as the rotation angle increases, which is smallest at rotation angle of 30° due to the sixfold symmetry of the monolayer [132]. By rotating and superposing two dot arrays in computer, the nanoparticle bilayer and Moiré fringe can be simulated with corresponding rotation angles as shown in Fig. 15i–l, which is consistent with the real TEM image in Fig. 15a–d, respectively [55].

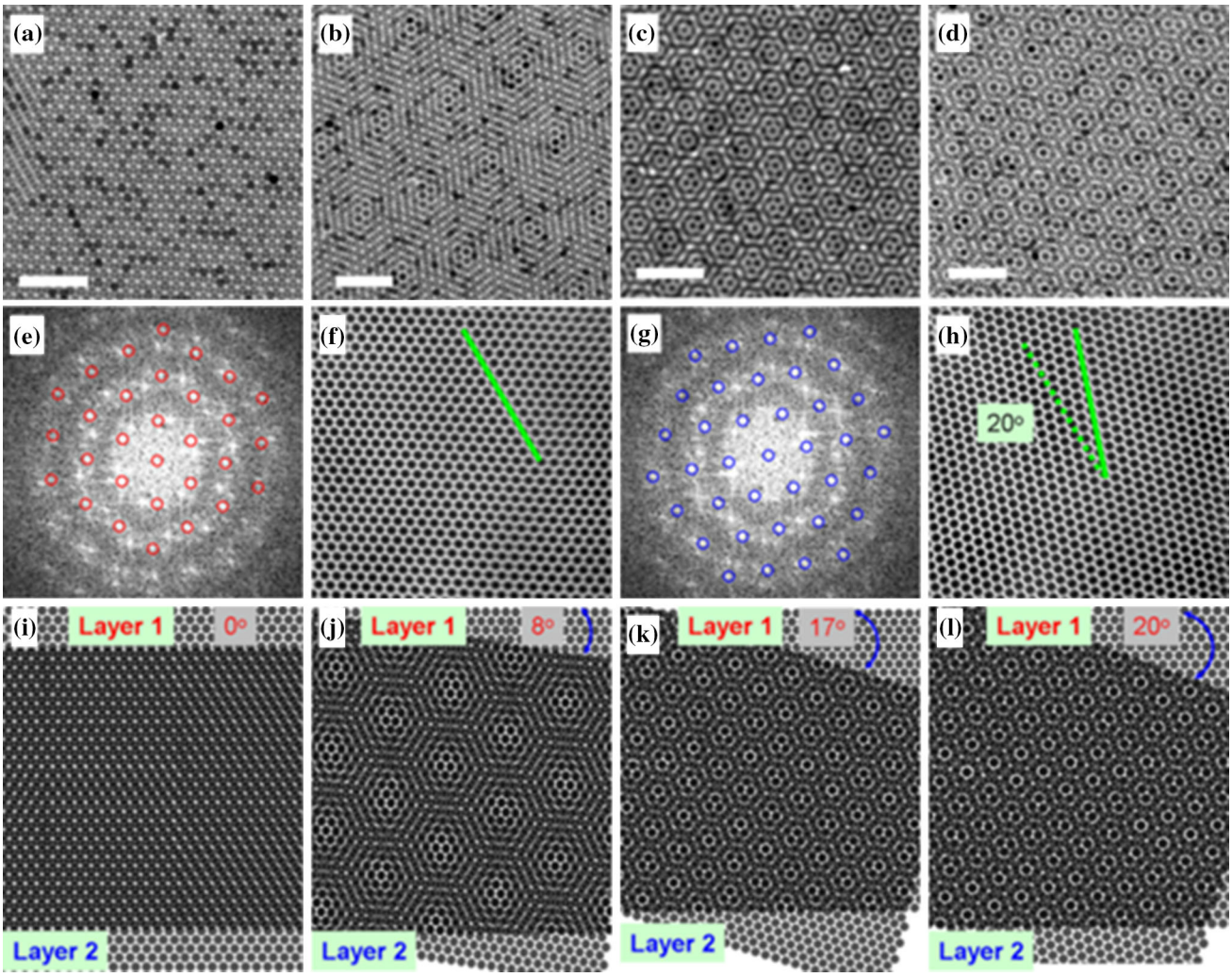

Fig. 15 TEM image of Fe_3O_4 nanoparticle bilayers with different rotation angles in (**a**–**d**) and the corresponding computer simulations in (**i**–**l**), respectively. **e**, **g** the two sets of hexagonal FFT patterns of the two composing monolayer in (**d**), and **f, h** the corresponding IFFT images. Copyright © American Chemical Society 2011 [55]

Nanoparticle monolayers fabricated by the above technique are continuous and uniform over centimeter-length scales, and thus can be considered or used as granular nanoparticle thin films. These nanoparticle monolayer thin films are of great interest for fundamental investigations and use as functional layers in devices [38, 41, 133, 134]. They are also of interest for many other applications such as nanoparticle lithography [135], discussed later in "Nanoparticle lithography" section. Besides the large-area 2D monolayer or bilayer, it is also often required to self-assemble nanoparticles into complex hierarchical structures [136, 137], such as nanoparticle assembly arrays, where assemblies composed of ~millions of nanoparticles are spatially organized in 2D arrays [56]. The combinations of lithographic techniques and convective self-assembly can be used to fulfill requirements of hierarchical self-assembly [43, 48, 50, 56, 119, 138]. Here the lithographic techniques have two important roles, namely, (1) to generate the first layer of the hierarchical structures on the substrates, and (2) affect the movement of the contact line by the lithographic features [48, 56]. The patterns can be generated by photolithography and e-beam lithography. Figure 16 shows an inverted pyramid hole arrays generated by photolithography, followed by wet chemical anisotropic etch. When nanoparticle solution evaporates on the generated hole arrays, the contact line will be pinned at the lithographic features, and nanoparticles will be driven along the meniscus to deposit in the holes by surface tension [48, 56]. As a result, nanoparticles will be preferentially deposited into the holes to generate nanoparticle assembly arrays [50]. However, when large numbers of nanoparticles are contained in each hole, it is nontrivial to fully and uniformly fill the hole arrays over large area [56]. Uncontrolled or improperly controlled evaporation of nanoparticle solutions often results in uneven filling of the hole arrays and inhomogeneous growth of nanoparticle assemblies [56]. Rapid evaporation will not give nanoparticles sufficient time to diffuse and reach their equilibrium positions, resulting in multiple nanoparticle assemblies in one hole and undesired massive deposition on the silicon wall [56]. Simple reduction of evaporation rate by slow pulling often results in partial filling [56].

To generate uniform nanoparticle assembly arrays over large area, the evaporation of the nanoparticle solution on the patterned surface should be properly controlled [56]. First, the evaporation rate should be slow and steady to give nanoparticles sufficient time to move in the lateral directions toward the holes. Second, the evaporation direction should be controlled to allow nanoparticles to move only along the lateral directions to the drying front to feed the nanoparticle deposition in holes [56]. To satisfy these two conditions, a procedure as shown in Fig. 17 is designed and used for the fulfillment of the hierarchical self-assembly of nanoparticles [56]. A drop of colloidal nanoparticle solution was spread on the patterned substrate, which was previously put in a petri-dish. Afterward, a fluorinated polyether plate of low surface energy is then placed on top of the nanoparticle solution. A nanoparticle solution layer is formed and sandwiched by the patterned substrate and the polymer plate. The petri-dish is then partially covered by a glass slide, as shown in Fig. 17. By doing this, the carrier fluid only evaporates toward the opening along the slit between the polymer plate and the substrate. In this process, the evaporation rate is reduced by the cover of polymer plate and the glass slide, giving nanoparticles sufficient time for movement. At the same time, the movement direction of nanoparticles in the carrier solution is also controlled by the evaporation direction of carrier fluid, which keeps driving nanoparticles in the solution reservoir to the drying front. As a result, the growth of nanoparticle assemblies in the hole can be continuously fed. After completion of evaporation, most nanoparticles are deposited in the holes, and sporadic nanoparticles deposited on the silicon wall are then removed by gentle polish [56].

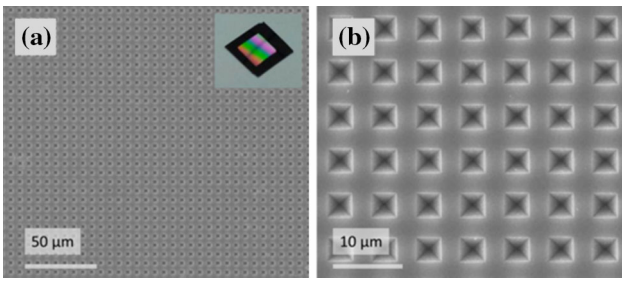

Fig. 16 **a** lower and **b** higher magnifications of the inverted pyramid hole arrays on silicon substrate characterized by SEM. The *inset* in (**a**) shows the SEM image of the patterned area. Copyright © Royal Chemical Society 2015 [56]

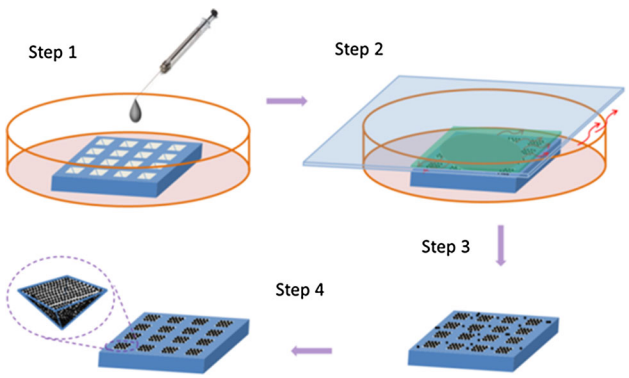

Fig. 17 Procedure for fabricating $CoFe_2O_4$ nanoparticle assembly arrays. Copyright © Royal Chemical Society 2015 [56]

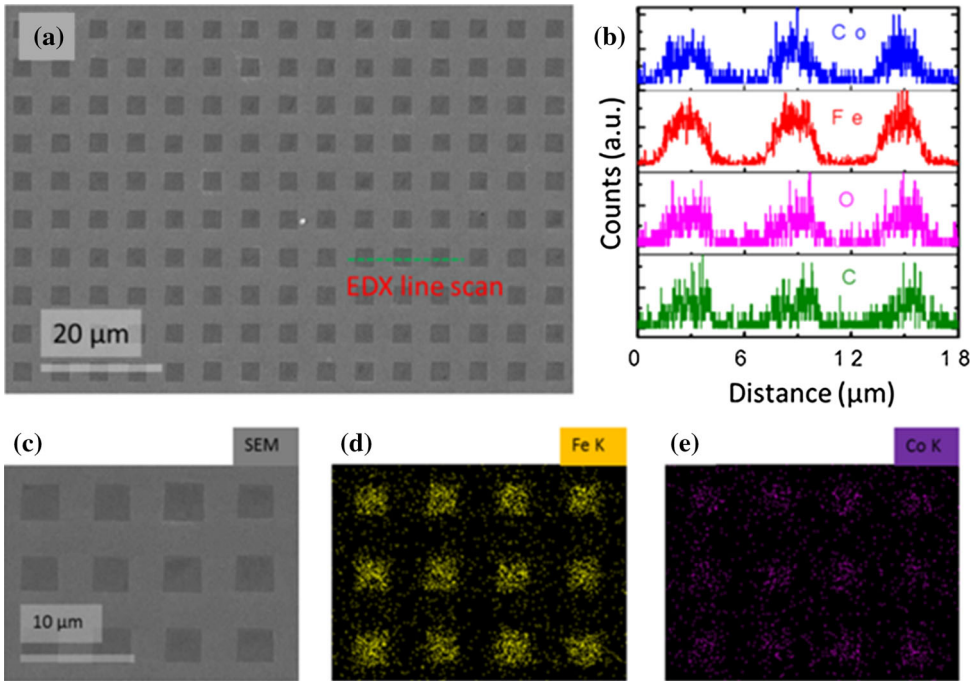

Fig. 18 **a** SEM image of 2D arrays of pyramid cobalt ferrite nanoparticle assemblies, the EDX line scan performed along the *green line* in (**a**) is shown in (**b**). **c**–**e** the SEM, the iron and cobalt mappings in a 4 × 3 matrix of pyramid nanoparticle assemblies, respectively. Copyright © Royal Chemical Society 2015 [56] (Color figure online)

Figure 18a shows a SEM image of pyramid nanoparticle assembly arrays over large areas. It is clear that the pyramid holes are completely filled by nanoparticles. No nanoparticles are found on the silicon wall by high-resolution image [56]. A focused electron beam was scanned along the green line as shown in Fig. 18a to perform energy dispersive X-ray spectroscopy (EDX) for element analysis. The corresponding concentration profiles of iron, cobalt, oxygen, and carbon are shown in Fig. 18b. The cobalt, iron, and oxygen signals are from cobalt ferrite nanoparticles, and carbon is from the surfactants coated on nanoparticles. The periodic concentration profile corresponds to the periodic structures of pyramid nanoparticle assembly arrays. The element mappings of cobalt and iron in Fig. 18d, e, correspond one-to-one with the SEM images in Fig. 18c. The large-area magnetic nanoparticle assembly arrays allow us to detect the magnetic behavior of nanoparticles in a single assembly by measuring the whole sample [56]. It is found that the magnetic pyramid nanoparticle assemblies can be easily magnetized along the fourfold symmetric axis [56].

As shown above, convective self-assembly is a simple, effective and economical method to engineer the spatial organizations of nanoparticles, exemplified by the 2D monolayer of nanoparticles and 2D array of nanoparticle assemblies. For large-area nanoparticle assembly, it is critical to control the evaporation rate and directions of carrier fluid to achieve uniform deposition of nanoparticles across the whole process. The high-quality nanoparticle assemblies give us additional degrees of freedom in designing the properties of magnetic nanoparticles, which definitely will affect and extend the application of magnetic nanoparticles.

Fabrication of hybrid magnetic composites

The increasing demand for multifunctional materials has led to the development of new and sophisticated composite materials [139–153]. In particular, hybrid structures consisting of magnetic nanoparticles embedded in a polymer matrix have gained interest as a new class of smart materials that combine magnetic field responsive behavior with attractive mechanical properties [145–147, 150, 152]. To date, extensive research has been devoted to the development of high-performance magnetic polymer composites for diverse applications in structural materials engineering and the biosciences [146–148, 152]. Moreover, the development of these materials has drawn attention to the scientific challenges in understanding the underlying physics behind their novel magneto-elastic properties, which is complicated by the collective influence of a variety of factors including materials chemistry of the composite, nanostructure morphology, and interface interactions [148–150]. The study of structure–property relationships in magnetic nanoparticle-reinforced polymer composites is rapidly growing but requires unique synthetic capabilities and high-end characterization tools since the performance of magnetic composite materials not only depends on its microstructure but also on the processing techniques and the influence of the microenvironment during specific applications.

Elastomers represent an important class of soft polymeric materials that exhibit low elastic modulus [151]. When magnetic nanoparticles are mixed with an elastomeric polymer, such as poly(vinyl alcohol)-based hydrogel [152, 153] or silicone rubber [152], the resulting magnetic polymer composite can demonstrate controlled stretching, contraction, and bending deformations under the influence of an external magnetic field. Tuning the orientation and magnitude of the external magnetic field can control the deformation motions and the variations in the composite material's tensile strength, compression, and shear moduli, thereby making them ideal materials for developing dampers in the automotive industry, rotating tools for machineries, and mixing pumps in microfluidic devices [147, 150]. Basically, there are two general types of magnetic nanoparticle-loaded elastomers: the first are isotropic magnetic polymer composites that have uniform spatial distribution of magnetic nanoparticle fillers, and the second are anisotropic composites characterized by uniaxially ordered filler nanoparticles (Fig. 19) [145]. An anisotropic system can be prepared by fabricating elastomers/magnetic nanoparticle composites under a uniform magnetic field (Fig. 19a). The anisotropy manifests itself in the direction-dependent elastic modulus (Fig. 19b). The elastic modulus can be increased if the direction of the magnetically aligned nanoparticle chain and the compression force are parallel. This finding, demonstrated by Filipcsei et al., suggests that strong mechanical anisotropy can be affected by incorporating chains of nanoparticles [145]. The spatial distribution of the magnetic nanoparticles has a decisive effect on the stress–strain dependence of the composites. When the direction of the compressive force is parallel or perpendicular to the magnetic nanoparticle chain structure, a deviation from the ideal mechanical behavior can be observed. This kind of mechanical behavior can be described by the Mooney–Rivlin equation with $C_2 < 0$:

$$W = C_1\left(\lambda_x^2 + \lambda_y^2 + \lambda_z^2 - 3\right) + C_2\left(\lambda_x^2\lambda_y^2 + \lambda_y^2\lambda_z^2 + \lambda_z^2\lambda_x^2 - 3\right)$$

where W is the work stored as strain energy, λ is the elongation of the original sample, and C_1 and C_2 are the materials constants. Similarly, it has been recently demonstrated that by using superparamagnetic iron oxide-coated reinforcement particles, ultralow magnetic fields can be utilized to precisely control the position and orientation of reinforcing particles within the polymer matrix, to give rise to a myriad of properties including out-of-plane global or local increase in composite stiffness, strength, hardness, wear resistance, and shape memory effects [145].

To facilitate the incorporation of magnetic nanoparticles into the polymer matrix, several well-known polymerization techniques have been optimized and utilized for grafting various types of polymer brushes on magnetic nanoparticles [154–159], which include grafting-to polymerization methods using click chemistry techniques [160], ring-opening polymerizations [161], and controlled radical polymerization methods [162–164]. In particular, the controlled radical polymerization approaches, such as reversible addition–fragmentation chain transfer polymerization (RAFT) and atom-transfer radical polymerization (ATRP), have been shown to produce well-defined and dispersed polymer-coated magnetic nanoparticles. Polymer brushes have been successfully grafted onto various types of nanoparticles using RAFT and ATRP methods, which facilitate the introduction of a large variety of polymers such as poly(methyl acrylate), poly(methyl methacrylate), poly(acrylic acid), and poly(*N*-isopropyl acrylamide) of controlled molecular weights on the nanoparticle surface [165]. In addition, through surface-initiated ring opening polymerization (ROP), polymer brushes such as poly-ε-caprolactone and poly(lactic acid) have been successfully grafted and grown on the surface of magnetic nanoparticles without polymer branching or abrupt termination of the polymerization process [161]. Moreover, block-copolymers with alkyne-terminating groups have been grafted on the surface of magnetic nanoparticles containing azide functionality via Cu-catalyzed click chemistry techniques [160].

The coating of polymer shells on the surface of magnetic nanoparticles has also made the construction of higher-order hierarchical structures possible. Using the seeded emulsion polymerization technique, clusters of

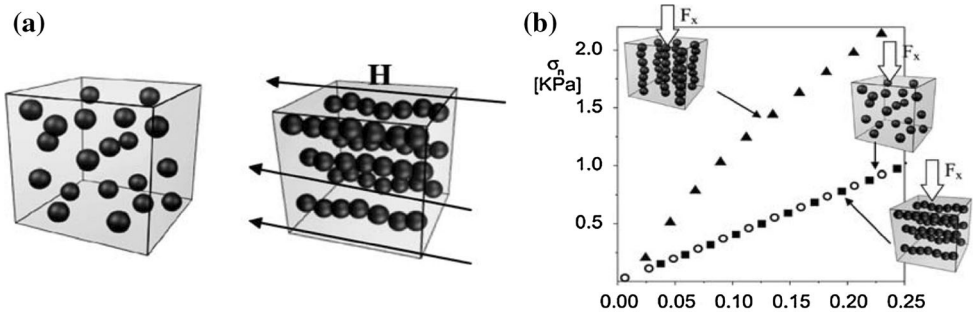

Fig. 19 **a** Magnetic composites showing isotropic and anisotropic particle distribution, respectively. **b** Anisotropic behavior of a magnetic nanoparticle reinforced elastomer; the *arrows* represent direction of compressive force. Copyright © Springer 2007 [145]

magnetic nanoparticles have been encapsulated within polymer matrixes. Through adjustment of the concentration of the emulsifier, the size of the emulsion micelle containing monomers and magnetic nanoparticles can be controlled [166–169]. With the introduction of an initiator and a crosslinking agent, the monomers are polymerized and crosslinked inside a stable polymer shell, which locks the cluster of magnetic nanoparticles in place [167]. The resulting magnetic nanoclusters have been shown to exhibit optimized MRI contrast enhancement and improved response in magnetic hyperthermia applications [167].

Magnetic composites made from thermoplastic polymers can also be fabricated using various processing methods, such as compression molding [170], melt compounding [171], solution casting [172], and melt extrusion [173]. In the fabrication of magnetic thermoplastics, particle agglomeration has been a consistent challenge, and alternative approaches have been introduced by using core–shell magnetic polymer nanoparticles with increased stability to prevent aggregation [172]. Iron oxide nanoparticles have been incorporated into an ultrahigh molecular weight polyethylene (UHMWPE) matrix as a platform to study the effects of interparticle interaction on the AC magnetic field response of iron oxide nanoparticles. The general use of UHMWPE as a composite matrix remains a challenge due to difficulties in processing. The extremely high molecular weight of this polymer makes it unprocessable by conventional thermoplastic processing techniques, and dispersion of magnetic nanoparticle fillers has been a serious challenge due to the polymer's extremely high viscosity. With decreasing particle size, the ratio of surface/volume increases, and the surface properties of the nanoparticles become a major factor in influencing its interfacial properties and agglomeration behavior. Therefore, to adjust the composite material's processability and properties, tailoring of the magnetic nanoparticle surface as well as tuning of the interfacial layer between the particle and the polymer matrix is crucial. The degree of particle agglomeration can, however, be further influenced by utilizing dispersants, which strongly influence the composite rheology because of the reduction in interparticle friction. For example, Bin et al. have successfully prepared multiwalled carbon nanotube (MWCT)-reinforced UHMWPE using decalin and paraffin as MWCT dispersants and have observed high stiffness and electrical conductivity in the fabricated composites [174]. On the other hand, Rong et al. have grafted styrene monomers on the surface of 7-nm-sized SiO_2 nanoparticles before mixing them with the polypropylene matrix [175]. This technique produced samples with no significant aggregation and, in addition, greatly increased the particle–polymer matrix interfacial interactions. It was also evident from the studies of Guoliang et al. that the liquid–solid mechanical dispersing method is better than the dry powder direct mechanical mixing approach in producing composites with better mechanical properties, owing to better particle distribution in the former method [176].

Consequently, to produce magnetic UHMWPE composite films with good particle dispersity, a liquid–solid mechanical mixing approach was adapted to fabricate magnetic UHMWPE composites. A high-speed blade mixer was first used to blend the magnetite nanoparticles with UHMWPE in the presence of an organic solvent dispersant. This approach has been successfully utilized in the processing of Al_2O_3 nanoparticle-reinforced PEEK polymer [176] and in carbon nanotube-reinforced UHMWPE [174]. To prepare magnetic composite films, the resulting UHMWPE and iron oxide magnetic powder blend was compression molded between layers of PTFE sheets and iron steel plates in a Carver Model laboratory press under seven metric ton of pressure (Fig. 20) [177]. In order to determine the optimal temperature for fabrication, the melting temperature of UHMWPE was evaluated using differential scanning calorimetry (DSC), and the oxidative degradation of the polymer matrix was examined using attenuated total reflectance-FTIR spectroscopy (ATR-FTIR). To ensure that the polymer is in its molten state for the fabrication process while maintaining minimal oxidative degradation, the optimal fabrication temperature was chosen to be 200 °C. Comparing the mechanical properties of the magnetic polyethylene composite fabricated using the optimized liquid-compounding method to that of the composite fabricated using the typical dry mixing method, there is a significant increase in elastic modulus with the liquid-compounding method. This can be explained by the improved nanoparticle dispersity within the polyethylene matrix owing to the presence of the organic solvent during mixing (Fig. 21a). The field-dependent magnetic properties of the uncompressed (prior to compression molding) and compression-molded magnetic nanoparticle–polyethylene composites containing 0.5 % Fe_3O_4 nanoparticles were essentially unchanged during the processing step (Fig. 21b). The magnetic hysteresis data obtained at 300 K reveal zero coercivity and remanence (inset, Fig. 21b), which demonstrates that the magnetic nanoparticles are superparamagnetic at room temperature even after being embedded in the UHMWPE matrix. From these results, it can be inferred that the morphology and superparamagnetic properties of the nanoparticles were preserved in the composite film, indicative of the resiliency of the nanoparticles while being subjected to high-temperature and -pressure conditions during the compression-molding stage.

Using the liquid–solid processing method, different percentages of magnetic nanoparticles could be

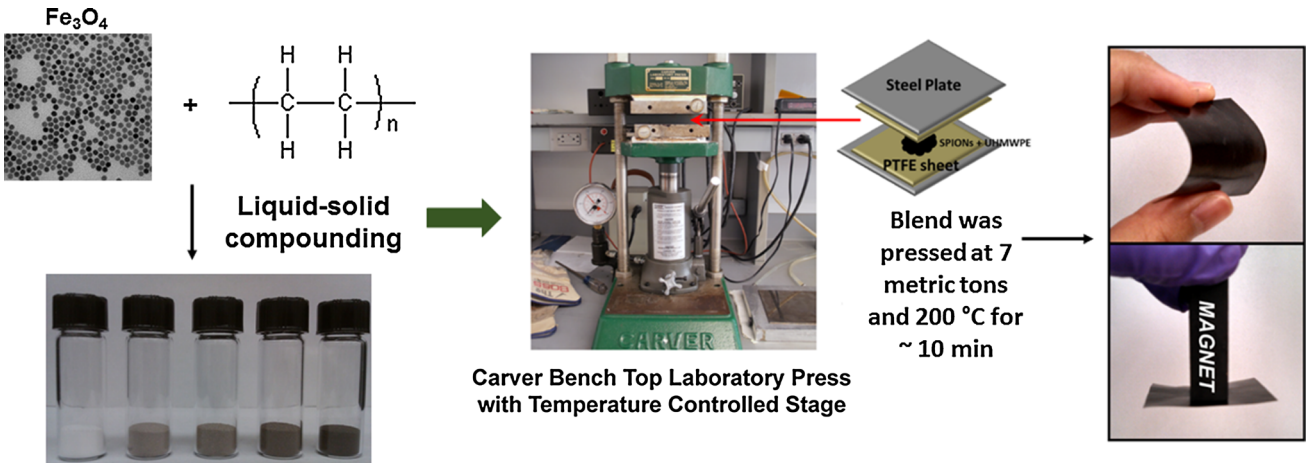

Fig. 20 Fabrication process for the magnetic UHMWPE composite involving a liquid–solid compounding and compression-molding approach. Copyright © Royal Society of Chemistry 2013 [177]

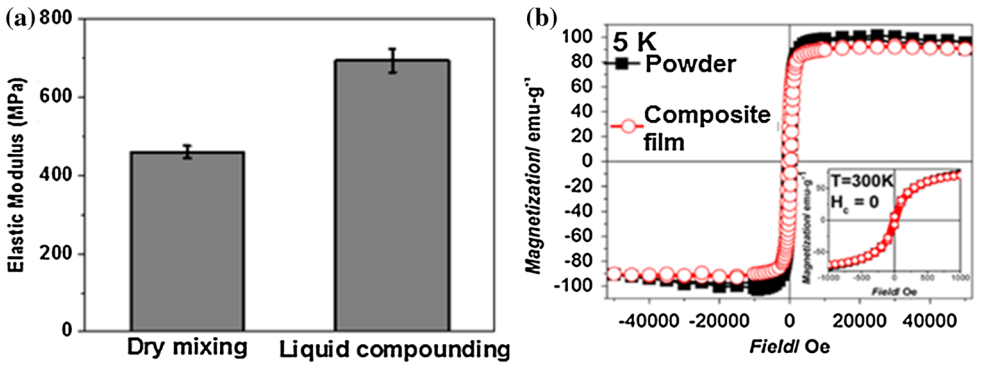

Fig. 21 **a** Elastic modulus of fabricated magnetic UHMWPE composite films. **b** Magnetic hysteresis curves taken at 5 K for a sample containing 0.5 % Fe_3O_4 nanoparticles mixed with UHMWPE powder (Fe_3O_4-NP + PE) and a corresponding magnetite–polyethylene composite film with the same amount of loaded magnetic nanoparticles

incorporated into the UHMWPE matrix (Fig. 22a). As anticipated, improved heating profiles, which can be exploited for magnetic hyperthermia applications, were observed with increasing magnetic nanoparticle loadings upon AC field excitation (Fig. 22b). However, the overall elastic modulus and tensile strength of the magnetic polyethylene composite decreased with the increasing nanoparticle loadings (Fig. 22c).

To overcome this challenge, a hydrothermal carbon-coating approach was employed to improve the polymer–iron oxide nanoparticle interfacial interactions (Fig. 23a). To form the carbon-coated iron oxide nanoparticles, antiferromagnetic FeO nanoparticles were used as co-reagents in the hydrothermal carbonization of glucose. The FeO nanoparticle and glucose mixture was treated under hydrothermal conditions for 2–12 h at 180 °C (Fig. 23b) [143]. During the HTC process, the FeO precursor nanoparticles slowly oxidized into ferrimagnetic Fe_3O_4 nanoparticles, leading to enhanced magnetic dipole interparticle interactions that facilitated the formation of short length iron oxide nanoparticle chain like assemblies [143]. The resulting carbon-coated iron oxide chains were then blended into the UHMWPE matrix, and this has led to improved mechanical properties of the magnetic polymer composites (Fig. 23c, d).

Similar to the behavior of ferrofluids at elevated temperatures, magnetic polymer composites exhibit superparamagnetic characteristics [145], but in contrast to magnetic fluids, the positions of the magnetic nanoparticles embedded into the polymer are rigidly fixed and particle motion is hindered. In magnetic polymer composites, the nanoparticles are trapped by the polymer network; therefore, the Brownian rotation is restricted, and the Néel relaxation is the dominating magnetic relaxation mechanism. Assuming that the particles do not interact, the magnetic behavior of the superparamagnetic material can be described by the Langevin function [5]. As such, the magnetic UHMWPE composite is a good platform for studying magnetic relaxation effects that de-couple the influence of Brownian motions.

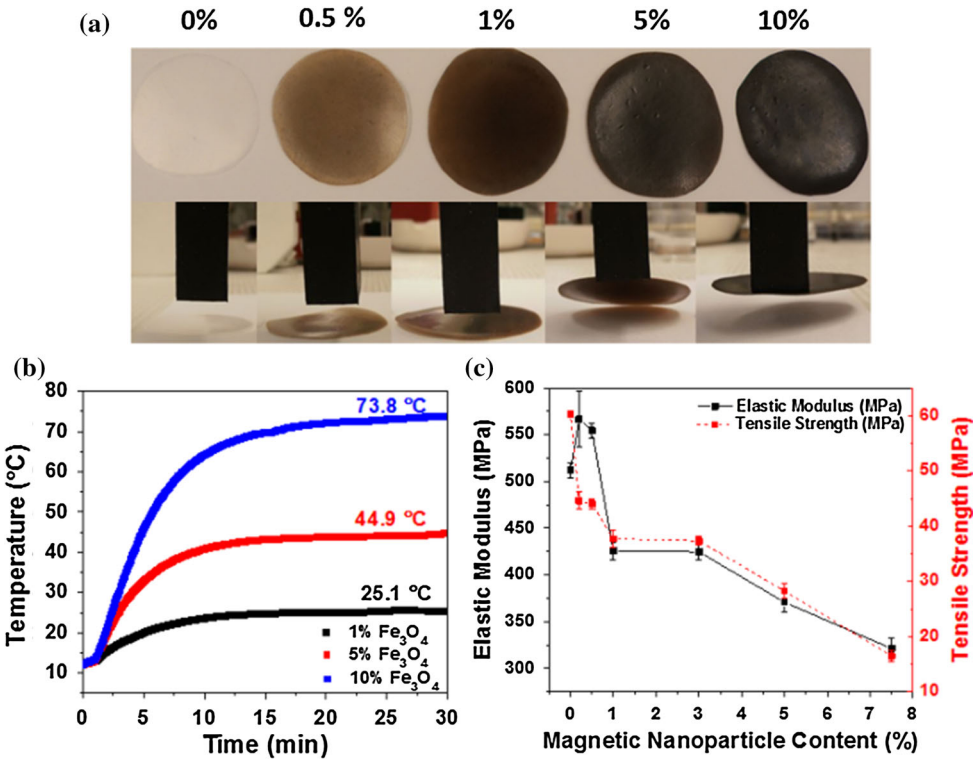

Fig. 22 **a** Photographs of the fabricated magnetic UHMWPE composites with 0, 0.5, 1, 5, and 10 % magnetite nanoparticle loadings. **b** Temperature profiles of the magnetic polymer composites with 1, 5, and 10 % magnetite nanoparticles upon excitation with AC magnetic field at a frequency of 380 kHz and field amplitude of 30 kA/m, and the corresponding mechanical properties of the magnetic polymer composites (**c**)

Surface engineering of nanoparticles

A nanoparticle must be stabilized with capping molecules to reduce the surface energy and maintain its nanoscale size; otherwise, aggregation will occur. Beyond the stabilization, the capping molecules are critical to their applications. For instance, the water solubility and surface functionality of nanoparticles are key parameters affecting their interactions with biological systems. The surface coating, in particular, directly affects nanoparticle cellular uptake [69], biodistribution [70], blood circulation [71], and metabolism [72] (see "Pharmacokinetic pathways of iron oxide nanoparticles" section). As discussed in previous sections, the high-quality iron oxide nanoparticles with controlled size distribution, crystallinity, and magnetic properties are normally produced in organic solvents at high temperatures [87–91]. Therefore, surface engineering is essential to achieve nanoparticle water solubility as well as further conjugation and functionality for biomedical applications.

The as-synthesized iron oxide nanoparticles, such as the nanoparticles prepared by the "heat-up" method (see "Size and shape control of iron oxide nanoparticles" section), are only soluble in organic solvents, and further surface modification is necessary for biomedical applications. Among various surface-functionalization strategies, the ligand exchange method has been highly attractive, because it removes the original hydrophobic coating and subsequently reduce potential toxicity effects on biological systems. Introducing a weakly binding ligand, such as TOPO molecules in the heat-up synthesis method, on the nanoparticle surface was critical to ensure effective exchange [92]. Various molecules have been used to replace the surface hydrophobic coatings, such as polyethylenimine (PEI), polyacrylic acid (PAA), and glutathione (GSH). These molecules not only provided water solubility to the nanoparticles, but also offered carboxylic acid (–COOH) or amino ($–NH_2$) groups for further biomolecule conjugation. The biomolecule conjugations to the nanoparticles with carboxylic or amino groups are normally done via linker chemistry such as carbodiimide (EDC) chemical linker and N-hydroxylsuccinimide (NHS) ester crosslinker. Even though chemical linker conjugation is effective, the chemical linker approach suffers several disadvantages. First, special reaction conditions are normally required for effective conjugation, such as acidic condition (pH 4.5–5.5) in adapting the carbodiimide (EDC) chemical linker, basic condition (pH 7.2–8.0) at low temperature (4 °C) with the use of a N-hydroxylsuccinimide (NHS) ester crosslinker, and reducing condition for maleimide chemistry. Second, low conjugation efficiency is always a concern because of competing reactions. For example, the EDC linker directly links carboxylic acid and amino groups, for conjugating molecules with multiple carboxylic acid and amino moieties (e.g., proteins), EDC chemistry always causes cross conjugation, thus, significantly decreasing the conjugation efficiency. Finally,

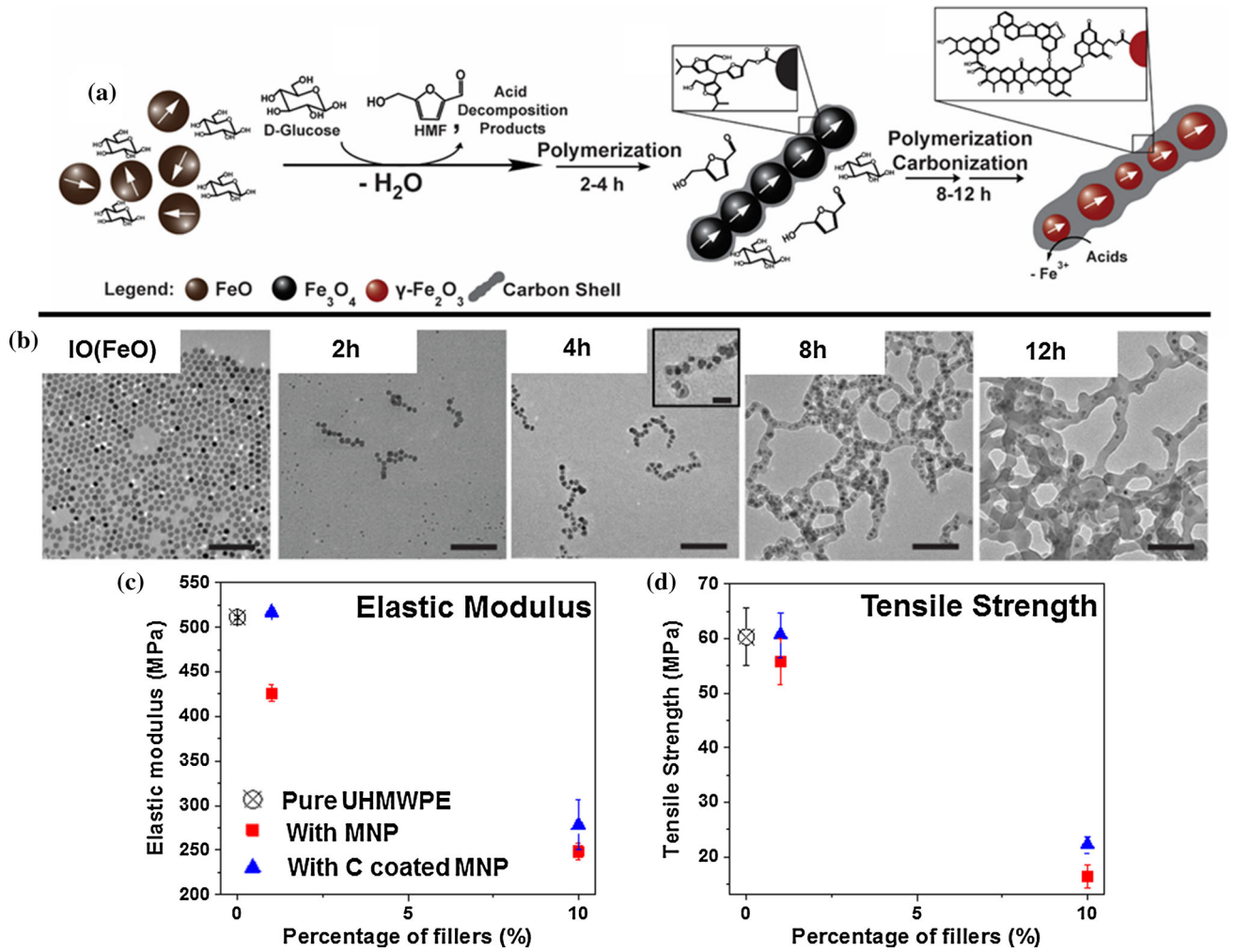

Fig. 23 **a** Schematic of the hydrothermal carbonization approach used to prepare carbon=coated iron oxide magnetic nanoparticles (MNPs). **b** Corresponding TEM images of the precursor FeO nanoparticles and the carbon-coated MNPs synthesized at different times. **c** Elastic modulus, and **d** tensile strength of pure UHMWPE film, composite films with MNPs, and carbon-coated MNPs. Copyright © American Chemical Society 2014 [143]

multiple cleaning steps are necessary to remove the excess chemical linkers and other co-reagents.

Besides the molecular linker chemistry, specific recognition based on biotin–streptavidin is another common strategy [178]. Biotin–avidin interaction requires prior attachment of biotin molecules on the nanoparticles. The biotin-labeled nanoparticles will react with any biotin-binding protein, reducing the specificity. In addition, biotin is a natural biological molecule, causing a big concern about the specificity and background effects when involving biotin-rich tissues and extracts (e.g., brain, liver, milk, or eggs)[2] [179].

Recently, catechol surface conjugation has attracted much attention because catechol can be easily activated by raising the solution pH and the activated catechol groups can directly interact with biomolecules with no need of chemical linkers [64, 93]. The catechol groups were introduced onto iron oxide nanoparticle surfaces by using dopamine as an exchange ligand, where the amino group of the dopamine molecule attach to the iron oxide nanoparticle surfaces, leaving the catechol group out (Fig. 24). The catechol groups on the nanoparticle surfaces can be easily oxidized into dopamine quinone at higher pH (>8.5), creating an active surface for further conjugation. The activated dopamine groups will allow for the direct conjugation of biological molecules containing amino and/or thiol groups through Michael addition and/or Schiff base formation (Fig. 24) [180, 181].

Figure 25a shows the TEM image of dopamine-coated iron oxide nanoparticles in water. The presence of dopamine on the nanoparticle surface and the subsequent

[2] http://www.piercenet.com/browse.cfm?fldID=4A957146-5056-8A76-4E97-81995432210B.

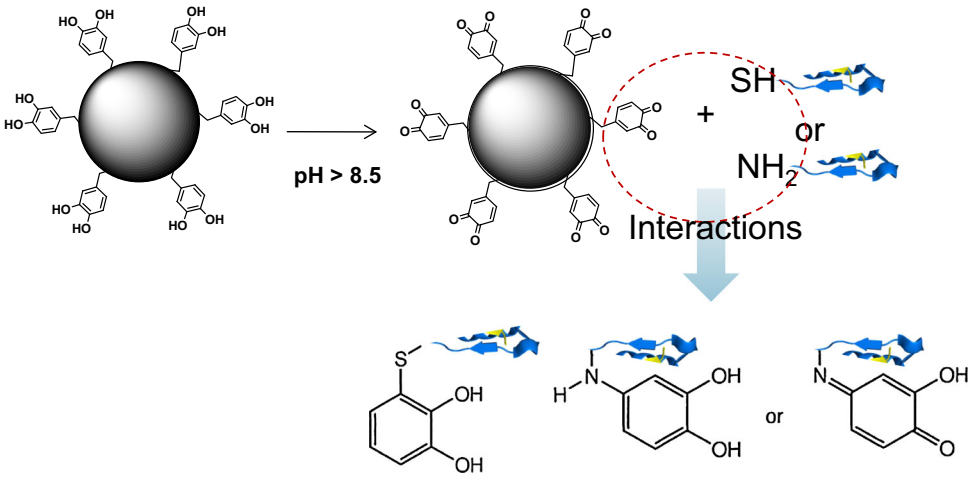

Fig. 24 A schematic drawing to illustrate the conjugation process

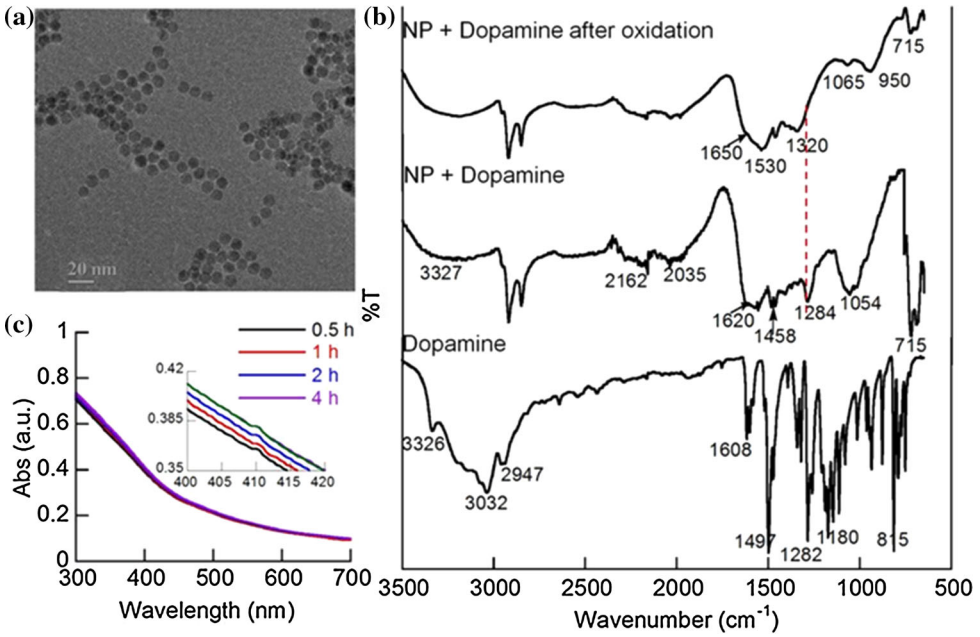

Fig. 25 **a** TEM image of the dopamine-coated iron oxide nanoparticles (10 nm), **b** FTIR spectra of free dopamine, dopamine-coated, and activated dopamine-coated nanoparticles, and **c** time-dependent UV–Vis spectra of dopamine-coated iron oxide nanoparticles after activation. Copyright © American Chemical Society 2012 [64]

activation were studied using FTIR (Fig. 25b). Compared to that of the free dopamine, the FTIR spectrum of dopamine-coated nanoparticles showed several band shifts related to the primary amine group. The two $-NH_2$ stretching peaks of the free dopamine in the range of 3200–3400 cm^{-1} became a single broad peak at 3327 cm^{-1} after interacting with iron oxide nanoparticles. This broad peak is likely merged with the hydroxyl stretching band in the similar region. After interacting with iron oxide nanoparticles, the dopamine $-NH_2$ bending (1577 and 1469 cm^{-1}) merged together with the –C=C– stretching in the range of 1460–1617 cm^{-1} and a much broader peak was observed. Further, the band of the $-NH_2$ wagging (815 cm^{-1}) [182] shifted to a lower wavelength, another indicator of the attachment of amino groups to the nanoparticle surfaces.

The characteristic band of the –C–O stretching (1282 cm^{-1}) remain unchanged before and after the attachment. After catechol group activation at pH 8.5, the IR spectrum of the activated nanoparticle surface exhibited a broad band at 1650 cm^{-1}, the characteristic of –C=O band in quinone structure [183]. The disappearance of the characteristic band of –C–O at 1282 cm^{-1} is another indicator of the dopamine oxidation. The oxidation process was also monitored with UV–Vis spectroscopy (Fig. 25c). Because of the strong absorption of iron oxide nanoparticles, the absorption of the oxidized dopamine molecules was not well resolved. However, the typical absorption peak (409 nm) of the oxidized dopamine was clearly visible in the detailed scan (Fig. 25c, inset).

To test the conjugation efficiency of the activated dopamine surfaces on nanoparticles, two model systems

were utilized, bovine serum albumin (BSA)-coated fluorescent Au nanoclusters and anti-GD2 antibody [64, 93]. The fluorescence emission of the BSA-coated fluorescent Au nanoclusters is also a quick tool to evaluate the conjugation process, while the antibody conjugation assesses whether the conjugation process will affect the biological activities of the conjugating molecules. For both systems, the conjugation experiments were performed by simply mixing the nanoparticles with activated surfaces with either BSA-Au nanoclusters or anti-GD2 antibody. The conjugated nanoparticles were then magnetically separated out of the solution, washed twice, and then and re-dispersed in water or buffer.

Figure 26 shows the fluorescent emission and excitation plots of fluorescent Au nanoclusters after being conjugated on iron oxide nanoparticles surfaces. The intense fluorescence of the conjugated structured indicated the effective conjugation between BSA and the activated dopamine surfaces. Under UV irradiation, the integrated structure showed bright red color, and the same sample was also highly responsive to a magnet, which also suggested the successful conjugation. The small fluorescent nanoclusters under bright TEM were barely seen, but the high-resolution TEM image of a typical integrated structure showed the presence of a single nanocluster on an iron oxide nanoparticle surface (Fig. 26c). Further, the conjugated nanoclusters were clearly observed in the darkfield image (Fig. 26d). Both the high-resolution TEM observation and the darkfield TEM image also suggested the effective conjugation of BSA-Au nanocluster to the nanoparticle surface.

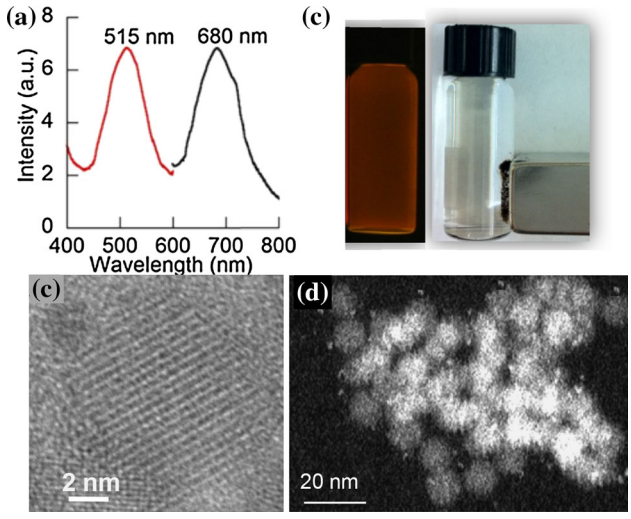

Fig. 26 The integrated structure of iron oxide nanoparticles and Au nanoclusters: **a** fluorescent emission (excited at 520 nm) and excitation scans for 680-nm emission, **b** photographs of the integrated nanostructures under a 365-nm UV radiation and magnetic fields, **c** high-resolution TEM image, **d** darkfield TEM image. Copyright © American Chemical Society 2012 [64]

A great concern for any biomolecule conjugate is whether the conjugation process affects the biological activities of the conjugated molecules. Subsequently, the catechol conjugation method was evaluated by the anti-GD 2 antibody, which specifically recognize GD2 disialoganglioside, an antigen expressed on neuroblastoma cancer cells, most melanomas and a large fraction of small cell lung cancers and other tumors of neuroectodermal origin [184, 185]. Figure 27a shows the negative stained TEM image of the antibody conjugated iron oxide nanoparticles, where antibodies were shown as lighter shells around the nanoparticles. The variation in the shell thickness was due to the different orientations of the antibodies on nanoparticle surfaces. The tiny dark spots around the nanoparticles were from the staining solution, where possible undissolved uranyl acetate stain or lead carbonate precipitation from lead citrate stain absorbed CO_2 from air.

In addition to the TEM visualization, the antibody conjugation was also supported by the zeta-potential shift of the nanoparticles (−44 eV to −34 eV) and hydrodynamic size change (24–34 nm) (Fig. 25b, c). The presence of the protein characteristic amide I (1633 cm^{-1}) and amide II (1520 cm^{-1}) bands clearly suggested the attachment of antibodies. After conjugation, the amine or thiol groups normally attached to the fourth position adjacent to a hydroxyl group through Michael addition and the quinone shifted back to hydroxyl groups. This process was supported by the IR spectrum of antibody-conjugated nanoparticles, where hydroxyl and its C–O bands at 1065 and 1005 cm^{-1} were clearly seen, compared with the strong –CH=CH– ring breathing peak at 956 cm^{-1} (Fig. 26). In fact, the IR bands in the range of 900–1100 cm^{-1} of the antibody conjugated

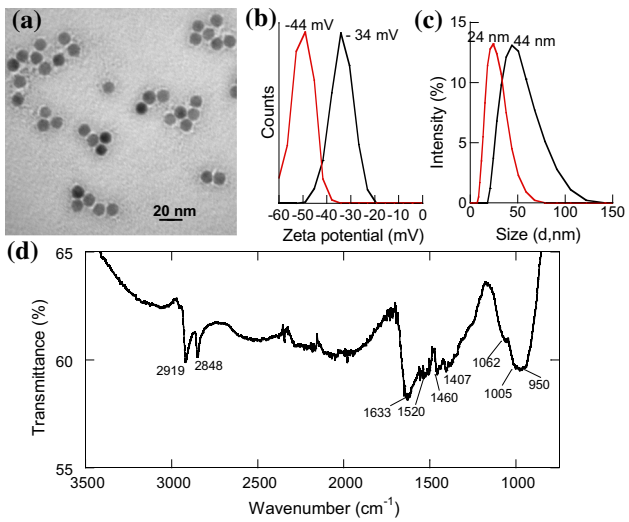

Fig. 27 Antibody-conjugated iron oxide nanoparticles: **a** TEM image, **b** Zeta-potential plots before and after conjugation, **c** DLS plots before and after conjugation, and **d** FTIR spectrum [93]

nanoparticles were very similar to the dopamine-coated nanoparticles before oxidation.

After conjugation, the targeting efficiency of the antibodies on nanoparticles was evaluated on GD2-positive neuroblastoma cells (CHLA-20) and normal fibroblasts. CHLA-20 neuroblastoma cells have a high level of expression of GD2 antigen on the cell surface, while normal fibroblasts do not express the GD2 receptor, serving as a suitable negative control [186]. The localization of the nanoparticles on CHLA-20 cell surface was visualized by fluorescence microscopy using green-fluorescent Alexa 488-labeled antihuman IgG antibody. The lack of green fluorescence after the treatment of cells with unconjugated nanoparticles and antihuman IgG antibody (Fig. 28a) indicated the absence of a nonspecific reaction of the detection system used. Remarkably, the sharp green shell around the cell surface (Fig. 28b) suggested the high level of binding of the antibody-conjugated nanoparticles to GD2-positive cells. In contrast, the antibody-conjugated nanoparticles did not bind to GD2-negative cells (such as normal fibroblasts, Fig. 28c, d), indicating their high specificity of recognizing of GD2 receptors.

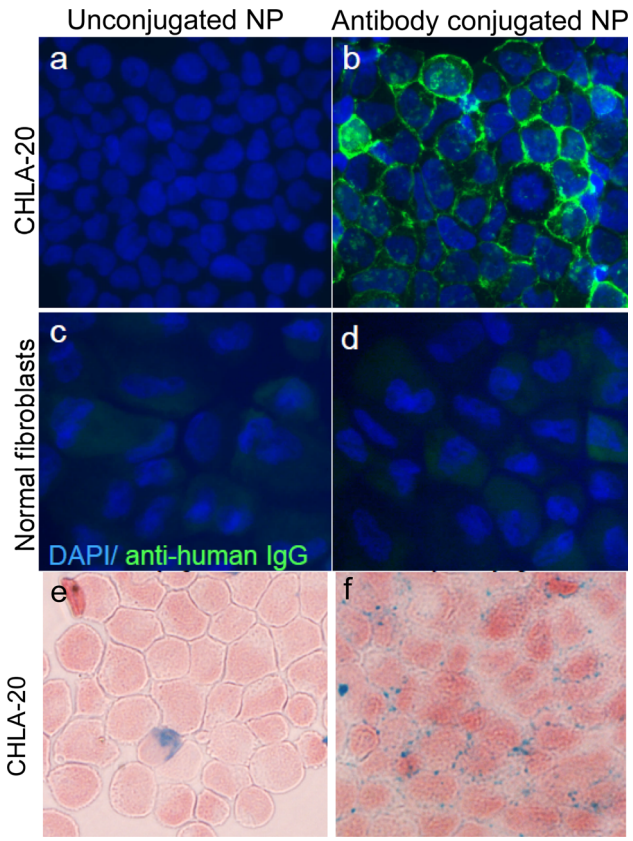

Fig. 28 Binding evaluation of antibody-conjugated iron oxide nanoparticles to neuroblastoma cells (CHLA-20): (Fluorescence microscopy (×400) of CHLA-20 cells or normal fibroblasts treated with unconjugated (**a**, **c**) or antibody-conjugated (**b**, **d**) nanoparticles; and Alexa 488-antihuman IgG antibody, and Perls staining using *Prussian blue* reaction detecting iron for (**e**) unconjugated; and (**f**) antibody-conjugated iron oxide nanoparticles [93]

To confirm the co-localization of the nanoparticles with antibody, Prussian blue iron staining was performed on CHLA-20 cells treated with conjugated and unconjugated nanoparticles. CHLA-20 cells treated with unconjugated, dopamine-coated nanoparticles only showed occasional big blue spots from nanoparticle aggregates (Fig. 28e). In contrast, the cells treated with antibody-conjugated nanoparticles showed clear blue shells around the cells, suggesting the presence of the nanoparticles around the cell membranes (Fig. 28f). In conjunction with the fluorescent microscopy image, this observation suggested the co-localization of nanoparticles and antibodies.

Specific targeting is a key step to realize the full potential of iron oxide nanoparticles in nanomedicine. Facile and effective conjugation of the targeting molecules onto iron oxide nanoparticle surfaces is critically important. The uniquely designed catechol conjugation allows for easy attachment of bioactive molecules onto iron oxide nanoparticles without the need for any type of chemical linkers and maintains the activity of the attached biomolecules. Eliminating the use of chemical linkers significantly simplifies the conjugation process, reduces the requirements of well-trained personnel, and increases the efficiency of the conjugation. Importantly, this conjugation method can be effectively extended to other molecules.

Emerging applications and considerations

Nanoparticle lithography

For applications such as the proposed bit patterned magnetic media [187–189], fabrication of dense nanopatterns with feature size of <20 nm and spacing of a few nanometers is required [41, 190]. Electron beam (e-beam) lithography is problematic to generate small (<10 nm) and dense nanopatterned arrays, where forward scattering of electrons in the resist often broaden the features, and the earlier written features would be affected by latter e-beam writing for dense structures [191, 192]. Besides the technical hurdles, e-beam lithography as a serial process is also very uneconomical and time consuming [193]. Block copolymer self-assembly is proposed and used as an alternative technique to generate these small and dense nanopatterns, which is then transferred into the underlying functional layers [194, 195]. However, as the feature size gets smaller, the driving force for block copolymer self-assembly will be greatly reduced [196]. Further, the self-assembled block copolymer is often a mixture of different morphologies [197]. As shown in self-assembly section, large-area monolayer of nanoparticles can be made by designed convective self-assembly at

the air/liquid interface with colloidal nanoparticles [55]. These nanoparticle arrays are dense and for monodisperse nanoparticles, exhibit good long range order. The feature size is ~10 nm, and the edge-to-edge distance is ~2 nm. As a result, the self-assembled monolayers of nanoparticle is proposed as the 'etch' mask for nanofabrication of 2D dense arrays with feature size <10 nm [41]. Unlike the microsphere particle lithography where the empty spacing between particles is large enough for etchants to penetrate through [120], etchants can hardly reach the underlying films through the ~2 nm spacing between nanoparticles, which is filled with surfactants. The surfactants between nanoparticles can be removed by oxygen plasma. However, it often results in cracking in the ordered monolayer of nanoparticles due to moment transfer from plasma [198]. Although electron treatment can mitigate the cracking, the effect is limited. Further, it is difficult for oxygen plasma to burn the surfactant through to the substrate due to the aspect ratio-dependent etch rate [199]. As a result, instead of using nanoparticle as etching masks, a new etching processing should be developed to transfer the nanopattern of self-assembled monolayer of nanoparticles into the underlying materials.

Electron irradiation can turn surfactants into hydrogenated amorphous carbon [200, 201], which is inert for fluorinated etching process [202]. Hence, surfactants can be used as resist material for e-beam lithography in silicon-based etching [201]. The surfactants around nanoparticle cores, a barrier for nanoparticle mask etch, can be used to transfer the nanopatterns of nanoparticle monolayers by e-beam treatment. Instead of a focused e-beam as in e-beam lithography, the e-beam was spread over large areas to treat all surfactants at one time [135]. By combining self-assembly of nanoparticle and electron treatment, dense and small hole arrays can be fabricated over large area in a parallel process [135]. Figure 29 shows the pattern transfer process using e-beam treatment and fluorinated reactive ion etch (RIE) [135]. The self-assembled monolayer of iron oxide nanoparticles was first treated by e-beam irradiation to turn the surfactant between and on top of nanoparticles into amorphous carbon, as shown in Fig. 29a, b. The surfactants underneath nanoparticles are slightly irradiated due to the shielding from nanoparticles. Afterward, the iron oxide nanoparticle cores were dissolved by hydrochloric acid to leave an amorphous carbon fence on the silicon substrates, as shown in Fig. 29c. The SEM image of the hole arrays of amorphous carbons is shown in Fig. 29g. CF_4 RIE was used to deepen the holes and transfer the pattern into the silicon substrate. The SEM image of the hole arrays in the silicon substrate is shown in Fig. 29h. The nanopattern has been successfully transferred from the self-assembled monolayer of nanoparticle into the silicon substrate by nanoparticle lithography [135].

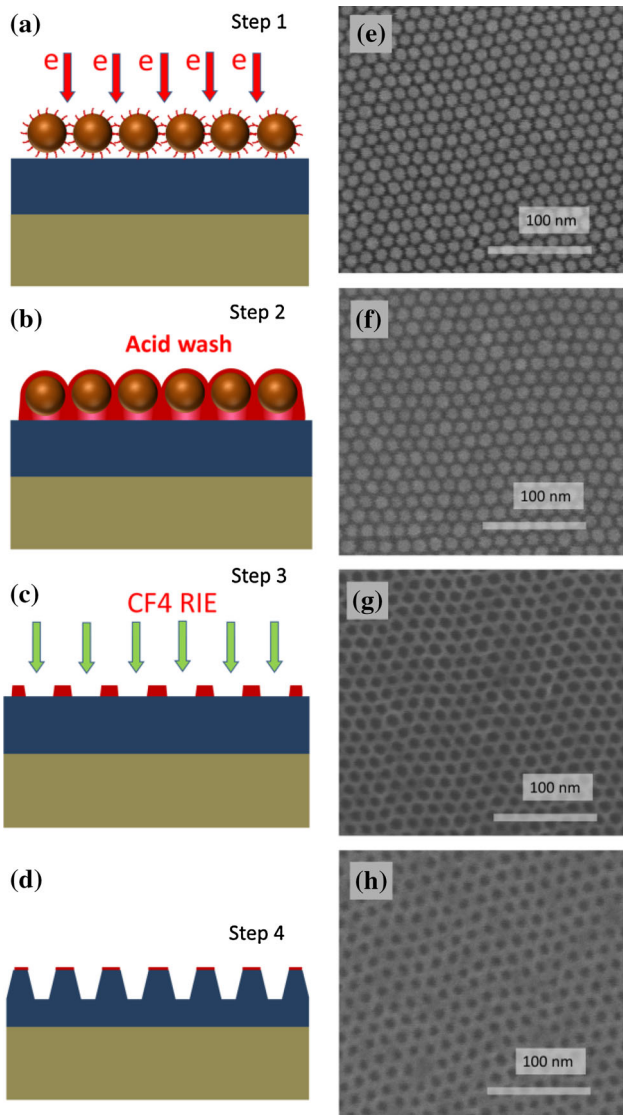

Fig. 29 **a–d** The patterns of transfer process, and **e–h** the corresponding SEM images in each step of the nanoparticle lithography process. Copyright © American Chemical Society 2012 [135]

The pattern transfer fidelity is excellent as shown in the SEM image in Fig. 30. The large grain sizes of self-assembled monolayers of the nanoparticles have been successfully transferred to the hole arrays in the silicon substrate, as shown in Fig. 30a. The hexagonal pattern and the long range order of the hole arrays can be clearly resolved in the SEM image in Fig. 30b, which is magnified from the enclosed area in Fig. 30a. Figure 30c shows the cross section of the hole arrays. The hole size is ~10 nm, and the pitch is ~15 nm. The depth of the holes is ~10 nm. The dense and small hole arrays have been fabricated by the nanoparticle lithography technology. The polycrystalline structures of the self-assembled nanoparticles have also been transferred as shown in Fig. 30d. Different grains show different stripe orientations and

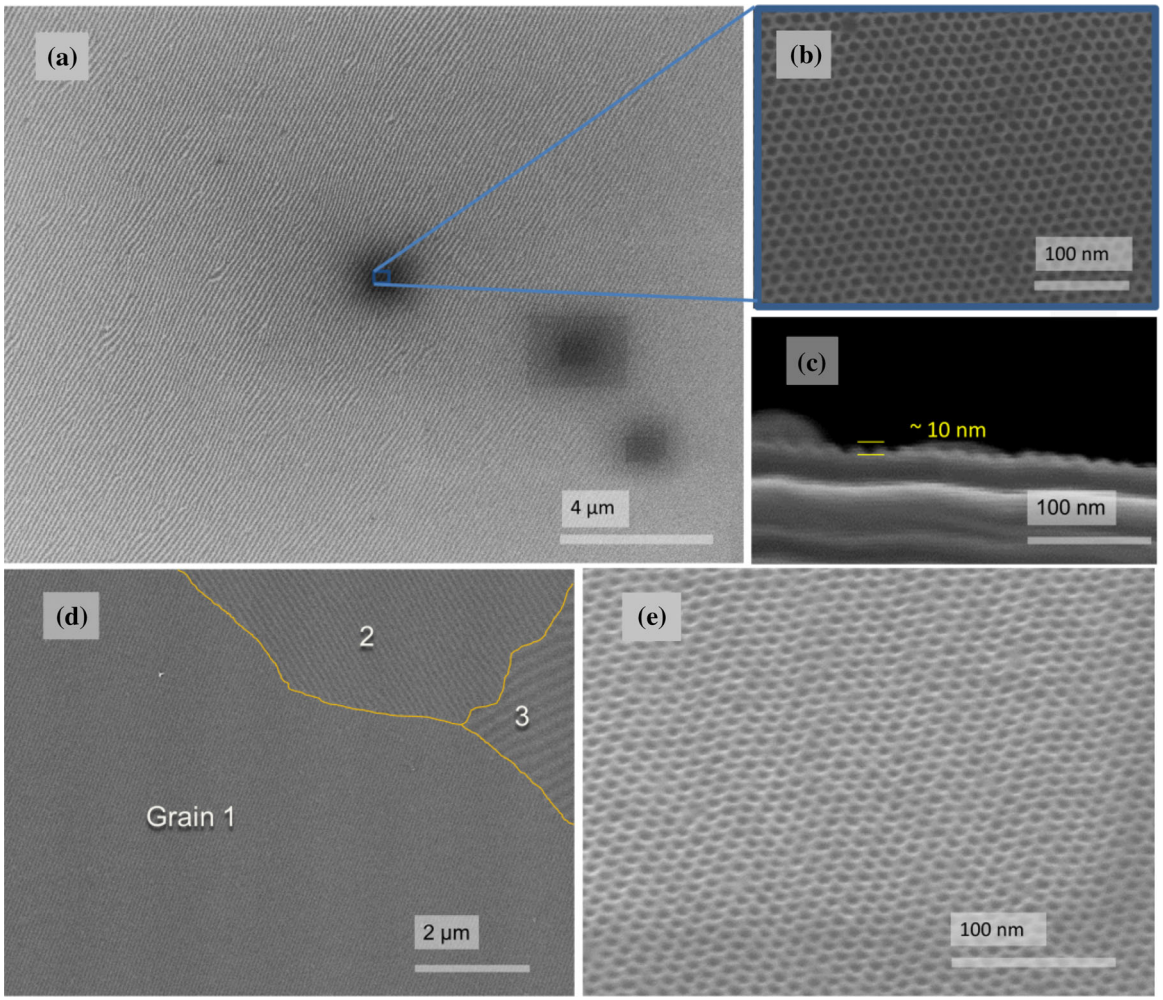

Fig. 30 SEM image of nano-hole arrays. **a** Stripe patterns generated by ~10-nm hole arrays within a grain, and the area enclosed in (**a**) magnified and shown in (**b**). **c** the cross section of the nano hole arrays. **d** the different stripe patterns in different grains. **e** the tilted SEM image of the hole arrays. Copyright © American Chemical Society 2012 [135]

periods, which can be used to differentiate the grain boundaries [135]. The profiles of the holes can be clearly discerned in the tilted SEM image in Fig. 30e.

The curvature of a surface would significantly affect the surface and interface energy [203], which can affect the morphologies of deposited thin films. When gold thin film was deposited on the hole arrays, it is found that gold atoms, originally deposited on the silicon wall, would automatically diffuse toward and fill the holes, resulting in gold nanoparticle arrays on the silicon substrate, as shown in Fig. 31 [135]. The diffusion is driven from convex to concave surface to minimize the surface energy of the system [203]. As the gold thin films grow thicker, gold nanoparticles become bigger with smaller gaps. Besides, the pitch of the gold nanoparticle arrays remains the same [135]. Unlike the nanoparticle arrays fabricated by self-assembly, the gold nanoparticle arrays on the hole arrays have tunable interparticle distances, which might affect their optical properties [204]. Nanoparticle lithography is very competitive over other lithography techniques to fabricate dense arrays with feature size <10 nm. Since the development of nanoparticle lithography is still in its early stage, many technical hurdles should be solved before it can be practically used. The dense arrays are currently transferred onto the silicon substrate by nanoparticle lithography. However, it is desired, although very challenging, to transfer the nanopattern of the self-assembled nanoparticles into functional materials, such as perpendicular FePt thin films. Besides antidot arrays, techniques should also be developed to fabricate dot arrays by nanoparticle lithography.

Magnetic particle imaging

MPI is an emerging tomographic imaging technique based on the magnetic relaxation of superparamagnetic iron oxide

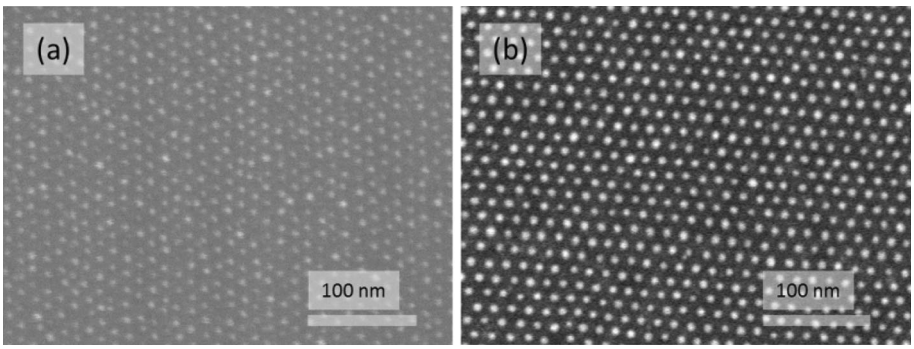

Fig. 31 The gold nanoparticle arrays generated by depositing gold thin film onto the nanohole arrays. The different sizes of gold nanoparticle in (**a**) and (**b**) are due to the different amounts of deposited gold atoms. Copyright © American Chemical Society 2012 [135]

nanoparticles [204–213]. In MPI, the large magnetic moment of the nanoparticles is directly probed rather than simply detecting its indirect effect on the proton relaxation, as in the case with MRI [210]. As such, MPI is fast, quantitative, and features good spatial resolution; a combination that is difficult to realize in the utilization of magnetic nanoparticles in MRI applications [210, 214]. Furthermore, unlike in MRI or in magnetorelaxometry imaging, MPI instrumentation has the potential for being relatively inexpensive because it does not require costly superconducting magnet or SQUID detectors to achieve high sensitivity [210].

In MPI, the magnetic nanoparticles are subjected to an oscillating magnetic field and subsequently show a nonlinear magnetization response. During this process, there are two types of relaxation mechanisms that can affect the alignment of the nanoparticle's magnetic dipoles. Either the magnetic nanoparticle itself undergoes a physical rotation, (Brownian rotation), or the magnetic moment can rotate in a fixed nanoparticle (Néel rotation). The Néel relaxation time, neglecting the applied field amplitude, can be computed by $\tau_N = \tau_0 \exp(K_A V k_B^{-1} T^{-1})$, where K_A is the anisotropy constant, V is the nanoparticle core volume, and k_B and T are the Boltzmann constant and temperature, respectively. On the other hand, the Brownian relaxation can be computed by $\tau_B = (3\eta V_H k_B^{-1} T^{-1})$, where η is the viscosity of the fluid and V_H is the hydrodynamic volume of the nanoparticles. The shorter relaxation time will dominate the behavior of the system. Moreover, the transition frequency between Néel and Brownian will depend on the nanoparticle size and anisotropy, and the viscosity of the medium.

In its very basic form, MPI applies a time-dependent magnetic field (drive field) to change the magnetization of the nanoparticles using transmit coils. In order to detect the change of the magnetization, the magnetic flux density is evaluated by measuring the voltage induced using appropriate receive coils. Due to the nonlinear relationship between the magnetization and the external field, the nanoparticles produce an MPI signal at both the fundamental frequency, and also at higher harmonics [215]. The harmonic signal is linear with the nanoparticle concentration by simple Fourier transform: $S_n = \text{Fourier}\{u(t)\}$; $u(t) \propto -c\{dM(t)/dt\}$ where, S_n is the magnetic nanoparticle harmonics, u is the voltage signal measured in the receive coils, c is the concentration of the magnetic nanoparticles, and M is the magnetization of the nanoparticles. The generation of higher-order harmonics for a nonlinear magnetization curve can be mathematically expressed by expanding the Langevin function into a Taylor series. Since all even derivatives of the Langevin function have a zero crossing point, at which the Taylor series is expanded, the even harmonics are absent, and only odd harmonics are seen in the signal spectrum [215].

For spatial encoding, an additional magnetic field gradient is superimposed onto the drive field such that a field-free point is established within the volume of interest [204–206, 208, 209]. Only particles located in the field-free point (FFP) contribute to the desired signal in the receive coils. Particles outside the FFP are saturated and do not show any further re-magnetization dynamics upon excitation by the drive field. In order to understand the behavior of the superparamagnetic probes in the various applied magnetic fields, a suitable model is needed. It has been shown that the simple Langevin theory of magnetism is capable of describing, to the first order, the important features of the imaging process [207, 209, 210].

To date, MPI studies have been effectively employed to image the real time movement of magnetic nanoparticles through a beating mouse heart [205]. This preclinical result demonstrated the potential of MPI as a valuable tool in cardiac imaging and cardiovascular disease diagnosis. Moreover, several groups have demonstrated that stem cells can be loaded with superparamagnetic iron oxide nanoparticles and be subsequently investigated using MPI [214–216]. With MPI having an anticipated low detection limit, it is conceivable that an MPI system could track a small number of stem cells and propel the development of this area of biomedical research. In addition to stem cells, red blood cells have also been labeled with superparamagnetic iron oxide nanoparticles, with the objective to use human erythrocytes as nanoparticle carriers for MPI tracers to conduct in vivo monitoring of blood circulation. A study

by Markov et al. [217] used red blood cells loaded with Resovist and Sinerem to generate the MPS signal. In addition to exhibiting an MPI signal, the magnetic tracer-loaded red blood cells evidenced a long blood half-life, which makes them especially suitable for imaging of the circulatory system.

Various applications of MPI, including cardiovascular imaging, sentinel lymph node biopsy (SLNB), and stem-cell tracking, have been actively pursued in various research groups [33, 65]. Moreover, the potential application of MPI in examining composite polymer biomaterials have been explored. In particular, we are working toward the use of MPI as a unique tool to characterize the in situ wear debris formation of magnetic polymer nanocomposites based on UHMWPE, which is used heavily in the fabrication of artificial joints (Fig. 32) [177]. The incorporation of superparamagnetic iron oxide nanoparticle inclusions into UHMWPE-based composite materials will enable us to attain magnetic signatures that can be exploited for the in situ monitoring of the wear debris formation of the material in various chemical and biological fluid environments. An improved spatio-temporal assessment of the structural integrity of the polyethylene material used in implants that is subjected to mechanical and chemical stresses will provide valuable information on the material's durability, and can help predict its wear and degradation over time. This capability has the potential to dramatically improve implant assessment and development and significantly reduce costs related to the replacement of failed prostheses.

Magnetic-guided drug delivery

The use of magnetic nanoparticles in biomedical research was pioneered by Gilchrist in 1956 when he utilized their induced heating for the treatment of lymph nodes near cancer sites [218]. A few years later in 1963, Meyer described how one can exploit magnetic targeting to localize iron oxide nanoparticle-based drug delivery systems for targeted therapeutic applications [219]. Over the years, different drug delivery vehicles have been developed that continue to take advantage of the unique properties of magnetic nanoparticles [220–223].

The design and assembly of magnetic drug delivery structures range from the surface modification of single particles to the adaptation of hollow and hybrid structures decorated with magnetic nanoparticles (Fig. 33). Magnetic nanoparticles can be synthesized with a core–shell structure upon coating with silica [224], gold [225], or a polymer to allow for easy functionalization and loading of drugs [152, 166]. Polymeric micelles structures consisting of hydrophilic outer shells and hydrophobic inner shells can be loaded with magnetic nanoparticles and active drugs inside the microcapsules through simple solvent evaporation methods. The size of the polymeric micelles can be controlled by adjusting the concentration of the amphiphilic block-copolymer used during the synthesis, thus providing flexibility on the loading of drug molecules [166]. In addition, various magnetic polymer nanostructures fabricated with thermoresponsive polymers can facilitate controlled release of drug molecules using magnetic hyperthermia effects [152]. Hollow nanostructures also provide an advantage for drug delivery due to the voids in the structure and its high drug loading capacity. Magnetic hollow nanoparticles can be directly synthesized

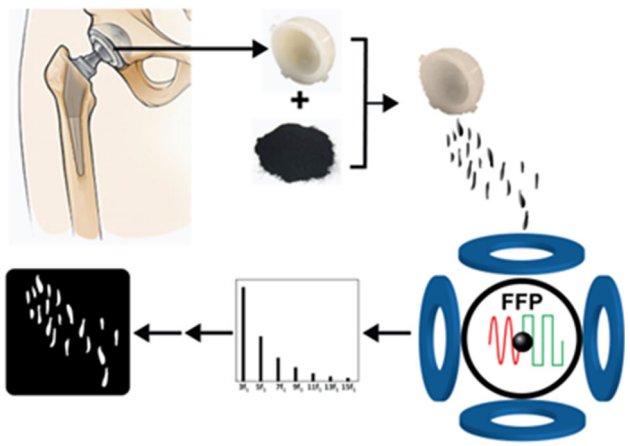

Fig. 32 Schematic representation of the magnetic particle imaging (MPI)-guided research on polymer implant materials

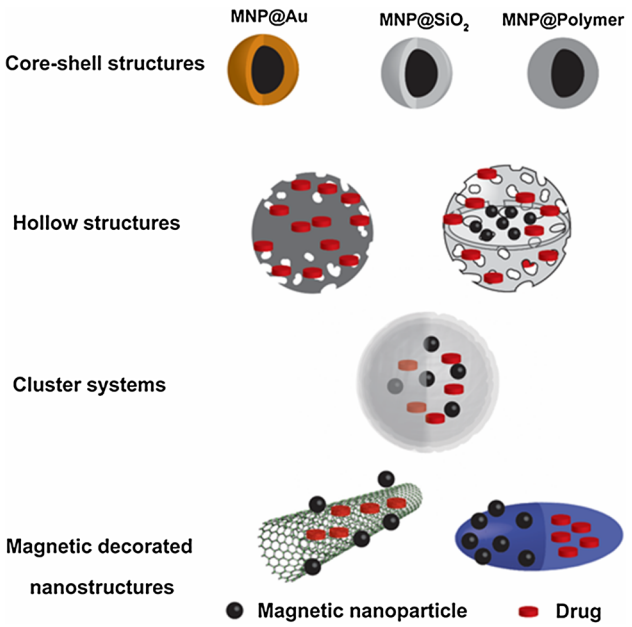

Fig. 33 Different structures of magnetic nanoparticle-based drug delivery systems

through co-precipitation of aqueous metal precursors or a galvanic replacement reaction on pre-synthesized metal oxide nanoparticles [226, 227]. Along this line, porous FePt microstructures were synthesized using cationic poly (diaryldimethylammonium chloride) (PDDA) as a sacrificial template. After loading with doxorubicin (DOX), in vitro treatment with applied alternating magnetic field (AMF) excitation showed above 70 % retardation in gastric cancer and lung cancer cell growth [228].

Magnetic nanoparticles have also been used to decorate other drug delivery vehicles for magnetic guidance. For example, magnetic nanoparticle decorated carbon nanotubes have been shown to be an effective platform for delivering anticancer drugs. Chen et al. have fabricated carbon nanotubes with Fe_3O_4 nanoparticles and the AMF treatment at the therapeutic site increased the drug efficacy up to two times, demonstrating that adding magnetic features in the drug delivery system can improve treatment outcome and reduce dosage of anticancer drugs used during therapy [229, 230]. In addition to the unique structures that allow for high loading of drugs and localized treatments using an external magnetic field, fabricated hybrid magnetic nanostructures are also compatible with most drugs used for targeted therapy. For example, drug molecules like DOX and paclitaxel (PTX) are used in anticancer therapy and are most commonly used in magnetic-guided drug delivery studies [220]. Antibiotics such as tetracycline, penicillin, and ciprofloxacin have also been incorporated into magnetic drug delivery vehicles to deliver antibiotics for localized treatments at infected sites [227, 232]. Radioisotopes have also been delivered using magnetically guided vehicles for anticancer therapy. Magnetic microspheres with the β-emitter ^{90}Y were shown to localize in tumor areas that resulted in complete disappearance of more than half of the tumors treated [221, 233].

Other than the ability to localize drugs at the diseased sites, magnetic nanoparticles have also been employed to design drug delivery vehicles with modulated drug release capacities through controlled excitation with an external magnetic field. Langer's group has demonstrated an increase in drug release in polymer nanocomposites loaded with iron oxide beads under AMF excitation. In their study, they have demonstrated that the movement of the iron oxide beads upon AMF excitation produces "microcracks" in the polymer matrix that then enables the release of the drug molecules entrapped in the nanocomposite. This method has been proven to be effective in the selective release of drug molecules with large molecular weights, which have slow diffusion rates [144, 234]. Implantable magnetic-modulated hemispherical drug delivery devices were also designed to enhance the drug release rate of large drug molecules under magnetic trigger. Applying a similar theory, hollow and porous silica

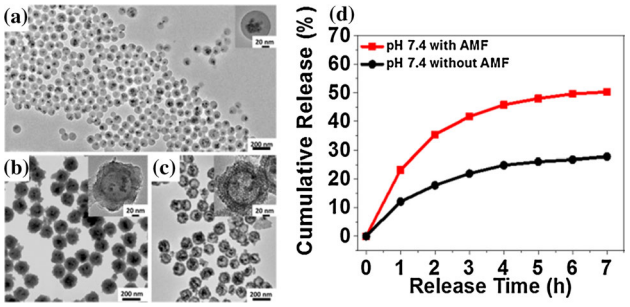

Fig. 34 Iron oxide nanoparticles coated in **a** polystyrene, **b** polystyrene and silica, and **c** iron oxide nanoparticles in hollow silica encapsulations. **d** Release profiles of doxorubicin from nanostructures with and without magnetic triggers. Copyright © Royal Chemical Society 2013 [144]

nanospheres containing clusters of iron oxide nanoparticles and DOX have been fabricated. In the absence of an applied AMF, the DOX can be released through the pores of the silica shell via diffusion. However, the AMF can induce magnetic hyperthermia effects, thus increasing the drug release rate (Fig. 34) [144]. Magnetic-triggered drug release has also been applied in nanostructures composed of flexible magnetic nanochains and drug-filled liposomes. The flexibility in the magnetic nanochains allows oscillation movements in the magnetic nanoparticles under the exposure to a radiofrequency field. Such oscillation movements can be transferred to the liposome filled with DOX and cause it to burst and achieve drug release on-demand [235].

Superparamagnetic iron oxide nanoparticles have also been utilized for dual therapeutic and diagnostic functionalities for theranostic applications. Jain et al. fabricated iron oxide nanoparticles coated with OA and Pluronic F-127 that were subsequently loaded with the cancer drugs DOX and PTX [236]. They reported that the drugs could be loaded efficiently into the magnetic nanoparticles individually or in combination (74–95 %). At the same time, the drug-loaded magnetic nanoparticles showed T_2 relaxivities comparable with that of Feridex IV but lower than that of bare magnetic nanoparticles. MRI-guided drug delivery using pH-responsive magnetic polymer nanocomposites has also been reported. A nanodrug carrier that specifically responds to the lower pH of extracellular cancer cells (pH 6.5–7.2) was fabricated by Lim et al. [237]. In their work, $MnFe_2O_4$ nanoparticles and DOX were encapsulated in a pyrene–polyethylene glycol derivative using a nanoemulsion method. DOX forms strong pi–pi interactions with pyrene under physiological conditions (pH 7.4), but these interactions become weaker when DOX is protonated in acidic conditions like that of intracellular cancer cells (pH 5), which leads to drug release. MRI was used to see the distribution of the drug in the tumor cells.

Magnetic resonance imaging (MRI)

MRI is a powerful, noninvasive tool for imaging tumors and monitoring therapy [238]. Clinically, contrast agents are routinely administrated to enhance image contrast for better resolution [239, 240]. Spherical iron oxide nanoparticles were traditionally utilized as negative (T_2) MRI contrast agents, which generate a darker (T_2-weighted) image by shortening the transverse relaxation time (T_2) [27, 241]. Iron oxide nanoparticles have limited clinical use as negative (T_2) contrast agents, because these nanoparticles can only passively accumulate in the liver or spleen [242, 243]. In addition, signal attenuation after T_2 contrast injection is susceptible to misinterpretation due to other potential sources of signal voids [244, 245]. The currently available positive (T_1) contrast agents are primarily gadolinium (Gd) complexes, which generate a brighter (T_1-weighted) image. Unfortunately, the use of Gd-based contrast agents has raised concerns about nephrogenic systemic fibrosis (NSF) in patients with acute kidney injury, severe renal disease, and liver transplant [246]. Recently, there is a growing interest in generating positive contrast with iron oxide nanoparticles through the alteration of imaging techniques. Several MR techniques for positive contrast imaging with iron oxide nanoparticles have been explored [247], such as susceptibility-weighted imaging [248] and phase gradient imaging [249]. Recently, ultrasmall spherical iron oxide nanoparticles ($\sim$3 nm) were shown to generate positive MRI contrast in mice under standard imaging protocols [28]. Therefore, it is feasible to develop T_1 contrast agents for standard clinical scanners by simply adjusting the properties of the nanoparticles.

The potential of using ultrasmall spherical iron oxide nanoparticles (<5 nm) as T_1 contrast agents has been demonstrated by several research groups [250–253]. The rationale of using ultrasmall iron oxide nanospheres as T_1 contrast agents is that the strong surface effects lead to strong paramagnetic properties. The high surface areas also enhance the water diffusion around the nanoparticles. The strong paramagnetic property and large surface area for water diffusion make ultrasmall nanospheres good candidates for T_1 MRI contrast agents. In addition to generating positive contrast agents, 3 nm ultrasmall spheres also showed high r_1 relaxivity and increased blood circulation time [28]. The in vivo mouse study also suggested that the ultrasmall iron oxide nanospheres enabled high-resolution blood pool T_1-weighted MR images of various blood vessels with size down to 0.2 mm. Figure 35 shows the T_1-weighted MR images of a mouse circulation system. The positive enhancement of the blood vessels remained for 1 h, indicating the long circulation time. Both the positive enhancement and the long blood circulation time are very important for clinical MR imaging.

Ultrasmall spheres are always associated with aggregation issues because of the high surface energy [250]. In addition, small nanoparticles (<8 nm) generally have fast renal clearance and tend to escape from blood circulation [254]. Similar to the rationale of ultrasmall spheres, we recently demonstrated that ultrathin nanowhiskers can be used as effective T_1 contrast agents as well. The extremely small diameter ($\sim$2 nm) of these nanowhiskers led to very high surface-to-volume ratios. The iron oxide nanowhiskers were prepared using our previously published procedure by decomposing the iron (III)-ligand complex at 150 °C with slight modification [16]. Specifically, oleylamine was introduced as a co-ligand during precursor preparation with oleate-to-oleylamine ratio of 2:1 [95]. This modification allowed producing iron oxide nanowhiskers with a more uniform diameter and length. Figure 36 a shows a TEM image of the ultrathin iron oxide nanowhiskers (about 2 × 20 nm) from a typical reaction. The high-resolution TEM image (inset) indicated the crystalline structure and small diameter of these nanostructures. These nanowhiskers showed a very strong paramagnetic signal without saturation from the magnetization versus applied field (M–H) curve of (Fig. 36). The strong paramagnetic signal is due to the high surface-to-volume ratio and surface iron–ligand complexation. A high percentage of surface iron atoms interacted with the capping molecules through coordination bonds, forming a layer of iron–ligand complexes. The surface layer is mainly paramagnetic, the so-called magnetic "dead layer" on the nanoparticle surfaces, which is commonly observed in small magnetic nanoparticle systems [108–112].

The as-synthesized nanowhiskers are only soluble in organic solvent and they must be transferred into aqueous solution for any biological or biomedical applications. The oleate- and oleylamine-coated iron oxide nanowhiskers were transferred into aqueous solution using tween-80 as capping molecules through a second layer encapsulation approach [255]. Specifically, polysorbate 80 (tween 80), an amphiphilic biocompatible polymer in water was mixed with nanowhisker organic solution under sonication. The hydrophobic region of tween-80 interacts with the hydrophobic tail of the ligand molecules on the nanowhisker surfaces, leaving the ethylene oxide polymers exposed for water solubility and biocompatibility.

The T_1-weighted MR images of a Sprague–Dawley rat collected on a 3T clinical MRI scanner also showed strong enhancement for both subcutaneous and intraperitoneal injection. Figure 37a–c shows T_1-weighted MR images of a Sprague–Dawley rat collected on a 3T clinical MRI scanner (Philips Achieva). The nanowhiskers were administrated intraperitoneally and subcutaneously. T_1-weighted MR images of the animals were recorded pre-injection and 1-min post-injection. The abdominal region of the IP

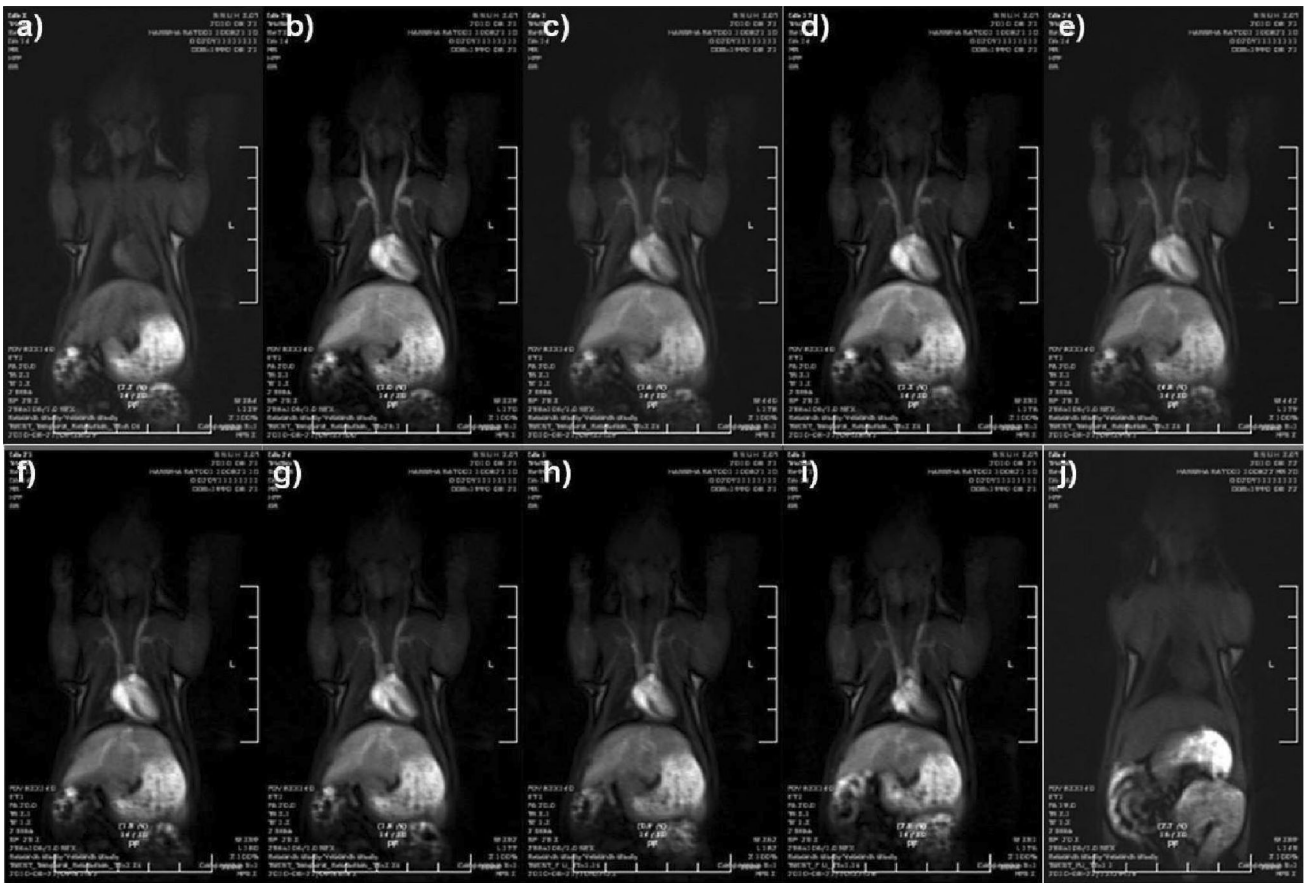

Fig. 35 ESION-enhanced in vivo MR images with dynamic time-resolved MR sequence acquired at **a** 0 s and **b** 30 s, **c** 1 min, **d** 2 min, **e** 3 min, **f** 5 min, **g** 10 min, **h** 30 min, **i** 60 min, and **j** 1 day after the injection. Copyright © American Chemical Society 2011 [28]

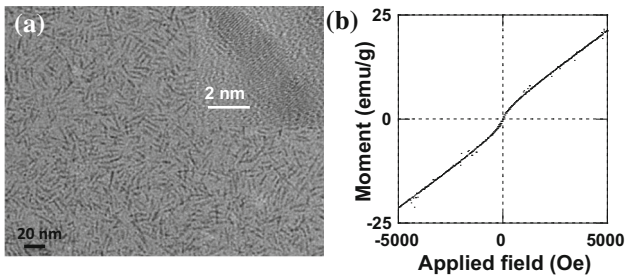

Fig. 36 Ultrathin iron oxide nanowhiskers: **a** a TEM image, and **b** a *M–H* curve. Copyright © Royal Chemical Society 2015 [2]

injected animal (Fig. 37b) shows brightening compared with the pre-injection image in Fig. 37a, suggesting the strong positive contrast enhancement of iron oxide nanowhiskers. The bleb from the subcutaneous injection (red circle) clearly shows T_1 enhancement due to the contrast agent (Fig. 37c). Both of these studies indicated the feasibility to generate positive contrast enhancement in vivo using ultrathin iron oxide nanowhiskers under standard MRI settings. The successful development of iron oxide nanoparticle-based T_1 contrast agents will not only fulfill the need of patients with special conditions during an MRI scan, but also greatly benefit healthy patients who need MRI scans, potentially leading to the advancement of human health.

Pharmacokinetic pathways of iron oxide nanoparticles

Superparamagnetic iron oxide nanoparticles (SPIONs) are the only class of magnetic nanoparticle materials with a history of clinical use. First introduced in the early nineties, clinically approved SPIONs were used as MRI contrast agents providing negative (T_2/T_2*) contrast enhancement, but their use as such has declined since market-wide discontinuation of SPION agents. Currently, Feraheme® (ferumoxytol)—clinically approved for treating iron deficiency in anemia patients [256]—is the only nonstoichiometric magnetite SPION formulation actively produced and marketed. However, novel technologies such as MPI [33, 205, 257, 258] and emerging applications such as magnetic SLNB [259, 260] are reviving clinical interest in SPION agents. Unlike the MRI contrast predecessors, however, a new class of SPIONs with precisely tailored

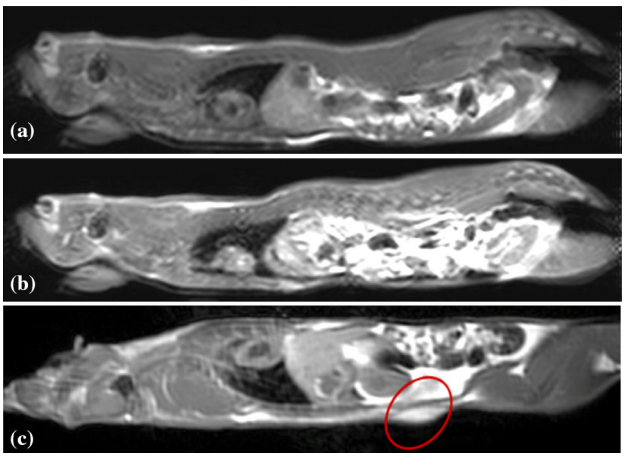

Fig. 37 T_1-weighted in vivo images of nanowhisker contrast agent at 3T: **a** Pre-injection image without nanowhiskers, **b** post-injection image showing positive enhancement of the abdominal region. 6 ml of contrast agent was injected IP, and **c** subcutaneous injection of 1 ml of nanowhiskers at 2 mg/ml concentration. *Red circle* indicates the bleb at the site of injection. Copyright © Royal Chemical Society 2015 [29] (Color figure online)

physicochemical properties are necessary. Further, the physicochemical and magnetic properties of SPIONs must be preserved in the physiological environment to ensure consistent performance after in vivo administration. Thus, SPION pharmacokinetics (PK) must be well characterized and controlled for translational application of these emerging technologies. In this section, we review the physicochemical properties of SPIONs that affect their principle pharmacokinetic properties—absorption, distribution, metabolism and excretion, typically referred together as "ADME" properties, and are defined as follows:

Absorption—traditionally defined for orally administered drugs, absorption involves two important steps: (1) absorption of the inactive drug through physiological barriers (e.g., GI tract for oral administration), and (2) release or bioavailability of the active drug into systemic circulation. For intravenously administered SPIONs, absorption is bypassed and bioavailability is considered 100 % as the drug directly enters systemic circulation. A critical parameter of bioavailability is the blood half-life, which is the time it takes to reach 50 % of the initial concentration in blood.

Distribution is defined as the reversible accumulation of the circulating drug in various organs or tissues, and depends on factors such as vascular permeability, organ perfusion, plasma protein binding, and macrophage uptake. Drugs or SPIONs that avoid protein binding and macrophage uptake in organs may re-enter systemic circulation.

Metabolism involves the irreversible breakdown of the drug into smaller metabolites. SPIONs are typically metabolized in organs comprising the mononuclear phagocytic system (MPS).

Excretion is the removal of the drug and its metabolites. As will be discussed in a later section, the body's conservative iron cycle limits active excretion of SPIONs. Iron oxide is instead recycled and transformed into various storable or usable forms.

Influence of physiological barriers on SPION pharmacokinetics

The selection of an in vivo administration route plays a critical role in dictating SPION PK. Critically, the body's "first line of defense" or physiological barriers that govern PK for an intravenous (IV) injection are different from a subcutaneous or oral administration. Traditionally, IV injection has been the preferred administration route for SPIONs as it provides rapid bioavailability of the iron oxide cores in the active superparamagnetic state. Thus, we first review the physiological barriers that SPIONs encounter following IV injection, followed by other routes such as subcutaneous and oral administration.

The vasculature network constructed from endothelial cells is the primary route for material exchange between blood and tissues. The structure of blood vessels, especially finer capillaries that penetrate deep in organs, is variable and tailored to facilitate the specific functions of organs they supply. For instance, the blood–brain barrier (BBB) [261] is a highly selective vascular network in the brain that allows for exchange of only essential micronutrients, although occasionally larger molecules and nanoparticles can permeate through a receptor-mediated transcytosis pathway [262]. On the other hand, organs responsible for filtering and detoxifying blood consist of fenestrated capillaries to allow for extraction of macromolecules and nanoparticles. Figure 38 provides a general illustration of blood vessel morphology in some vital organs that partake in the clearance of drugs and nanoparticles.

The bioavailability of IV injected SPIONs depends on their ability to remain systemic and curtail irreversible removal from fenestrated capillaries in the kidneys, liver, spleen, and bone marrow. In kidneys, certain globular proteins (less than 20,000 Da) and water-soluble drug molecules [263] are filtered out from blood in the glomeruli capillary folds (Fig. 38a). The filtrate enters the encapsulating Bowman capsule and eventually gets excreted with urine. However, unlike in the sinusoid capillaries of the liver and spleen, a basement membrane provides structural integrity to the glomeruli capillaries and limits fenestrae size from about 5 nm to no greater than 15 nm [264, 265]. Most SPIONs larger than 15 nm in hydrodynamic diameter avoid renal filtration and instead distribute in organs that host the mononuclear phagocyte system (MPS)—a system of phagocytic cells that reside in the sinusoid capillaries of the liver, spleen and lymph nodes, and as macrophage

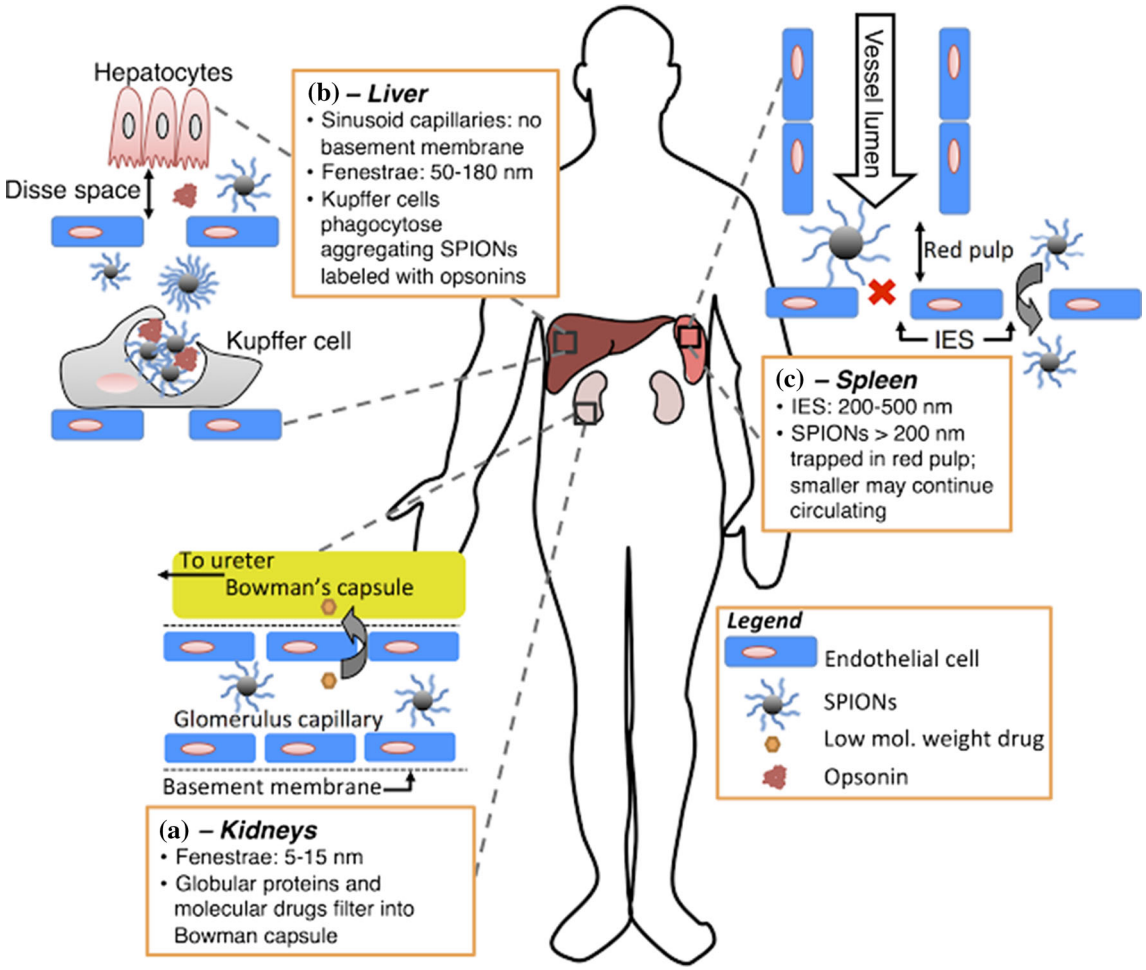

Fig. 38 Illustration of key physiological barriers SPIONs encounter during systemic circulation (relative dimensions not drawn to scale). **a** Kidneys extract small water-soluble molecules from circulation, but nanoparticles greater than ~15 nm avoid getting filtered. **b** Large fenestrae (50–180 nm) in sinusoid capillaries of the liver allow SPIONs to permeate in and out of lumen, prolonging their residence time; as a result, opsonins can adsorb onto aggregating nanoparticles and activate phagocytosis in Kupffer cells—the resident macrophages of the liver. SPIONs coated with nonfouling "stealth" polymers (minimize opsonin adsorption) like PEG delay phagocytosis removal and thus have longer circulation times. **c** The Spleen imposes an upper limit on size for circulating SPIONs, as anything rigid and larger than about 200 nm in diameter may get trapped in the *red pulp* and is eventually sequestered by resident phagocytic cells

progenitors in the bone marrow [266]. Sinusoid capillaries are highly fenestrated vessels that lack a continuous basement membrane, allowing for greater vascular permeability and blood perfusion in the host organ, and thus increasing the probability for phagocytosis and removal by resident MPS cells. In the sinusoid capillaries of the liver (Fig. 38b), fenestrae can range from 50 to 180 nm and allow for macromolecular exchange between the sinusoid lumen and hepatocytes through the plasma-rich perisinusoidal space (or Disse space) [267, 268]. The phagocytic MPS cells of the liver, also called Kupffer cells, reside in the sinusoid capillaries. Phagocytic removal of SPIONs and other nanoparticles occurs when plasma proteins called opsonins adsorb onto the particle surface and enable recognition by Kupffer cells and other phagocytic cells comprising the MPS; thus, avoiding or minimizing opsonin binding should be a critical requirement for designing long-circulating SPIONs.

In the spleen (Fig. 38c), sinusoid capillaries are morphologically distinct from that of the liver [71]. Blood from terminal arterial openings flows into the red pulp—a region engorged with dead erythrocytes and platelets (thus the red appearance)—where it undergoes filtration by seeping through the 200–500 nm-wide interendothelial slits (IES) [265, 269] before re-entering systemic circulation. The deformability of healthy erythrocytes allows them to pass through the relatively smaller IES, while rigid structures such as dead erythrocytes or nanoparticles greater than 200 nm in diameter get trapped in the red pulp. Macrophages residing in the spleen eventually phagocytose material accumulated against the IES [269]. SPIONs can also passively accumulate in certain fast-growing tumors;

tumor vasculature is highly permeable and suffers from poor lymphatic drainage, which results in a phenomenon called the enhanced permeability and retention (EPR) effect. Passive accumulation of SPIONs and other macromolecules using the EPR effect has been proposed as a "silver bullet" approach to targeting a wide spectrum of cancers; however, translation from well-controlled preclinical to realistic clinical models has been slow possibly due to heterogeneity in tumors and the surrounding vascular morphology [270].

SPION administration through routes other than IV injection are less common for their wide clinical use as imaging agents but prevalent for other budding applications. For instance, subcutaneous or peritumoral injection is more appropriate than IV injection for Sentinel Lymph Node detection and Biopsy (SLNB)—an emerging area of clinical application for magnetic SPIONs [260, 271–273]. In a typical magnetic SLNB procedure [259], SPIONs are injected subcutaneously near the tumor, from where a portion of the injected material traverses through the draining lymphatic vessels and localizes in the sentinel lymph nodes. Lymph nodes consist a large number of phagocytic lymphocytes and macrophages that uptake SPIONs and cease further advancement. However, SPIONs with nonfouling coatings that minimize phagocytic uptake can continue draining to higher echelon nodes or even enter a nearby blood vessel, where they eventually disseminate through one of the systemic pathways discussed above. Finally, oral administration is less common but also a possible administration route for SPIONs. GastroMARK® (ferumoxsil, Mallinckordt Inc.) was an aqueous dispersion of silicone-coated SPIONs intended for oral administration and MR-imaging of the gastrointestinal (GI) tract. Since the intended use of GastroMARK was primarily diagnostic imaging of the bowels, the surface coating was designed to minimize absorption in the GI tract and excrete the material out with feces. The fraction of SPIONs that do get absorbed through the GI tract enter systemic circulation, but the SPION may break down during the absorption process and its bioavailability in the superparamagnetic state will be limited—a major reason why IV administration of SPIONs is preferred for delivery to organs outside the GI tract. On the other hand, it should be possible to design "prodrug" formulations that protect the active SPION composition during GI absorption.

Influence of surface properties on SPION pharmacokinetics

The preceding discussion presents a general summary of physiological barriers SPIONs encounter through various administration routes. In the following section, we consider the influence of surface physicochemical properties on the pharmacokinetic characteristics of SPIONs. Note that the scope of this discussion is limited to low aspect ratio particles, which are representative of nanoparticles typically synthesized and thus extensively studied and used in clinical applications. SPIONs intended for in vivo use typically consist of an external shell coating to help stabilize and protect the magnetic cores in physiological environments. While inorganic shells are common, organic coatings such as dextran-based carbohydrates and hydrophilic polymers like polyethylene glycol (PEG) are preferred because of their relative biocompatibility and functionalization versatility. The physicochemical makeup of coatings contributes significantly to the hydrodynamic diameter (d_H), net surface charge, and coating coverage—all being the critical design parameters that determine the in vivo fate of nanoparticles.

Size Hydrodynamic diameter (d_h) of a SPION, also called the Stokes diameter, is its diameter when dispersed in a solvent and includes the nanoparticle core, shell, and any associated solvent layer that diffuses as an extension of the coating. In view of the different physiological barriers discussed above, d_h is an important parameter that affects SPION permeability through capillary fenestrae. Renal filtration is particularly dominant when d_h is smaller than the 5–15 nm kidney fenestrae. Long-circulating SPIONs must preferably have d_h greater than 15 nm to avoid rapid renal clearance. At the other extreme, SPIONs larger than the average spacing between interendothelial slits in the spleen (200–500 nm) will be retained and eventually get cleared by macrophages in the red pulp. Strictly going by the lower and upper size limits enforced by physiological barriers in the kidney and spleen, SPIONs with d_h between 15 and 200 nm should have reasonable blood retention or blood half-life times. In practice, however, PK studies with dextran and PEG-coated SPIONs showed that circulation time (blood half-life) decreases with the increase in d_h (assuming size within the 15–200-nm window) [70, 274, 275]. The latter finding is in line with cellular uptake studies that show greater phagocytic uptake in monocytes [276] and other cancer cell lines [277] when d_h is increased, suggesting larger nanoparticles are more susceptible to opsonin binding, aggregation, and subsequent macrophage-mediated clearance in MPS organs like the liver and spleen [278–280]. Thus, reducing opsonin binding is critical to designing long-circulation SPIONs.

Charge In addition to size, surface charge is a critical surface property that dictates opsonin binding. Unlike size, shape, and curvature that only affect the number of bound proteins, surface charge plays a significant role in their identity; positively charged nanoparticles preferentially adsorb negatively charge proteins and vice versa [281]. A survey of the literature shows that nanoparticles with neutral or zwitterionic surfaces have lower opsonization rates than charged particles, and thus retained longer in

circulation [279, 281–283]. Metz et al. [276] showed that a carboxydextran (negatively charged)-coated SPION formulation called SHU 555C ($d_h \sim 21$ nm) showed greater uptake in monocytes than the comparable sized nonionic-dextran-coated ferumoxtran-10 ($d_h \sim 20$–50 nm). Further, the study suggested that surface charge induced a greater phagocytic effect than size as carboxydextran-coated ferucarbotran ($d_h = 62$ nm) showed threefold uptake in monocytes than the significantly larger ($d_h = 150$ nm) nonionic-dextran-coated ferumoxides. On the other hand, surface charge may be useful if efficient cell penetration is a desired application, which is the case in nonviral delivery of DNA or siRNA to cells using charged polymers [6, 284]. Positively charged polymer coatings such as poly(-ethyleneimine) (PEI) enhance cell penetration due to electrostatic attraction to the negatively charged phospholipid-lined cell membranes.

Coating density Hydrophobic surfaces, due to their insolubility in aqueous environments, often undergo rapid nonspecific protein adsorption and must be cloaked when designing long-circulating SPIONs. PEG is particularly attractive for coating hydrophobic SPION cores due to its exceptional nonfouling characteristics [285, 286]. Nevertheless, even partially hydrophobic regions, which may not affect solubility in aqueous media, can agglomerate SPIONs in biological media due to opsonin binding in a physiological environment. Thus, the density or surface coverage of coatings is another critical parameter in designing long-circulating SPIONs. For PEG-coated nanoparticles, low or high surface coverage results in either a 'mushroom' or 'brush' configuration, respectively [280]. In the mushroom state, PEG chains have greater mobility due to increased distance between neighboring polymers. The low coverage however, exposes significant portions of the underlying core, providing easy access for opsonin binding. At the other extreme, high surface coverage extends PEG chains further into the solvent, but, in addition reduces chain flexibility and mobility—critical properties of PEG responsible for its nonfouling characteristics [286]. Thus, optimal PEG conformation must facilitate both sufficient coverage and PEG chain mobility to prevent access to opsonins and enhance nanoparticle stability.

SPION metabolism and the iron cycle

The systemic bioavailability of SPIONs eventually decreases as their distribution in the MPS organs—liver, spleen, and lymph nodes—becomes irreversible due to opsonin binding and phagocytic uptake. This starts the metabolism process, which is the next step in the pharmacokinetic cycle of SPIONs. Since iron is an essential component of the body's hematopoietic cycle, it is incorporated in the physiological iron cycle and either utilized or conserved for future use [287, 288]. An illustration of the iron cycle is provided in Fig. 39. SPIONs phagocytosed in MPS cells are digested in the acidic lysosomes and sequestered in ferritin and hemosiderin protein cages. About 1.5 grams of the body's total iron, primarily distributed in the liver parenchyma and other MPS cells, is stored in this manner [289]. The iron is stored in a nontoxic mineral form consisting a mixture of magnetite, hematite, and ferrihydrite phases [296]. In addition to storage, ferritin and hemosiderin also serve to supply iron for hemoglobin production during erythropoiesis (red blood cell production) in the bone marrow. Hemoglobin in erythrocytes uses up about 2 g of iron, which is about 2/3 of the total iron in the body. Myoglobin proteins in muscles account for another 10 %; together, hemoglobin and myoglobin represent the lion's share of iron utilized for physiological function. Finally, the amount of iron loss is about the same as the amount of iron absorbed from dietary intake—about 1–2 mg per day. In summary, the iron cycle is highly conserved and SPIONs metabolized in the liver and other MPS organs are eventually incorporated in either the storage or utilization pathways.

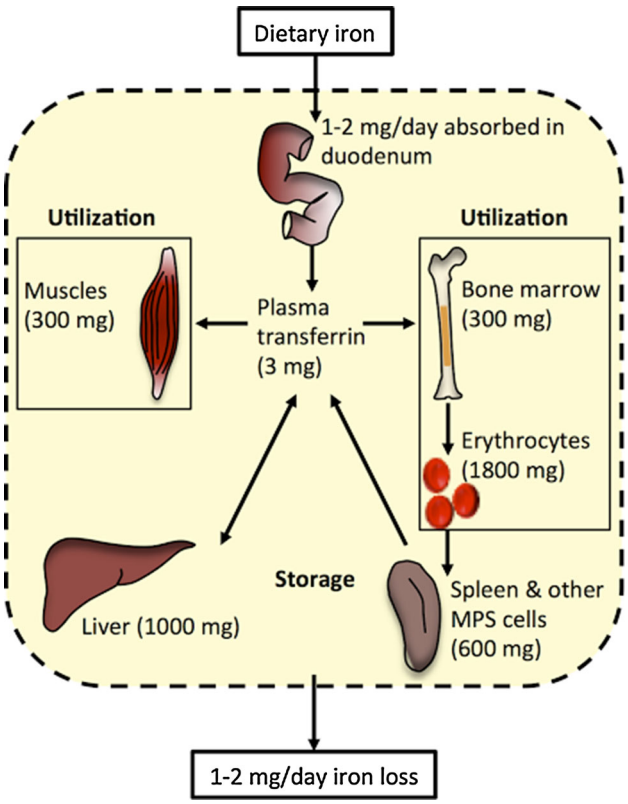

Fig. 39 SPIONs administered in vivo distribute in the liver, spleen, and lymph nodes. MPS cells digest the nanoparticles and store the iron in ferritin and hemosiderin proteins. Since iron is highly conserved in the body, the SPIONs are eventually recycled and incorporated to some degree of storage and utilization in the physiological iron cycle. Figure adapted from Ref. [289]

Perspectives and outlook

It is clear from this comprehensive review of our work that research in magnetic nanoparticles, particularly phase-pure magnetite, with tailored sizes, narrow size distributions and optimized surface functionalities, has reached a sophisticated level of optimization. In fact, we are at the cusp of realizing major translational applications in biomedical imaging, diagnostics and therapy. Much of this progress is due to careful material engineering at the nanoscale, both of the nanoparticle core properties, to tailor their magnetic response, and its surface functionalization for molecular imaging (targeting), biocompatibility, and controlled circulation. Further progress will occur only if careful attention is paid to in vivo biological constraints, including addressing challenges of ensuring continued optimal magnetic response in the "harsh" in vivo environment, minimizing toxicity, achieving appropriate circulation times and controlling their biodistribution and clearance. In parallel, as we have described, the monodispersity of such nanoparticles lends them to large-area self-assembly with unique possibilities in creating lithographic structures at the $\sim$10-nm length scale and potentially impacting broadly on energy and information technologies.

Acknowledgements Y. Bao was partially supported by NSF-DMR 0907204, DMR 114993, and Ralph Power Junior Faculty Enhancement Award. T. Wen acknowledges the financial support from the National Natural Science Foundation of China under contract # 51401046 and # 61131005. A. C. S. Samia is supported by an NSF-CAREER Grant (DMR-1253358). A. Khandhar and Kannan M. Krishnan acknowledge support from the NIH/NIBIB grant nos. 1R41EB013520-01 and 2R42EB013520-02A1. Kannan M. Krishnan was also supported under grant nos. NIH 1R01EB013689-01/NIBIB, NSF/DMR–0501421, and NSF/DMR #0203069.

References

1. Casbeer E, Sharma VK, Li XZ (2012) Synthesis and photocatalytic activity of ferrites under visible light: a review. Sep Purif Technol 87:1–14
2. Mangrulkar PA, Polshettiwar V, Labhsetwar NK, Varma RS, Rayalu SS (2012) Nano-ferrites for water splitting: unprecedented high photocatalytic hydrogen production under visible light. Nanoscale 4:5202–5209
3. Han SB, Kang TB, Joo OS, Jung KD (2007) Water splitting for hydrogen production with ferrites. Sol Energy 81:623–628
4. Pankhurst QA, Connolly J, Jones SK, Dobson J (2003) Applications of magnetic nanoparticles in biomedicine. J Phys D 36:R167–R181
5. Krishnan KM (2010) Biomedical nanomagnetics: a spin through possibilities in imaging, diagnostics, and therapy. IEEE Trans Magn 46:2523–2558
6. Plank C, Vlaskou D, Schillinger U, Mykhaylyk O (2011) MagnetofectionTM platform: from magnetic nanoparticles to novel nucleic acid therapeutics. Ther Deliv 2:717–726
7. Massoud TF, Gambhir SS (2003) Molecular imaging in living subjects: seeing fundamental biological processes in a new light. Genes Dev 17:545–580
8. Jain RK (1998) The next frontier of molecular medicine: delivery of therapeutics. Nat Med 4:655–657
9. Ito A, Shinkai M, Honda H, Kobayashi T (2005) Review: medical application of functionalized magnetic nanoparticles. J Biosci Bioeng 100:1–11
10. Liang QL, Macher T, Xu YL, Bao YP, Cassady CJ (2014) MALDI MS in-source decay of glycans using a glutathione-capped iron oxide nanoparticle matrix. Anal Chem 86:8496–8503
11. Baldi G, Bonacchi D, Innocenti C, Lorenzi G, Sangregorio C (2007) Cobalt ferrite nanoparticles: the control of the particle size and surface state and their effects on magnetic properties. J Magn Magn Mater 311:10–16
12. Vestal CR, Zhang ZJ (2003) Effects of surface coordination chemistry on the magnetic properties of $MnFe_2O_4$ spinel ferrite nanoparticles. J Am Chem Soc 125:9828–9833
13. Song O, Zhang ZJ (2004) Shape control and associated magnetic properties of spinel cobalt ferrite nanocrystals. J Am Chem Soc 126:6164–6168
14. Palchoudhury S, Xu Y, Goodwin J, Bao Y (2011) Synthesis of iron oxide nanoworms. J Appl Phys 109:07E314
15. Palchoudhury S, Xu YL, Rushdi A, Holler RA, Bao YP (2012) Controlled synthesis of iron oxide nanoplates and nanoflowers. Chem Commun 48:10499–10501
16. Palchoudhury S, An W, Xu YL, Qin Y, Zhang ZT, Chopra N et al (2011) Synthesis and growth mechanism of iron oxide nanowhiskers. Nano Lett 11:1141–1146
17. Peddis D, Cannas C, Musinu A, Piccaluga G (2009) Magnetism in nanoparticles: beyond the effect of particle size. Chem-A Eur J 15:7822–7829
18. Peddis D, Cannas C, Musinu A, Ardu A, Orru F, Fiorani D et al (2013) Beyond the effect of particle size: influence of $CoFe_2O_4$ nanoparticle arrangements on magnetic properties. Chem Mater 25:2005–2013
19. Lee J-H, Jang J-T, Choi J-S, Moon SH, Noh S-H, Kim J-W et al (2011) Exchange-coupled magnetic nanoparticles for efficient heat induction. Nat Nano 6:418–422
20. Mohapatra J, Mitra A, Bahadur D, Aslam M (2013) Surface controlled synthesis of MFe_2O_4 (M = Mn, Fe Co, Ni and Zn) nanoparticles and their magnetic characteristics. CrystEngComm 15:524–532
21. Li QL, Wang YF, Chang CB (2010) Study of Cu Co, Mn and La doped NiZn ferrite nanorods synthesized by the coprecipitation method. J Alloy Compd 505:523–526
22. Xu Y, Sherwood J, Qin Y, Holler RA, Bao Y (2015) A general approach to the synthesis and detailed characterization of magnetic ferrite nanocubes. Nanoscale 7:12641–12649
23. Scherer C, Neto AMF (2005) Ferrofluids: properties and applications. Braz J Phys 35:718–727
24. Xie J, Huang J, Li X, Sun S, Chen X (2009) Iron oxide nanoparticle platform for biomedical applications. Curr Med Chem 16:1278–1294
25. Namdeo M, Saxena S, Tankhiwale R, Bajpai M, Mohan YM, Bajpai SK (2008) Magnetic nanoparticles for drug delivery applications. J Nanosci Nanotechnol 8:3247–3271
26. Gazeau F, Levy M, Wilhelm C (2008) Optimizing magnetic nanoparticle design for nanothermotherapy. Nanomedicine 3:831–844
27. Reimer P, Balzer T (2003) Ferucarbotran (Resovist): a new clinically approved RES-specific contrast agent for contrast-enhanced MRI of the liver: properties, clinical development, and applications. Eur Radiol 13:1266–1276

28. Park M, Lee N, Choi SH, An K, Yu SH, Kim JH et al (2011) Large-scale synthesis of ultrathin manganese oxide nanoplates and their applications to T_1 MRI contrast agents. Chem Mater 23:3318–3324
29. Macher T, Totenhagen J, Sherwood J, Qin Y, Gurler D, Bolding MS et al (2015) Ultrathin iron oxide nanowhiskers as positive contrast agents for magnetic resonance imaging. Adv Funct Mater 25:490–494
30. Park JH, von Maltzahn G, Zhang LL, Schwartz MP, Ruoslahti E, Bhatia SN et al (2008) Magnetic iron oxide nanoworms for tumor targeting and imaging. Adv Mater 20:1630–1635
31. Lee N, Choi Y, Lee Y, Park M, Moon WK, Choi SH et al (2012) Water-dispersible ferrimagnetic iron oxide nanocubes with extremely high r_2 relaxivity for highly sensitive in vivo MRI of tumors. Nano Lett 12:3127–3131
32. Guardia P, Di Corato R, Lartigue L, Wilhelm C, Espinosa A, Garcia-Hernandez M et al (2012) Water-soluble iron oxide nanocubes with high values of specific absorption rate for cancer cell hyperthermia treatment. ACS Nano 6:3080–3091
33. Ferguson RM, Khandhar AP, Kemp SJ, Arami H, Saritas EU, Croft LR et al (2015) Magnetic particle imaging with tailored iron oxide nanoparticle tracers. IEEE Trans Med Imaging 34:1077–1084
34. Majetich SA, Sachan M (2006) Magnetostatic interactions in magnetic nanoparticle assemblies: energy, time and length scales. J Phys D 39:R407–R422
35. Majetich SA, Wen T, Mefford OT (2013) Magnetic nanoparticles. MRS Bull 38:899–903
36. Talapin DV, Murray CB (2005) PbSe nanocrystal solids for n- and p-channel thin film field-effect transistors. Science 310:86–89
37. Kim TH, Cho KS, Lee EK, Lee SJ, Chae J, Kim JW et al (2011) Full-colour quantum dot displays fabricated by transfer printing. Nat Photonics 5:176–182
38. Han ST, Zhou Y, Xu ZX, Huang LB, Yang XB, Roy VAL (2012) Microcontact printing of ultrahigh density gold nanoparticle monolayer for flexible flash memories. Adv Mater 24:3556–3561
39. Nie ZH, Petukhova A, Kumacheva E (2010) Properties and emerging applications of self-assembled structures made from inorganic nanoparticles. Nat Nanotechnol 5:15–25
40. Zhang W, Wen TL, Krishnan KM (2012) Positive exchange bias and upward magnetic relaxation in a Fe-film/CoO-nanoparticle hybrid system. Appl Phys Lett 101:132401 **(6 pp)**
41. Majetich SA, Wen T, Booth RA (2011) Functional magnetic nanoparticle assemblies: formation, collective behavior, and future directions. ACS Nano 5:6081–6084
42. Bao YP, Beerman M, Krishnan KM (2004) Controlled self-assembly of colloidal cobalt nanocrystals mediated by magnetic interactions. J Magn Magn Mater 272:E1367–E1368
43. Grzelczak M, Vermant J, Furst EM, Liz-Marzan LM (2010) Directed self-assembly of nanoparticles. ACS Nano 4:3591–3605
44. Bigioni TP, Lin XM, Nguyen TT, Corwin EI, Witten TA, Jaeger HM (2006) Kinetically driven self assembly of highly ordered nanoparticle monolayers. Nat Mater 5:265–270
45. Huang JX, Kim F, Tao AR, Connor S, Yang PD (2005) Spontaneous formation of nanoparticle stripe patterns through dewetting. Nat Mater 4:896–900
46. Whitesides GM, Grzybowski B (2002) Self-assembly at all scales. Science 295:2418–2421
47. Talapin DV, Shevchenko EV, Murray CB, Titov AV, Kral P (2007) Dipole-dipole interactions in nanoparticle superlattices. Nano Lett 7:1213–1219
48. Liddle JA, Cui Y, Alivisatos P (2004) Lithographically directed self-assembly of nanostructures. J Vac Sci Technol B 22:3409–3414
49. Lin XM, Jaeger HM, Sorensen CM, Klabunde KJ (2001) Formation of long-range-ordered nanocrystal superlattices on silicon nitride substrates. J Phys Chem B 105:3353–3357
50. Yin YD, Lu Y, Gates B, Xia YN (2001) Template-assisted self-assembly: a practical route to complex aggregates of monodispersed colloids with well-defined sizes, shapes, and structures. J Am Chem Soc 123:8718–8729
51. Bishop KJM, Wilmer CE, Soh S, Grzybowski BA (2009) Nanoscale forces and their uses in self-assembly. Small 5:1600–1630
52. Cheng GJ, Romero D, Fraser GT, Walker ARH (2005) Magnetic-field-induced assemblies of cobalt nanoparticles. Langmuir 21:12055–12059
53. Shevchenko EV, Talapin DV, Kotov NA, O'Brien S, Murray CB (2006) Structural diversity in binary nanoparticle superlattices. Nature 439:55–59
54. Gao YH, Bao YP, Beerman M, Yasuhara A, Shindo D, Krishnan KM (2004) Superstructures of self-assembled cobalt nanocrystals. Appl Phys Lett 84:3361–3363
55. Wen TL, Majetich SA (2011) Ultra-large-area self-assembled mono layers of nanoparticles. ACS Nano 5:8868–8876
56. Wen T, Zhang D, Wen Q, Zhang H, Liao Y, Li Q et al (2015) Magnetic nanoparticle assembly arrays prepared by hierarchical self-assembly on a patterned surface. Nanoscale 7:4906–4911
57. Wen TL, Brush LN, Krishnan KM (2014) A generalized diffusion model for growth of nanoparticles synthesized by colloidal methods. J Colloid Interface Sci 419:79–85
58. Puntes VF, Krishnan KM, Alivisatos AP (2001) Colloidal nanocrystal shape and size control: the case of cobalt. Science 291:2115–2117
59. Bao YP, An W, Turner CH, Krishnan KM (2010) The critical role of surfactants in the growth of cobalt nanoparticles. Langmuir 26:478–483
60. Lee D-E, Koo H, Sun I-C, Ryu JH, Kim K, Kwon IC (2012) Multifunctional nanoparticles for multimodal imaging and theragnosis. Chem Soc Rev 41:2656–2672
61. Jin YD, Jia CX, Huang SW, O'Donnell M, Gao XH (2010) Multifunctional nanoparticles as coupled contrast agents. Nat Commun 1:1–8
62. Bao YP, Calderon H, Krishnan KM (2007) Synthesis and characterization of magnetic-optical Co-Au core-shell nanoparticles. J Phys Chem C 111:1941–1944
63. Corr SA, Rakovich YP, Gun'ko YK (2008) Multifunctional magnetic-fluorescent nanocomposites for biomedical applications. Nanoscale Res Lett 3:87–104
64. Xu YL, Palchoudhury S, Qin Y, Macher T, Bao YP (2012) Make conjugation simple: a facile approach to integrated nanostructures. Langmuir 28:8767–8772
65. Arami H, Khandhar AP, Tomitaka A, Yu E, Goodwill PW, Conolly SM et al (2015) In vivo multimodal magnetic particle imaging (MPI) with tailored magneto/optical contrast agents. Biomaterials 52:251–261
66. Arami H, Krishnan KM (2014) Intracellular performance of tailored nanoparticle tracers in magnetic particle imaging. J Appl Phys 115:17B306 **(3 pp)**
67. Gonzales-Weimuller M, Zeisberger M, Krishnan KM (2009) Size-dependant heating rates of iron oxide nanoparticles for magnetic fluid hyperthermia. J Magn Magn Mater 321:1947–1950
68. Gonzales M, Krishnan KM (2005) Synthesis of magnetoliposomes with monodisperse iron oxide nanocrystal cores for hyperthermia. J Magn Magn Mater 293:265–270
69. Clift MJD, Rothen-Rutishauser B, Brown DM, Duffin R, Donaldson K, Proudfoot L et al (2008) The impact of different nanoparticle surface chemistry and size on uptake and toxicity in a murine macrophage cell line. Toxicol Appl Pharmacol 232:418–427

70. Chouly C, Pouliquen D, Lucet I, Jeune JJ, Jallet P (1996) Development of superparamagnetic nanoparticles for MRI: effect of particle size, charge and surface nature on biodistribution. J Microencapsul 13:245–255
71. Moghimi SM, Hunter AC, Murray JC (2001) Long-circulating and target-specific nanoparticles: theory to practice. Pharmacol Rev 53:283–318
72. Lunov O, Syrovets T, Rocker C, Tron K, Nienhaus GU, Rasche V et al (2010) Lysosomal degradation of the carboxydextran shell of coated superparamagnetic iron oxide nanoparticles and the fate of professional phagocytes. Biomaterials 31:9015–9022
73. Ferguson RM, Khandhar AP, Arami H, Hua L, Hovorka O, Krishnan KM (2013) Tailoring the magnetic and pharmacokinetic properties of iron oxide magnetic particle imaging tracers. Biomed Eng 58:493–507
74. Kittel C (1949) Physical theory of ferromagnetic domains. Rev Modern Phys 21:541–589
75. Krishnan KM, Pakhomov AB, Bao Y, Blomqvist P, Chun Y, Gonzales M et al (2006) Nanomagnetism and spin electronics: materials, microstructure and novel properties. J Mater Sci 41:793–815. doi:10.1007/s10853-006-6564-1
76. Frei SSEH, Treves D (1957) Critical size and nucleation field of ideal ferromagnetic particles. Phys Rev 106:446–455
77. Puntes VF, Krishnan K, Alivisatos AP (2002) Synthesis of colloidal cobalt nanoparticles with controlled size and shapes. Top Catal 19:145–148
78. Bao YP, Beerman M, Pakhomov AB, Krishnan KM (2005) Controlled crystalline structure and surface stability of cobalt nanocrystals. J Phys Chem B 109:7220–7222
79. Bao Y, An W, Turner CH, Krishnan K (2009) The critical role of surfactants in the growth of cobalt nanoparticles. Langmuir 26:478–483
80. Carpenter EE (2001) Iron nanoparticles as potential magnetic carriers. J Magn Magn Mater 225:17–20
81. Guo DD, Wu CH, Li XM, Jiang H, Wang XM, Chen BA (2008) In vitro cellular uptake and cytotoxic effect of functionalized nickel nanoparticles on leukemia cancer cells. J Nanosci Nanotechnol 8:2301–2307
82. Bao Y, Pakhomov AB, Krishnan KM (2005) A general approach to synthesis of nanoparticles with controlled morphologies and magnetic properties. J Appl Phys 97:10J317 **(3 pp)**
83. Sun SH, Murray CB, Weller D, Folks L, Moser A (2000) Monodisperse FePt nanoparticles and ferromagnetic FePt nanocrystal superlattices. Science 287:1989–1992
84. Joseyphus RJ, Shinoda K, Sato Y, Tohji K, Jeyadevan B (2008) Composition controlled synthesis of fcc-FePt nanoparticles using a modified polyol process. J Mater Sci 43:2402–2406. doi:10.1007/s10853-007-1951-9
85. Wang HL, Zhang Y, Huang Y, Zeng Q, Hadjipanayis GC (2004) CoPt nanoparticles by chemical reduction. J Magn Magn Mater 272:E1279–E1280
86. Gupta AK, Gupta M (2005) Synthesis and surface engineering of iron oxide nanoparticles for biomedical applications. Biomaterials 26:3995–4021
87. Hyeon T, Lee SS, Park J, Chung Y, Na HB (2001) Synthesis of highly crystalline and monodisperse maghemite nanocrystallites without a size-selection process. J Am Chem Soc 123:12798–12801
88. Rockenberger J, Scher EC, Alivisatos AP (1999) A new nonhydrolytic single-precursor approach to surfactant-capped nanocrystals of transition metal oxides. J Am Chem Soc 121:11595–11596
89. Xie J, Peng S, Brower N, Pourmand N, Wang SX, Sun SH (2006) One-pot synthesis of monodisperse iron oxide nanoparticles for potential biomedical applications. Pure Appl Chem 78:1003–1014
90. Park J, An KJ, Hwang YS, Park JG, Noh HJ, Kim JY et al (2004) Ultra-large-scale syntheses of monodisperse nanocrystals. Nat Mater 3:891–895
91. Yu WW, Falkner JC, Yavuz CT, Colvin VL (2004) Synthesis of monodisperse iron oxide nanocrystals by thermal decomposition of iron carboxylate salts. Chem Commun 2306–2307
92. Xu YL, Qin Y, Palchoudhury S, Bao YP (2011) Water-soluble iron oxide nanoparticles with high stability and selective surface functionality. Langmuir 27:8990–8997
93. Xu YL, Baiu DC, Sherwood JA, McElreath MR, Qin Y, Lackey KH et al (2014) Linker-free conjugation and specific cell targeting of antibody functionalized iron-oxide nanoparticles. J Mater Chem B 2:6198–6206
94. Kim BH, Lee N, Kim H, An K, Park YI, Choi Y et al (2011) Large-scale synthesis of uniform and extremely small-sized iron oxide nanoparticles for high-resolution T-1 magnetic resonance imaging contrast agents. J Am Chem Soc 133:12624–12631
95. Palchoudhury S, Xu YL, An W, Turner CH, Bao YP (2010) Platinum attachments on iron oxide nanoparticle surfaces. J Appl Phys 107:09B311 **(3 pp)**
96. Young AG, Al-Salim N, Green DP, McQuillan AJ (2008) Attenuated total reflection infrared studies of oleate and trioctylphosphine oxide ligand adsorption and exchange reactions on CdS quantum dot films. Langmuir 24:3841–3849
97. Hufschmid R, Arami H, Ferguson RM, Gonzales M, Teeman E, Brush LN, Browning ND, Krishnan KM (2015) Nanoscale 7:11142–11154
98. Hai HT, Yang HT, Kura H, Hasegawa D, Ogata Y, Takahashi M et al (2010) Size control and characterization of wustite (core)/spinel (shell) nanocubes obtained by decomposition of iron oleate complex. J Colloid Interface Sci 346:37–42
99. Kovalenko MV, Bodnarchuk MI, Lechner RT, Hesser G, Schaffler F, Heiss W (2007) Fatty acid salts as stabilizers in size- and shape-controlled nanocrystal synthesis: the case of inverse spinel iron oxide. J Am Chem Soc 129:6352–6353
100. Xu ZC, Shen CM, Tian YA, Shi XZ, Gao HJ (2010) Organic phase synthesis of monodisperse iron oxide nanocrystals using iron chloride as precursor. Nanoscale 2:1027–1032
101. Kim D, Park J, An K, Yang NK, Park JG, Hyeon T (2007) Synthesis of hollow iron nanoframes. J Am Chem Soc 129:5812–5813
102. Shavel A, Rodriguez-Gonzalez B, Spasova M, Farle M, Liz-Marzan LM (2007) Synthesis and characterization of iron/iron oxide core/shell nanocubes. Adv Funct Mater 17:3870–3876
103. Kwon SG, Piao Y, Park J, Angappane S, Jo Y, Hwang NM et al (2007) Kinetics of monodisperse iron oxide nanocrystal formation by "heating-up" process. J Am Chem Soc 129:12571–12584
104. Plate NA, Mamlykh AV, Uzhinova LD, Panov VP, Rozenfel'd MA (1989) Structure of the heparin macromonomer and features of its radical polymerization. Polym Sci USSR 31:220–226
105. Kwon KW, Lee BH, Shim M (2006) Structural evolution in metal oxide/semiconductor colloidal nanocrystal heterostructures. Chem Mater 18:6357–6363
106. Park JN, Zhang P, Hu YS, McFarland E (2010) Synthesis and characterization of sintering-resistant silica-encapsulated Fe_3O_4 magnetic nanoparticles active for oxidation and chemical looping combustion. Nanotechnology 21:225708 **(8 pp)**
107. Jia CJ, Sun LD, Luo F, Han XD, Heyderman LJ, Yan ZG et al (2008) Large-scale synthesis of single-crystalline iron oxide magnetic nanorings. J Am Chem Soc 130:16968–16977
108. Issa B, Obaidat IM, Albiss BA, Haik Y (2013) Magnetic nanoparticles: surface effects and properties related to biomedicine applications. Int J Mol Sci 14:21266–21305
109. Kachkachi H, Ezzir A, Nogues M, Tronc E (2000) Surface effects in nanoparticles: application to maghemite gamma-Fe_2O_3. Eur Phys J B 14:681–689

110. Koseoglu Y, Kavas H, Aktas B (2006) Surface effects on magnetic properties of superparamagnetic magnetite nanoparticles. Phys Status Solidi 203:1595–1601
111. Millan A, Urtizberea A, Silva NJO, Palacio F, Amaral VS, Snoeck E et al (2007) Surface effects in maghemite nanoparticles. J Magn Magn Mater 312:L5–L9
112. Koseoglu Y, Kavas H (2008) Size and surface effects on magnetic properties of Fe_3O_4 nanoparticles. J Nanosci Nanotechnol 8:584–590
113. Iglesias O, Labarta A (2001) Finite-size and surface effects in maghemite nanoparticles: Monte Carlo simulations. Phys Rev B 63:184416 **(19 pp)**
114. Ding T, Song K, Clays K, Tung CH (2009) Fabrication of 3D photonic crystals of ellipsoids: convective self-assembly in magnetic field. Adv Mater 21:1936–1940
115. Yamaki M, Higo J, Nagayama K (1995) Size-dependent separation of colloidal particles in 2-dimensional convective self-assembly. Langmuir 11:2975–2978
116. Kim MH, Im SH, Park OO (2005) Rapid fabrication of two- and three-dimensional colloidal crystal films via confined convective assembly. Adv Funct Mater 15:1329–1335
117. Wen TL, Liang WK, Krishnan KM (2010) Coupling of blocking and melting in cobalt ferrofluids. J Appl Phys 107:09B501 **(3 pp)**
118. Denkov ND, Velev OD, Kralchevsky PA, Ivanov IB, Yoshimura H, Nagayama K (1992) Mechanism of formation of 2 dimensional crystals from latex-particles on substrate. Langmuir 8:3183–3190
119. Henzie J, Andrews SC, Ling XY, Li ZY, Yang PD (2013) Oriented assembly of polyhedral plasmonic nanoparticle clusters. Proc Natl Acad Sci USA 110:6640–6645
120. Zhang JH, Li YF, Zhang XM, Yang B (2010) Colloidal self-assembly meets nanofabrication: from two-dimensional colloidal crystals to nanostructure arrays. Adv Mater 22:4249–4269
121. Lalatonne Y, Richardi J, Pileni MP (2004) Van der Waals versus dipolar forces controlling mesoscopic organizations of magnetic nanocrystals. Nat Mater 3:121–125
122. Glotzer SC (2012) Nanotechnology shape matters. Nature 481:450–452
123. Jones MR, Macfarlane RJ, Prigodich AE, Patel PC, Mirkin CA (2011) Nanoparticle shape anisotropy dictates the collective behavior of surface-bound ligands. J Am Chem Soc 133:18865–18869
124. Wu LH, Jubert PO, Berman D, Imaino W, Nelson A, Zhu HY et al (2014) Monolayer assembly of ferrimagnetic $Co_xFe_{3-x}O_4$ nanocubes for magnetic recording. Nano Lett 14:3395–3399
125. Deegan RD, Bakajin O, Dupont TF, Huber G, Nagel SR, Witten TA (1997) Capillary flow as the cause of ring stains from dried liquid drops. Nature 389:827–829
126. Yunker PJ, Still T, Lohr MA, Yodh AG (2011) Suppression of the coffee-ring effect by shape-dependent capillary interactions. Nature 476:308–311
127. Damasceno PF, Engel M, Glotzer SC (2012) Predictive self-assembly of polyhedra into complex structures. Science 337:453–457
128. Mueggenburg KE, Lin XM, Goldsmith RH, Jaeger HM (2007) Elastic membranes of close-packed nanoparticle arrays. Nat Mater 6:656–660
129. He JB, Kanjanaboos P, Frazer NL, Weis A, Lin XM, Jaeger HM (2010) Fabrication and mechanical properties of large-scale freestanding nanoparticle membranes. Small 6:1449–1456
130. Kanjanaboos P, Joshi-Imre A, Lin XM, Jaeger HM (2011) Strain patterning and direct measurement of Poisson's ratio in nanoparticle mono layer sheets. Nano Lett 11:2567–2571
131. Murray CB, Kagan CR, Bawendi MG (2000) Synthesis and characterization of monodisperse nanocrystals and close-packed nanocrystal assemblies. Ann Rev Mater Sci 30:545–610
132. Singh A, Dickinson C, Ryan KM (2012) Insight into the 3D architecture and quasicrystal symmetry of multilayer nanorod assemblies from moire interference patterns. ACS Nano 6:3339–3345
133. Puntes VF, Gorostiza P, Aruguete DM, Bastus NG, Alivisatos AP (2004) Collective behaviour in two-dimensional cobalt nanoparticle assemblies observed by magnetic force microscopy. Nat Mater 3:263–268
134. Yamamoto K, Hogg CR, Yamamuro S, Hirayama T, Majetich SA (2011) Dipolar ferromagnetic phase transition in Fe_3O_4 nanoparticle arrays observed by Lorentz microscopy and electron holography. Appl Phys Lett 98:072509 **(3 pp)**
135. Wen TL, Booth RA, Majetich SA (2012) Ten-nanometer dense hole arrays generated by nanoparticle lithography. Nano Lett 12:5873–5878
136. Claridge SA, Castleman AW, Khanna SN, Murray CB, Sen A, Weiss PS (2009) Cluster-assembled materials. ACS Nano 3:244–255
137. Lopes WA, Jaeger HM (2001) Hierarchical self-assembly of metal nanostructures on diblock copolymer scaffolds. Nature 414:735–738
138. Alba M, Pazos-Perez N, Vaz B, Formentin P, Tebbe M, Correa-Duarte MA et al (2013) Macroscale plasmonic substrates for highly sensitive surface-enhanced raman scattering. Angew Chem Int Ed 52:6459–6463
139. Wen TL, Krishnan KM (2011) Cobalt-based magnetic nanocomposites: fabrication, fundamentals and applications. J Phys D 44:393001 **(24 pp)**
140. Wen TL, Krishnan KM (2011) Magnetic properties of Au-core-Co-shell nanoparticles. J Appl Phys 109:07B515 **(3 pp)**
141. Wen TL, Krishnan KM (2010) Thermal stability and morphological transformations of Au-core-Co-shell nanocrucibles. J Phys Chem C 114:14838–14842
142. Wen TL, Liu D, Luscombe CK, Krishnan KM (2009) Granular magnetoresistance in cobalt/poly (3-hexylthiophene, 2, 5-diyl) hybrid thin films prepared by a wet chemical method. Appl Phys Lett 95:082509 **(3 pp)**
143. Situ SF, Samia ACS (2014) Highly efficient antibacterial iron oxide@carbon nanochains from wustite precursor nanoparticles. ACS Appl Mater Interface 6:20154–20163
144. Lu F, Popa A, Zhou SW, Zhu JJ, Samia ACS (2013) Iron oxide-loaded hollow mesoporous silica nanocapsules for controlled drug release and hyperthermia. Chem Commun 49:11436–11438
145. Filipcsei G, Csetneki I, Szilagyi A, Zrinyi M (2007) Magnetic field-responsive smart polymer composites. In: Abe A, Albertsson A-C, Coates GW, Genzer J, Kobayashi S, Lee K-S, Leibler L, Long TE, Möller M, Okay O, Percec V, Tang BZ, Terentjev EM, Vicent MJ, Voit B, Wiesner U, Zhang X (eds) Advances in polymer science, vol 206. Springer, Berlin, pp 137–189
146. Kumar UN, Kratz K, Wagermaier W, Behl M, Lendlein A (2010) Non-contact actuation of triple-shape effect in multi-phase polymer network nanocomposites in alternating magnetic field. J Mater Chem 20:3404–3415
147. Stepanov GV, Borin DY, Raikher YL, Melenev PV, Perov NS (2008) Motion of ferroparticles inside the polymeric matrix in magnetoactive elastomers. J Phys 20:204121 **(6 pp)**
148. Thévenot J, Oliveira H, Sandre O, Lecommandoux S (2013) Magnetic responsive polymer composite materials. Chem Soc Rev 42:7099–7116
149. Ding XB, Sun ZH, Wan GX, Jiang YY (1998) Preparation of thermosensitive magnetic particles by dispersion polymerization. React Funct Polym 38:11–15
150. Zrínyi M, Barsi L, Büki A (1996) Deformation of ferrogels induced by nonuniform magnetic fields. J Chem Phys 104:8750–8756

151. Visakh PM, Thomas S, Chandra AK, Mathew AP (2013) Advances in elastomers II: composites and nanocomposites. Springer, Berlin
152. Kost J, Langer R (2012) Responsive polymeric delivery systems. Adv Drug Deliv Rev 64:327–341
153. Luo L-B, Yu S-H, Qian H-S, Gong J-Y (2006) Large scale synthesis of uniform silver@carbon rich composite (carbon and cross-linked PVA) sub-microcables by a facile green chemistry carbonization approach. Chem Commun 793–795
154. Jones CD, Lyon LA (2000) Synthesis and characterization of multiresponsive core–shell microgels. Macromolecules 33: 8301–8306
155. Zhou S, Chu B (1998) Synthesis and volume phase transition of poly(methacrylic acid- co-N-isopropylacrylamide) microgel particles in water. J Phys Chem B 102:1364–1371
156. Galeotti F, Bertini F, Scavia G, Bolognesi A (2011) A controlled approach to iron oxide nanoparticles functionalization for magnetic polymer brushes. J Colloid Interface Sci 360:540–547
157. Li X, Liu Y, Xu Z, Yan H (2011) Preparation of magnetic microspheres with thiol-containing polymer brushes and immobilization of gold nanoparticles in the brush layer. Eur Polym J 47:1877–1884
158. Liu B, Zhang D, Wang J, Chen C, Yang X, Li C (2013) Multilayer magnetic composite particles with functional polymer brushes as stabilizers for gold nanocolloids and their recyclable catalysis. J Phys Chem C 117:6363–6372
159. Xu F, Geiger JH, Baker GL, Bruening ML (2011) Polymer brush-modified magnetic nanoparticles for His-tagged protein purification. Langmuir 27:3106–3112
160. Ranjan R, Brittain WJ (2007) Combination of living radical [polymerization and click chemistry for surface modification. Macromolecules 40:6217–6223
161. Schmidt AM (2005) The synthesis of magnetic core-shell nanoparticles by surface-initiated ring-opening polymerization of e-caprolactone. Macromol Rapid Commun 26:93–97
162. Moraes J, Ohno K, Maschmeyer T, Perrier S (2013) Synthesis of silica-polymer core-shell nanoparticles by reversible addition-fragmentation chain transfer polymerization. Chem Commun 49:9077–9088
163. Vestal CR, Zhang ZJ (2002) Atom transfer radical polymerization synthesis and magnetic characterization of $MnFe_2O_4$/polystyrene core/shell nanoparticles. J Am Chem Soc 124:14312–14313
164. Wang Y, Teng X, Wang J-S, Yang H (2003) Solvent-free atom transfer radical polymerization in the synthesis of Fe_2O_3 @polystyrene core–shell nanoparticles. Nano Lett 3:789–793
165. Achilleos DS, Vamvakaki M (2010) End-grafted polymer chains onto inorganic nano-objects. Materials 3:1981–2026
166. Nasongkla N, Bey E, Ren J, Ai H, Khemtong C, Guthi JS et al (2006) Multifunctional polymeric micelles as cancer-targeted, MRI-ultrasensitive drug delivery systems. Nano Lett 6:2427–2430
167. Kloust H, Pöselt E, Kappen S, Schmidtke C, Kornowski A, Pauer W et al (2012) Ultrasmall biocompatible nanocomposites: a new approach using seeded emulsion polymerization for the encapsulation of nanocrystals. Langmuir 28:7276–7281
168. Chern CS (2006) Emulsion polymerization mechanisms and kinetics. Prog Polym Sci 31:443–486
169. Keng PY, Bull MM, Shim I-B, Nebesny KG, Armstrong NR, Sung Y et al (2011) Colloidal polymerization of polymer-coated ferromagnetic cobalt nanoparticles into Pt-Co_3O_4 nanowires. Chem Mater 23:1120–1129
170. Cuppoletti J (2011) Metal, ceramic and polymeric composites for various uses. InTech, chap 25
171. Tanahashi M (2010) Development of fabrication methods of filler/polymer nanocomposites: with focus on simple melt-compounding-based approach without surface modification of nanofillers. Materials 3:1593–1619
172. Yang T-I, Brown RNC, Kempel LC, Kofinas P (2008) Magneto-dielectric properties of polymer—Fe_3O_4 nanocomposites. J Magn Magn Mater 320:2714–2720
173. Wang D, Wang K, Xu W (2013) Novel fabrication of magnetic thermoplastic nanofibers via melt extrusion of immiscible blends. Polym Adv Technol 24:70–74
174. Bin Y, Yamanaka A, Chen QY, Xi Y, Jiang XW, Matsuo M (2007) Morphological, electrical and mechanical properties of ultrahigh molecular weight polyethylene and multi-wall carbon nanotube composites prepared in decalin and paraffin. Polym J 39:598–609
175. Rong MZ, Zhang MQ, Zheng YX, Zeng HM, Friedrich K (2001) Improvement of tensile properties of nano-SiO_2/PP composites in relation to percolation mechanism. Polymer 42:3301–3304
176. Pan G, Guo Q, Tian A, He Z (2008) Mechanical behaviors of Al_2O_3 nanoparticles reinforced polyetheretherketone. Mater Sci Eng A 492:383–391
177. Pablico-Lansigan MH, Situ SF, Samia ACS (2013) Magnetic particle imaging: advancements and perspectives for real-time in vivo monitoring and image-guided therapy. Nanoscale 5:4040–4055
178. Hermanson GT (2008) Bioconjugate techniques, 2nd edn. Academic Press, San Diego
179. Lee H, Rho J, Messersmith PB (2009) Facile conjugation of biomolecules onto surfaces via mussel adhesive protein inspired coatings. Adv Mater 21:431–432
180. Lee H, Dellatore SM, Miller WM, Messersmith PB (2007) Mussel-inspired surface chemistry for multifunctional coatings. Science 318:426–430
181. Stuart BH (2004) Infrared spectroscopy [electronic resource]: fundamentals and applications. Wiley, Hoboken
182. Wang XY, Jin BK, Lin XQ (2002) In-situ FTIR spectroelectrochemical study of dopamine at a glassy carbon electrode in a neutral solution. Anal Sci 18:931–933
183. Modak S, Cheung NK (2007) Disialoganglioside directed immunotherapy of neuroblastoma. Cancer Investig 25:67–77
184. Yoshida S, Fukumoto S, Kawaguchi H, Sato S, Ueda R, Furukawa K (2001) Ganglioside G(D2) in small cell lung cancer cell lines: enhancement of cell proliferation and mediation of apoptosis. Cancer Res 61:4244–4252
185. Jiao P, Zhou H, Otto M, Mu Q, Li L, Su G et al (2011) Leading neuroblastoma cells to die by multiple premeditated attacks from a multifunctionalized nanoconstruct. J Am Chem Soc 133:13918–13921
186. Ross CA, Smith HI, Savas T, Schattenburg M, Farhoud M, Hwang M et al (1999) Fabrication of patterned media for high density magnetic storage. J Vac Sci Technol B 17:3168–3176
187. Albrecht TR, Bedau D, Dobisz E, Gao H, Grobis M, Hellwig O et al (2013) Bit patterned media at 1 Tdot/in(2) and beyond. IEEE Trans Magn 49:773–778
188. Kikitsu A, Maeda T, Hieda H, Yamamoto R, Kihara N, Kamata Y (2013) 5 Tdots/in(2) bit patterned media fabricated by a directed self-assembly mask. IEEE Trans Magn 49:693–698
189. Terris BD, Thomson T (2005) Nanofabricated and self-assembled magnetic structures as data storage media. J Phys D 38:R199–R222
190. Broers AN, Hoole ACF, Ryan JM (1996) Electron beam lithography—resolution limits. Microelectron Eng 32:131–142
191. Vieu C, Carcenac F, Pepin A, Chen Y, Mejias M, Lebib A et al (2000) Electron beam lithography: resolution limits and applications. Appl Surf Sci 164:111–117
192. Tseng AA, Chen K, Chen CD, Ma KJ (2003) Electron beam lithography in nanoscale fabrication: recent development. IEEE Trans Electron Packag Manuf 26:141–149

193. Park M, Harrison C, Chaikin PM, Register RA, Adamson DH (1997) Block copolymer lithography: periodic arrays of similar to 10(11) holes in 1 square centimeter. Science 276:1401–1404
194. Ruiz R, Kang HM, Detcheverry FA, Dobisz E, Kercher DS, Albrecht TR et al (2008) Density multiplication and improved lithography by directed block copolymer assembly. Science 321:936–939
195. Fasolka MJ, Mayes AM (2001) Block copolymer thin films: physics and applications. Ann Rev Mater Res 31:323–355
196. Stoykovich MP, Nealey PF (2006) Block copolymers and conventional lithography. Mater Today 9:20–29
197. Hogg CR, Majetich SA, Bain JA (2010) Investigating pattern transfer in the small-gap regime using electron-beam stabilized nanoparticle array etch masks. IEEE Trans Magn 46:2307–2310
198. Keil D, Anderson E (2001) Characterization of reactive ion etch lag scaling. J Vac Sci Technol B 19:2082–2088
199. Seshadri K, Froyd K, Parikh AN, Allara DL, Lercel MJ, Craighead HG (1996) Electron-beam-induced damage in self-assembled monolayers. J Phys Chem 100:15900–15909
200. Lercel MJ, Rooks M, Tiberio RC, Craighead HG, Sheen CW, Parikh AN et al (1995) Pattern transfer of electron-beam modified self-assembled monolayers for high-resolution lithography. J Vac Sci Technol B 13:1139–1143
201. Balachova OV, Alves MAR, Swart JW, Braga ES, Cescato L (2000) CF4 plasma etching of materials used in microelectronics manufacturing. Microelectron J 31:213–215
202. Cao G, Wang Y (2011) Nanostructures & nanomaterials : synthesis, properties, and applications, 2nd edn. World Scientific, New Jersey
203. Su KH, Wei QH, Zhang X, Mock JJ, Smith DR, Schultz S (2003) Interparticle coupling effects on plasmon resonances of nanogold particles. Nano Lett 3:1087–1090
204. Gleich B, Weizenecker J (2005) Tomographic imaging using the nonlinear response of magnetic particles. Nature 435:1214–1217
205. Weizenecker J, Gleich B, Rahmer J, Dahnke H, Borgert J (2009) Three-dimensional real-time in vivo magnetic particle imaging. Phys Med Biol 54:L1–L10
206. Sattel TF, Knopp T, Biederer S, Gleich B, Weizenecker J, Borgert J et al (2009) Single-sided device for magnetic particle imaging. J Phys D 42:022001–022005
207. Weizenecker J, Borgert J, Gleich B (2007) A simulation study on the resolution and sensitivity of magnetic particle imaging. Phys Med Biol 52:6363–6374
208. Goodwill PW, Scott GC, Stang PP, Conolly SM (2009) Narrowband magnetic particle imaging. IEEE Trans Med Imaging 28:231–1237
209. Goodwill PW, Conolly SM (2010) The X-space formulation of the magnetic particle imaging process: 1-D signal, resolution, bandwidth, SNR, SAR, and magnetostimulation. IEEE Trans Med Imaging 29:851–1859
210. Ferguson RM, Minard KR, Khandhar AP, Krishnan KM (2011) Optimizing magnetite nanoparticles for mass sensitivity in magnetic particle imaging. Med Phys 38:1619–1626
211. Ferguson RM, Minard KR, Krishnan KM (2009) Optimization of nanoparticle core size for magnetic particle imaging. J Magn Magn Mater 321:1548–1551
212. Ferguson RM, Khandhar AP, Krishnan KM (2012) Tracer design for magnetic particle imaging. J Appl Phys 111:07B3181–07B3185
213. Goodwill PW, Conolly SM (2011) Experimental demonstration of X-space magnetic particle imaging. Proc SPIE7 965:79650U1–79650U6
214. Lüdtke-Buzug K, Rapoport DH, Schneider D. Presented at the 8th international conference on the scientific and clincal applications of magnetic carriers, Rostock, Germany, 2010
215. Knopp T, Buzug TM (2012) Magnetic particle imaging: an introduction to imaging principles and scanner instrumentation. Spinger, Berlin
216. Bulte JW, Gleich B, Weizenecker J, Bernard S, Walczak P, Markov DE et al (2008) Developing cellular MPI: initial experience. Proc Intl Soc Mag Reson Med 16:201–204
217. Markov DE, Boeve H, Gleich B, Borgert J, Antonelli A, Sfara C et al (2010) Human erythrocytes as nanoparticle carriers for magnetic particle imaging. Phys Med Biol 55:6461–6473
218. Gilchris RK, Medal R, Shorey WD, Hanselman RC, Parrott JC, Taylor CB (1957) Selective inductive heating of lymph nodes. Ann Surg 146:596–606
219. Meyers PH, Cronic F, NIice CM (1963) Experimental approach in the use and magnetic control of metallic iron particles in the lymphatic and vascular system of dogs as a contrast and isotopic agent. Am J Roentgenol Radium Therapy Nucl Med 90:1068–1077
220. Häfeli UO (2004) Magnetically modulated therapeutic systems. Int J Pharm 277:19–24
221. Barakat NS (2009) Magnetically modulated nanosystems: a unique drug-delivery platform. Nanomedicine 4:799–812
222. McBain SC, Yiu HHP, Dobson J (2008) Magnetic nanoparticles for gene and drug delivery. Int J Nanomed 3:169–180
223. Lee J-H, Kim J-W, Cheon J (2013) Magnetic nanoparticles for multi-imaging and drug delivery. Mol Cells 35:274–284
224. Slowing II, Vivero-Escoto JL, Wu C-W, Lin VS-Y (2008) Mesoporous silica nanoparticles as controlled release drug delivery and gene transfection carriers. Adv Drug Deliv Rev 60:1278–1288
225. Wang LY, Luo J, Fan Q, Suzuki M, Suzuki IS, Engelhard MH et al (2005) Monodispersed core-shell Fe_3O_4@Au nanoparticles. J Phys Chem B 109:21593–21601
226. Grumezescu AM (2015) Biocompatible magnetic hollow silica microspheres for drug delivery. Curr Org Chem 17:1029–1033
227. Márquez F, Herrera GM, Campo T, Cotto M, Ducongé J, Sanz JM et al (2012) Preparation of hollow magnetite microspheres and their applications as drugs carriers. Nanoscale Res Lett 7:210 **(11 pp)**
228. Fuchigami T, Kawamura R, Kitamoto Y, Nakagawa M, Namiki Y (2012) A magnetically guided anti-cancer drug delivery system using porous FePt capsules. Biomaterials 33:1682–1687
229. Chen ML, He YJ, Chen XW, Wang JH (2012) Quantum dots conjugated with Fe_3O_4-filled carbon nanotubes for cancer-targeted imaging and magnetically guided drug delivery. Langmuir 28:16469–16476
230. Masotti A, Caporali A (2013) Preparation of magnetic carbon nanotubes (Mag-CNTs) for biomedical and biotechnological applications. Int J Mol Sci 14:24619–24642
231. Mashhadizadeh MH, Amoli-Diva M (2012) Drug-carrying amino silane coated magnetic nanoparticles as potential vehicles for delivery of antibiotics. J Nanomed Nanotechnol 3:1000139 **(7 pp)**
232. Häfeli UO, Sweeney SM, Beresford BA, Humm JL, Macklis RM (1995) Effective targeting of magnetic radioactive 90Y-microspheres to tumor cells by an externally applied magnetic field. Preliminary in vitro and in vivo results. Nucl Med Biol 22:147–155
233. Edelman ER, Langer R (1993) Optimization of release from magnetically controlled polymeric drug release devices. Biomaterials 14:621–626
234. Chen H, Langer R (1997) Magnetically-responsive polymerized liposomes as potential oral delivery vehicles. Pharm Res 14:537–540
235. Jain TK, Richey J, Strand M, Leslie-Pelecky DL, Flask CA, Labhasetwar V (2008) Magnetic nanoparticles with dual

functional properties: drug delivery and magnetic resonance imaging. Biomaterials 29:4012–4021
236. Lim EK, Huh YM, Yang J, Lee K, Suh JS, Haam S (2011) pH-triggered drug-releasing magnetic nanoparticles for cancer therapy guided by molecular imaging by MRI. Adv Mater 23:2436–2442
237. Terreno E, Castelli DD, Viale A, Aime S (2010) Challenges for molecular magnetic resonance imaging. Chem Rev 110:3019–3042
238. Waters EA, Wickline SA (2008) Contrast agents for MRI. Basic Res Cardiol 103:114–121
239. Strijkers GJ, Mulder WJM, van Tilborg GAF, Nicolay K (2007) MRI contrast agents: current status and future perspectives. Anticancer Agents Med Chem 7:291–305
240. Advanced Magnetics (1996) FDA approval for Feridex iv liver contrast agent. Drug News Persp 9:422–422
241. Hamm B, Staks T, Tapuitz M, Maibauer R, Speidel A, Huppertz A et al (1994) Contrast-enhanced MR-imaging of liver and spleen—1st experience in humans with a new superparamagnetic iron oxide. J Magn Res Imaging 4:659–668
242. Baiu DC, Brazel C, Bao Y, Otto M (2013) Interactions of iron oxide nanoparticles with the immune system: challenges and opportunities for their use in nano-oncology. Curr Pharm Des 19:6606–6621
243. Brisset JC, Sigovan M, Chauveau F, Riou A, Devillard E, Desestret V et al (2011) Quantification of iron-labeled cells with positive contrast in mouse brains. Mol Imaging Biol 13:672–678
244. Okuhata Y (1999) Delivery of diagnostic agents for magnetic resonance imaging. Adv Drug Deliv Rev 37:121–137
245. Hasebroock KM, Serkova NJ (2009) Toxicity of MRI and CT contrast agents. Exp Opin Drug Metabol Toxicol 5:403–416
246. Lin CH, Cai SH, Feng JH (2012) Positive contrast imaging of SPIO nanoparticles. J Nanomater 2012:734842 **(7 pp)**
247. Eibofner F, Steidle G, Kehlbach R, Bantleon R, Schick F (2010) Positive contrast imaging of iron oxide nanoparticles with susceptibility-weighted imaging. Magn Reson Med 64:1027–1038
248. Zhu HT, Demachi K, Sekino M (2011) Phase gradient imaging for positive contrast generation to superparamagnetic iron oxide nanoparticle-labeled targets in magnetic resonance imaging. Magn Reson Med 29:891–898
249. Tromsdorf UI, Bruns OT, Salmen SC, Beisiegel U, Weller H (2009) A highly effective, nontoxic T-1 MR contrast agent based on ultrasmall PEGylated iron oxide nanoparticles. Nano Lett 9:4434–4440
250. Park JY, Choi ES, Baek MJ, Lee GH, Woo S, Chang Y (2009) Water-soluble ultra small paramagnetic or superparamagnetic metal oxide nanoparticles for molecular MR imaging. Eur J Inorg Chem 2009:2477–2481
251. Taboada E, Rodriguez E, Roig A, Oro J, Roch A, Muller RN (2007) Relaxometric and magnetic characterization of ultrasmall iron oxide nanoparticles with high magnetization. Evaluation as potential T-1 magnetic resonance imaging contrast agents for molecular imaging. Langmuir 23:4583–4588
252. Li Z, Yi PW, Sun Q, Lei H, Zhao HL, Zhu ZH et al (2012) Ultrasmall water-soluble and biocompatible magnetic iron oxide nanoparticles as positive and negative dual contrast agents. Adv Funct Mater 22:2387–2393
253. Longmire M, Choyke PL, Kobayashi H (2008) Clearance properties of nano-sized particles and molecules as imaging agents: considerations and caveats. Nanomedicine 3:703–717
254. Prakash A, Zhu HG, Jones CJ, Benoit DN, Ellsworth AZ, Bryant EL et al (2009) Bilayers as phase transfer agents for nanocrystals prepared in nonpolar solvents. ACS Nano 3:2139–2146
255. Lu M, Cohen MH, Rieves D, Pazdur R (2010) FDA report: ferumoxytol for intravenous iron therapy in adult patients with chronic kidney disease. Am J Hematol 85:315–319
256. Goodwill PW, Saritas EU, Croft LR, Kim TN, Krishnan KM, Schaffer DV et al (2012) X-space MPI: magnetic nanoparticles for safe medical imaging. Adv Mater 24:3870–3877
257. Khandhar AP, Ferguson RM, Arami H, Krishnan KM (2013) Monodisperse magnetite nanoparticle tracers for in vivo magnetic particle imaging. Biomaterials 34:3837–3845
258. Douek M, Klaase J, Monypenny I, Kothari A, Zechmeister K, Brown D et al (2014) Sentinel node biopsy using a magnetic tracer versus standard technique: the SentiMAG multicentre trial. Ann Surg Oncol 21:1237–1245
259. Wong SL, Balch CM, Hurley P, Agarwala SS, Akhurst TJ, Cochran A et al (2012) Sentinel lymph node biopsy for melanoma: American Society of Clinical Oncology and Society of Surgical Oncology joint clinical practice guideline. J Clin Oncol 30:2912–2918
260. Hawkins BT, Davis TP (2005) The blood-brain barrier/neurovascular unit in health and disease. Pharmacol Rev 57:173–185
261. Wiley DT, Webster P, Gale A, Davis ME (2013) Transcytosis and brain uptake of transferrin-containing nanoparticles by tuning avidity to transferrin receptor. Proc Natl Acad Sci USA 110:8662–8667
262. Maack T, Johnson V, Kau ST, Figueiredo J, Sigulem D (1979) Renal filtration, transport, and metabolism of low-molecular-weight proteins: a review. Kidney Int 16:251–270
263. Choi HS, Liu W, Misra P, Tanaka E, Zimmer JP, Ipe BI et al (2007) Renal clearance of quantum dots. Nat Biotechnol 25:1165–1170
264. Sarin H (2010) Physiologic upper limits of pore size of different blood capillary types and another perspective on the dual pore theory of microvascular permeability. J Angiogenes Res 2:14 **(19 pp)**
265. Hume DA (2006) The mononuclear phagocyte system. Curr Opin Immunol 18:49–53
266. Braet F, Wisse E (2002) Structural and functional aspects of liver sinusoidal endothelial cell fenestrae: a review. Comp Hepatol 1:1 **(17 pp)**
267. Wisse E, Jacobs F, Topal B, Frederik P, De Geest B (2008) The size of endothelial fenestrae in human liver sinusoids: implications for hepatocyte-directed gene transfer. Gene Ther 15:1193–1199
268. Cesta MF (2006) Normal structure, function, and histology of the spleen. Toxicol Pathol 34:455–465
269. Prabhakar U, Maeda H, Jain RK, Sevick-Muraca EM, Zamboni W, Farokhzad OC et al (2013) Challenges and key considerations of the enhanced permeability and retention effect for nanomedicine drug delivery in oncology. Cancer Res 73:2412–2417
270. Ahmed M, Purushotham AD, Douek M (2014) Novel techniques for sentinel lymph node biopsy in breast cancer: a systematic review. Lancet Oncol 15:e351–e362
271. Klimberg VS, Rubio IT, Henry R, Cowan C, Colvert M, Korourian S (1999) Subareolar versus peritumoral injection for location of the sentinel lymph node. Ann Surg 229:860–865
272. Thill M, Kurylcio A, Welter R, van Haasteren V, Grosse B, Berclaz G et al (2014) The Central-European SentiMag study: sentinel lymph node biopsy with superparamagnetic iron oxide (SPIO) vs. radioisotope. Breast 23:175–179
273. Bourrinet P, Bengele HH, Bonnemain B, Dencausse A, Idee JM, Jacobs PM et al (2006) Preclinical safety and pharmacokinetic profile of ferumoxtran-10, an ultrasmall superparamagnetic iron oxide magnetic resonance contrast agent. Invest Radiol 41:313–324
274. Fang C, Shi B, Pei YY, Hong MH, Wu J, Chen HZ (2006) In vivo tumor targeting of tumor necrosis factor-alpha-loaded stealth nanoparticles: effect of MePEG molecular weight and particle size. Eur J Pharm Sci 27:27–36

275. Metz S, Bonaterra G, Rudelius M, Settles M, Rummeny EJ, Daldrup-Link HE (2004) Capacity of human monocytes to phagocytose approved iron oxide MR contrast agents in vitro. Eur Radiol 14:1851–1858
276. Matuszewski L, Persigehl T, Wall A, Schwindt W, Tombach B, Fobker M et al (2005) Cell tagging with clinically approved iron oxides: feasibility and effect of lipofection, particle size, and surface coating on labeling efficiency. Radiology 235:155–161
277. Alexis F, Pridgen E, Molnar LK, Farokhzad OC (2008) Factors affecting the clearance and biodistribution of polymeric nanoparticles. Mol Pharm 5:505–515
278. Owens DE 3rd, Peppas NA (2006) Opsonization, biodistribution, and pharmacokinetics of polymeric nanoparticles. Int J Pharm 307:93–102
279. Storm G, Belliot SO, Daemen T, Lasic DD (1995) Surface modification of nanoparticles to oppose uptake by the mononuclear phagocyte system. Adv Drug Deliv Rev 17:31–48
280. Aggarwal P, Hall JB, McLeland CB, Dobrovolskaia MA, McNeil SE (2009) Nanoparticle interaction with plasma proteins as it relates to particle biodistribution, biocompatibility and therapeutic efficacy. Adv Drug Deliv Rev 61:428–437
281. Almeida JP, Chen AL, Foster A, Drezek R (2011) In vivo biodistribution of nanoparticles. Nanomedicine 6:815–835
282. Schlenoff JB (2014) Zwitteration: coating surfaces with zwitterionic functionality to reduce nonspecific adsorption. Langmuir 30:9625–9636
283. Shuai XT, Merdan T, Unger F, Wittmar M, Kissel T (2003) Novel biodegradable ternary copolymers hy-PEI-g-PCL-b-PEG: synthesis, characterization, and potential as efficient nonviral gene delivery vectors. Macromolecules 36:5751–5759
284. Jokerst JV, Lobovkina T, Zare RN, Gambhir SS (2011) Nanoparticle PEGylation for imaging and therapy. Nanomedicine 6:715–728
285. Gong P, Grainger DW (2007) Nonfouling surfaces: a review of principles and applications for microarray capture design assays. Method Mol Biol 381:59–92
286. Beard JL, Dawson H, Pinero DJ (1996) Iron metabolism: a comprehensive review. Nutr Rev 54:295–317
287. Ganz T (2013) Systemic iron homeostasis. Physiol Rev 93:1721–1741
288. Andrews NC (1999) Disorders of iron metabolism. N Engl J Med 341:1986–1995
289. Galvez N, Fernandez B, Sanchez P, Cuesta R, Ceolin M, Clemente-Leon M et al (2008) Comparative structural and chemical studies of ferritin cores with gradual removal of their iron contents. J Am Chem Soc 130:8062–8068